Final response

We want to thank the referees for their valuable comments and remarks.

The purpose of this paper is to present a new compact instrument for simultaneous observations of mesospheric CO and O3. Our focus is to present the instrument, the measurement technique, the inversion procedure and the first results compared with one satellite sensor.
We have chosen the journal of Geoscientific Instrumentation, Methods and Data Systems since we believe that this an appropriate choice for a presentation of a new instrument and its first data.

This document has three sections:

The answers to Referee 1

CO as a tracer has been used by others, e.g. Funke et.al (2009). Please refer to some of the recent scientific history when attempting to interpret CO profiles and to justify why measurements of mesospheric CO is interesting. I recommend the PhD thesis of Dr. Hoffmann (2012) for a detailed account of the interpretion of measurements of CO by ground-based millimeterwave radiometry.
We agree that Hoffmann (2012) gives a good description of both the dynamics of the polar mesosphere and the seasonal variation of mesospheric CO. His work is now mentioned in the Introduction.

Generally the connection to existing work is very cursory and not sufficient. For both gases CO and O3 exist a number of instruments measuring O3 or CO, so neither measurements are new. The advantages and disadvantages of the presented instrument are only little discussed and not related to other measurement principles. Since our aim is to present the first results of a new instrument we focused on the different existing instruments rather than on the different users. We agree that the references has been to sparse and we have done several additions (see comments below)

The manuscript should be published after a major revision.

Introduction
The discussion of existing work related to millimeterwave measurements of Ozone and CO is by far not complete. A few examples, not an exhaustive literature research:

Palm et al (2010) describe an Ozone instrument (OZORAM) with emphasis to the mesosphere. They used EOS-MLS on the AURA satellite and the SABER instrument on the TIMED satellite to compare the OZORAM results to satellite measurements and found, that MLS-measurements (version 2.2) is not comparing well to OZORAM at 70 km altitude and above, whereas SABER measures similar values. From Palm et.al (2010) I would conclude that the MLS measurements in version 2.2 were not able to measure O3 as high as 70 km. Has this changed in the new version?
Palm et.al (2010) is now mentioned in the Introduction under load-switching and in section 6 Satellite comparisons. The upper limit of the MLS O3 data has not changed between v2.2 and v3.3 and is still 2 Pa (about 75 km). We thank the referee for this comment and we have changed the upper limit of the OSO-MLS comparison in the text and in figure 16 to 2.4 Pa

Boyd (2007) also discusses an ozone instrument measuring at 110 GHz and also discusses comparison to MLS. Boyd et.al (2010) is now mentioned in the Introduction under sky-switching, and in section 6 Satellite comparisons

Hocke (2007) provides yet another comparison of a millimeterwave measurements of Ozone at 142 GHz and also compares to a profiles obtained from several satellite instruments, including MLS. Hocke et al. (2007) is now mentioned in the Introduction under load-switching.

Connor (1994) and Connor (1995) discussed millimeterwave radiometry at 110 GHz and the error analysis in great detail. Especially the latter publication of Connor sets a baseline for error discussion of retrievals of O3 from millimeterwave instruments and should not be left out. The findings sould also be discussed refering to this publication. Connor (1995) was one of the first to carefully implement Clive Rodgers formalism on the Optimal Estimation Method. However, nowadays using Rodgers formalism in microwave retrievals is considered standard method especially after the publication of Rodgers (2000). We therefore do not see the need to cite an error analysis of an instrument not used in our paper. We do agree that Connor (1994) is relevant for our paper, and it is now mentioned in the Introduction under sky-switching.

Studer et.al. (2013) has not been published in AMT but only in discussions and a final publication is not foreseen. For the described instrument, GROMOS, there are other publications which might be more appropriate. A more appropriate and recent paper is now chosen, (Moreria et al., 2015)

A similar lack in history can be stated for CO measurements by ground based millimeterwave radiometry. Recent experiments include Biagio (2010) and de Zafra (2004). Kuenzi and Carlson (1982) used the same frequency to measure atmospheric CO. These papers are now mentioned in the Introduction under CO measurements

Please complete the discussion of measurements of O3 and CO by means of groundbased millimeterwave radiometry and put your instrument into context of the existing scientific literature. This is also valid for the discussion of the results and the conclusion. In section 6, Satellite comparison, our comparisons with MLS are now compared to other similar investigations.

Page 319

I dont quite understood why the authors choose frequency switching as the Dicke switch method opposed to the total power calibration used for other instruments. The method restricts the bandwith, hence is the reason that the instrument cannot measure O3 in the lower and middle stratosphere, I would doubt that the method is appropriate for the measurement of O3. Because a large part of O3 is below the lower boundary of the measurement I would be concerned about varying attenuation due to O3. Yet the authors did not mention how they deal with it.
The attenuation of O3 up to about 20 km is taken care of by the tropospheric correction, this is now mentioned in the text. The attenuation of the mesospheric O3 signal due to stratospheric O3 is about 5%. The mean attenuation is taken into account by the apriori O3 profile. The effect of any error in the apriori stratospheric ozone profile is included in the error analysis as the term +-50% XA in figure 10.

It seems that the instrument could measure in Total Power mode (load-switching) also. Is this true? Please discuss the advantages of the frequency method with reference to the load-switching mode, in particular because the frequency-switching method places severe restrictions to O3 measurements. Yes the radiometer can be used in many different configurations. We have focused on the mesosphere region and we therefore use frequency switching. In the Introduction and the Summary we clearly state that this instrument, in the current configuration, is limited to mesopheric observations of O3 due to the small frequency throw in the frequency switching. Frequency switching has been a conscious choice since we want to study the mesosphere. The effective observation time is twice as high with frequency switching compared to load or sky switching since no time is spent observing a reference. This is now clarified in the Introduction.

CO is only abundant in the polar region. In the presence of sun light, it is removed quickly from the mesosphere. Hence the possibility to measure CO and O3 simultaneously is not interesting in mid latitudes or tropical regions. We agree that this dual function may not be as interesting for a low latitude site. In the Introduction we have now added that measurements of mesopsheric CO is especially interesting at high latitudes.

The integration time for one measurement is quite long for O3 in the mesosphere, given that the transisition between night and day is more or less instantaneous. The measurement would last over the terminator, so mixing two very different states in the mesosphere occurs. We do not claim that the chosen time periods are optimal and furthermore in future studies other periods can be chosen since the integration time of each individual spectrum is only 5 min. The fact that no time is spent observing a reference load makes frequency switching ideal for observing fast changes in the mesosphere.

Page 321
line 16 For the radiometers ASTRID and KONRAD, is there any publication describing those instruments? Elgered and Jarlemark (1998) is the best paper describing Astrid. Konrad is a similar instrument, Stoew et al. (2000) is now added in section 2.5

line 20 It took a while to understand, that "Sect. 3.3" refers to this publication and not to the publication of Elgered and Jarlemark (1998). Please append the sentence with'In Sect. 3.3 of this publication we describe the use ...' or similar to spare the reader a bit of flipping to and fro. This is now reformulated.

Page 322
HITRAN 2004 is used in this study for the line parameters. Why not using one of the later catalogs, i.e. HITRAN 2008 or HITRAN 2012? Please justify. It should be a simple exercise to exchange the spectral data base and rerunning the whole time series.

The spectral data used is actually from a database compiled to optimize the advantages of the HITRAN and JPL databases. However, combining the two databases is non-trivial since atmospheric isotope ratios and differences in the definition of the partition function of the two databases. For the 110.8 GHz Ozone line the broadening parameters are actually taken from Connor 1986, and this reference has now been added.

We have used this set of spectroscopic parameters in the previous iteration of the instrument (Forkman, 2012), and they have been used by other instruments as well (Fernandez, 2015). Thus, to facilitate the extension of our current time series, and comparison to other instruments we choose to use the old spectroscopic data.

We do however recognize that the uncertainties in the spectroscopic parameters do leads to an uncertainty in the retrieved values. In the previous draft there was an error in figure 10 which led to an underestimation of this uncertainty. This has now been corrected, and in particular for Ozone in the lower mesosphere the estimated uncertainty has increased.

Page 323, line 15ff: Are you using an iteration method for solving this equation or do you assume a linear forward model? In the previous version of the manuscript we used a linear method to solve the retrieval equation. However, since the troposphere is directly included in the state vector, the problem is slightly non-linear, and we have now replaced this linear method with an iterative approach using the Gauss-Newton method, and updated the manuscript to reflect this. This change did not change the retrieved results in any noteworthy way.

Page 323, Line 1: The baseline ripple is often caused by a Fabry-Perot effect (In the Conclusion you write: 'Standing waves arising from reflections...') in the optical path and is described as a cos function. I would not consider a polynomial appropriate to model such a function. Why do you not use sinoids to model the baseline ripple, especially because it is straight forward to include it in the forward model and also in the K-matrix. Please add a section showing the spectrum with and without the modeled baseline ripple and its effect to the retrieved profiles. In conclusions we mention that standing waves arising from reflections in the transmission line affect our sideband ratio measurements. These reflections originates from the non-ideal matching between the different components used in this investigation.
In our measured spectra we do not see a sinusoidal baseline and hardly any baseline features at all. The baselines are now added in figure 7a.

Page 324 line 16ff
I would expect the spectrometer to exhibit spectral leaking, i.e. the spectrometer channels have a response function which extends over more than one channel. Is this accounted for by providing a correlation between channels or is the spectral leaking modeled separately in the forward model?
We mention the correlation between neighbor channels due to the Hanning window applied. Test signal measurements have given that we have no other leaks. The spectral response of each channel due to this Hanning filter is taken into account in the forward model as described in at page 322, line 13. Furthermore, this cross channel correlation is taken into account in the error covariance matrix as described in the last paragraph of section 3.2.

page 327 line 11-18.
I think this explanation, that the CO profile reflects the movement of the air is a bit short. Especially in summer, I doubt that at 57N the reversal of the residual circulation is measured, but rather the CO poor air in mid-latitudes. The variations on a daily base and shorter may be caused by movements of the polar vortex, but other causes are already possible, e.g. the effect of gravity waves.
We agree, our text was to simplified, we have now expanded this section

Page 328 ff
I do not fully understand the error discussion. What do the authors mean by accuracy and precision (I know the concepts, but can not understand how they derive those figures). We have now changed the wording from accuracy and precision to systematic and random errors. We have also added a line explaining the meaning of these two words.

Page 329
I would think that errors spectroscopy provides also cause a large systematic uncertainty, possibly even larger. In the light of the authors former statement, that the line positions of the O3 line is off by a fair amount, I would hesitate to put too much trust into the other line parameters.
There is definitely uncertainty in the spectroscopic parameters, we have included our best guess error in our error analysis. This error estimate is either based on the uncertainty given by HITRAN, or the differences between our values and HITRAN 2012. For our estimate we have used the largest of these two error estimations. It is our opinion that this is as good an estimate we can get without explicitly evaluating the different spectroscopic methods used, which is beyond the scope of this paper.

Figure 8: Comparing the upper panel of figure 8 (CO timeseries) with the AVK of CO in figure 9, I wonder where the enhancement in 90 km is really appearing. The AVK rather show, that the instrument is not sensitive at this altitude. Exactly where the changes comes from is unfortunately not possible to say due to the ambiguity caused by the Doppler dominated line at these altitudes. A line commenting on this ambiguity has now been added to Section 4.

Hoffmann et.al. (2011) discuss very detailed the interpretation of the AVK and results from ground based millimeterwave radiometry. Especially the problem of the nonuniqueness of the Voigt profile due to the strong temperature broadening from higher altitudes is not mentioned there. Please include and discuss there findings with respect to your CO results.

The non-uniqueness of the Voigt profile means that changes in CO at higher altitudes (above 110 km) can be interpreted by the retrieval as changes at lower altitudes. As Hoffmann 2011 shows in figure 5, the 120km AVK is highly influenced by changes (in unit vmr) at 70 km while the opposite is not true.

In fact the two major physical properties determining to what the degree changes at 120 km affect the retrieved value at 70 km is the number density of CO molecules, and the temperature since these two parameters in the end determine the amount of radiation emitted from an atmospheric layer.

To our best knowledge, the number density at 120 km is orders of magnitude smaller than at 70 km due to the lower pressure. We base this assumption on current atmospheric models (WACCM) and retrieved data from Odin-SMR (valid up to ~105 km). This means that for any major cross contamination to occur, the molecules at 120 km must emit stronger than those at 70 km. However, since the CO line measured is a ground state line, the line intensity actually decreases with increasing temperature (See e.g. Eriksson and Merino, 1997). We therefore regard it as unlikely that this ambiguity has any practical implications for the values below 80 km.

Hoffmann et. al. (2011) present extensive work on the comparison of CO measured by MLS and ground bases millimeterwave radiometry. Please relate your discussion to the results presented in this work. Since only one satellite sensor is used we believe that a thorough discussion about CO validation (as described in Hoffmann et al. 2011 and Forkman et al. 2012) is beyond the scope of this paper. The work of Hoffmann et al. 2011 is mentioned in section 6.

Page 331 line 11:
I would think, the most severe drawback of the frequency switching method is the small bandwidth, with restricts the measurements to the upper stratosphere and mesosphere only. In both Introduction and Summary the advantages and drawbacks of a frequency switching compared to load and sky switching are discussed. The text in the Introduction has been expanded

Page 331 line 21 - 26
At least Palm (2010) and Hoffmann (2011) do not use a single absorption to model the troposphere but use a model similar to the one presented here in order to adjust for the tropospheric attenuation in their retrievals. They also include the troposphere in the forward model and retrieve its absorption simultaneously with the O3 or CO profiles. We agree that wording in section Summary was miss-leading. This is now changed.

Technical comments:
Page 322 Line 13 ’a channels response’ -> ’a channel response’ Corrected
Page 325 line 20: ’Both these values ...’ -> ’Both values ...’ Corrected
Page 327 line 11: ’...cover...’ -> ’...covers...’ Corrected
Figure 8 The title of the upper figure is clipped Corrected

The answers to Referee 2

Trustable altitude range:
The authors claim that data are useful for an altitude range where the contribution from the a-priori profile is less than 20%, i.e. where the measurement response is >80%. The measurement response is equal to the area under the averaging kernels. In case of CO retrieval these kernels show distinctive problems. There is a strong negative part for lower altitudes. The authors claim that this is not critical as at these altitude changes in the VMR profile of CO are not expected and values in VMR is small.

Unfortunately the wavering kernels also suffer from another problem. The park of the kernel significantly deviates from the nominal altitude and in fact none of the kernels parks above 80km as can clearly be seen in Figure 9. The plot of the measurement response and of the kernels in this same figure clearly shows that according the definition of the authors data are usable up to an altitude of approx. 93km (left part of figure). On the other hand it is clear that the kernels practically have no contribution. Misleading also is the white line in Figure 8 indicating the same problem of the measurement response. In some occasions it even goes to an altitude of 100km where definitely Doppler-broadening does not allow to retrieve any meaningful information.

The authors must deal with this problem. It is not sufficient to merely refer to a previous work by Hoffmann saying that this is a typical behavior of the CO retrieval. I would like to see a detailed discussion with information about where the kernels peak and the usefulness of the measurement response in this context.
The measurement response (as classically defined) answers the question of what part of our retrieved profile is sensitive to changes in the true atmosphere. As the reviewer writes, it does not give any information from where this influence comes.

For species where the change at one altitude can be assumed to be of roughly the same size as changes at another altitudes (withing the vertical resolution of the instrument) the position of the peak of the averaging kernel, and the corresponding measurement response is relatively straightforward to interpret.

However, for gases with a strong vertical gradient the analysis is a bit more complicated. The reason for this is that a large deviation from the apriori (in terms of vmr) is much less likely at lower altitudes than at higher. Thus, an optimal retrieval method (in terms of aposteriori error) does not necessarily peak at the nominal altitude.

To take into account this changing variability with altitude, species with a high vertical gradients can be constrained (through the apriori covariance matrix) using a relative units, i.e. the assumed variation around the apriori is proportional to the apriori itself as done in this paper, or letting the diagonal elements of Sa vary with altitude (as done in Hoffmann, 2012) or a mixture of both (Forkman, 2012).

To make this clearer we now show relative AVKs in our diagnostic plots for CO and describe the consequences of using a relative constraint in the text. This relative AVK matrix (and the measurement response given by the sum of its rows) is now used for determining valid heights for our data. We do however wish to keep the error analysis and presentation of the results etc. to vmr units as this is the most commonly retrieved unit for other profiling instruments.

In light of this discussion we do want to stress that the measurement response, and peak of AVKs provide merely a guideline for the end user. Any later scientific use of the data should take the structure of the complete averaging kernel matrix into account.

Tropospheric correction:
I have read this paragraph several times but have not understood how the correction is done. I do not understand what is described on p. 326. The whole process with the random number r is at least for me not understandable. Please reword this whole paragraph in a way it is more clear what you do. Explain why you do not use just the information from one of the two dual-channel radiometers. What is the advantage of this information about the fractional cloud cover if you observe in one direction.

The cloud cover needed to be parametrized, as the amount of liquid water expected over the OSO cite does not only depend on the mean LWC from ERA-interim but how this is distributed across within the grid box. The exact details of this parametrization is not critical for the results presented in this paper, and we have now removed this explanation and replaced it with a more general description of our approach.

The dual channel radiometers did not operate continuously during the time period presented in this study, and since we cannot guarantee the future operation we wanted to have a method independent of these radiometers. Hence using a database based on ERA-interim, corrected using the two radiometers was chosen. We did however wanted to use the days where both the dual channel radiometers and the spectrometer was operating to test our sensitivity to changes in the tropospheric attenuation, and hence they are used in Sec 5.

Further comments:
Observations are taken at an elevation angle of 80. Please indicate why this selection was made.
The spectral resolution is 25 kHz. Discuss this resolution in context with the Doppler broadening.
The highest signal to noise ratios of the observed mesospheric emission from both CO and O3 are found at observation elevations larger than about 40 degrees. To avoid Doppler shift effects due to zonal winds in the middle atmosphere an elevation as close to the zenith direction as possible is preferable. To get close to zenith but to avoid reflections from the housing structure an elevation of 80 degrees is chosen. The 25 kHz resolution is good enough, as the smallest line-widths expected from the CO and O3 line measured due to Doppler broadening has full width, half maximum values of 220 kHz and 160 kHz respectively. This text is now added in section 2.

Technical comments:
p. 318, eq.(10): say that this is the classical Y-factor measurement Corrected
p. 320, l.18: CW source is connected to the radiometer Corrected
p. 321, l. 4 and 9. Please indicate how glsb and GL and gusb and GU are related Added
p. 325, l. 26: constructed of data Corrected
p. 326, l. 4: say what LWC is Added
p. 328, l. 3 and 4 I think in order to give the degree of freedom one should not use the sign for degree. Corrected

Manuscript prepared for Geosci. Instrum. Method. Data Syst.
with version 2014/09/16 7.15 Copernicus papers of the LaTeX class copernicus.cls.
Date: 23 December 2015

A compact receiver system for simultaneous measurements of mesospheric CO and O_3

P. Forkman[1], O. M. Christensen[1], P. Eriksson[1], B. Billade[1], V. Vassilev[2], and V. M. Shulga[3]

[1]Department of Earth and Space Sciences, Chalmers University of Technology, Sweden
[2]Department of Microtechnology and Nanoscience, Chalmers University of Technology, Sweden
[3]Institute of Radio Astronomy, Ukrainian Academy of Sciences

Correspondence to: P. Forkman (peter.forkman@chalmers.se)

Abstract. During the last decades, ground-based microwave radiometry has matured to an established remote sensing technique for measuring vertical profiles of a number of gases in the stratosphere and the mesosphere. Microwave radiometry is the only ground-based technique that can provide vertical profiles of gases in the upper stratosphere and mesosphere both day and night, and even during cloudy conditions. Except for microwave instruments placed at high altitude sites, or at sites with dry atmospheric conditions, only molecules with significant emission lines below 150 GHz, such as CO, H_2O and O_3 can be observed. Vertical profiles of these molecules can give important information about chemistry and dynamics in the middle atmosphere.

Today these measurements are performed at relatively few sites, more simple and reliable instrument solutions are required to make the measurement technique more widely spread. This need is today urgent as the number of satellite sensors observing the middle atmosphere is about to decrease drastically. In this study a compact double-sideband frequency-switched radiometer system for simultaneous observations of mesospheric CO at 115.27 GHz and O_3 at 110.84 GHz is presented.

The radiometer, its calibration scheme and observation method are presented. The retrieval procedure, including compensation of the different tropospheric attenuation at the two frequencies, and error characterization are also described. The first measurement series from October 2014 until April 2015 taken at the Onsala Space Observatory, OSO, (57° N, 12° E) is analysed. The retrieved vertical profiles are compared with co-located CO and O_3 data from the MLS instrument on the Aura satellite. The datasets from the instruments agree well to each other. The main differences are the higher OSO volume mixing ratios of O_3 in the upper mesosphere during the winter nights and the higher OSO volume mixing ratios of CO in the mesosphere during the winter. The low bias of mesospheric winter values of CO from MLS compared to ground-based instruments has been reported earlier.

1 Introduction

Simultaneous measurements of mesospheric gases with different chemical lifetimes, such as ozone (fraction of hour) and carbon monoxide (order of weeks), can give important information on both chemical and dynamical processes in this altitude region. The middle atmospheric distribution of ozone, O_3, is characterized by a stratospheric volume mixing ratio (vmr) peak at $\sim 35\,\mathrm{km}$ altitude, first described by Chapman (1930), and a diurnally varying secondary mesospheric peak at $\sim 90\,\mathrm{km}$ altitude (Hays and Roble, 1973). The secondary peak is formed during night by reactions between atomic and molecular oxygen and partly destroyed by photo-dissociation during day. Additionally, a tertiary, also diurnally varying, peak is present at $\sim 72\,\mathrm{km}$ in winter at high latitudes (Marsh et al., 2001; Hartogh et al., 2011).

The main source of middle atmospheric carbon monoxide, CO, is photo-dissociation of carbon dioxide, CO_2, in the upper mesosphere/thermosphere region. Reactions with hydroxyl, OH, is the main sink. Low vmr in the stratosphere, significantly increasing values with altitude up through the mesosphere, and high values in the thermosphere is the typical vertical distribution of middle atmospheric CO (Lopez-Puertas et al., 2000).

The vertical component of the mesospheric dynamics can at high latitudes be described as an annual cycle with air ascending in the summer and descending in the winter. The horizontal component is weak during summer, while it is controlled by the polar vortex and stronger during winter (Brasseur and Solomon, 2008). Due to its long lifetime in the mesosphere CO is an excellent tracer of dynamics in this altitude region, especially at high latitudes during winter (Hoffmann, 2012).

Microwave radiometry is the only ground-based remote-sensing technique that both day and night, even during cloud cover, can provide vertical profiles of different trace gases up to the mesopause region. In microwave radiometry, emission spectra from rotational transitions within the observed molecular species are measured. Due to pressure broadening, the measured spectra contain information about the vertical distribution of the molecule. Except from very dry sites, or sites at high altitudes, only frequencies up to about 150 GHz can be observed since higher frequencies are effectively attenuated by tropospheric water (Janssen, 1993). The gases CO, H_2O, O_2 and O_3 all have sufficiently strong emissions at frequencies below 150 GHz. Thus, there is a need for simple and reliable radiometers operating below 150 GHz, since they can observe important gases from almost every ground-based site. If such a radiometer could also observe two of the gases simultaneously (e.g. O_3 and CO) it would be even more useful for the microwave community.

Dicke-switching is the generally used observation technique in microwave radiometry, meaning that the radiation from the sky is compared to an equally intense reference source to diminish the effects of gain variations. Three main Dicke-switching variants can be recognized. In load-switching the reference is a blackbody or other noise source. The zenith sky is the reference in sky-switching. In frequency-switching the mixer's local oscillator frequency, LO, is changed between the signal and the reference phases. Parrish (1994) gives an overview of the mentioned observation methods.

Since the pioneering work by Caton et al. (1968) several heterodyne radiometer systems dedicated for middle atmospheric O_3 observations have been developed, primarily for the relatively strong O_3 transitions at 110.8 and 142.2 GHz. Lobsiger (1987) developed a load-switching technique where the sky, a liquid nitrogen cold load at 80 K, and an ambient load were measured during each observation cycle; several 142.2 GHz instruments use variants of this method (Hartogh et al., 1991; Peter et al., 1998; Hocke et al., 2007; Palm et al., 2010; Moreira et al., 2015). Recently the technique has been developed further by implementing a noise diode and a Peltier cooled load (Fernandez et al., 2015).

Parrish et al. (1988) and Parrish et al. (1992) developed a sky-switching procedure at 110.8 GHz where the reference zenith beam passes a "lossy" window at Brewster angle to compensate for the higher intensity in the signal beam. This observation technique has been widely used, for example by Connor et al. (1994), Boyd et al. (2007) and Nedoluha et al. (2015).

The drawback of load and sky switching is that a reference is observed during half the observation time. The advantage of frequency-switching is that the wanted sky emission is present in both signal and reference, which doubles the effective observation time compared to load or sky switching. The drawback is that the frequency dependent impedances in the frontend components can change the overall gain between the signal and reference phases if the frequency throw is more than ~ 30 MHz. As the pressure broadening in the stratosphere exceeds the bandwidth limitation of frequency-switching this method can only be used for studies of mesospheric and upper stratospheric O_3. However, narrow mesospheric lines can be resolved with a higher temporal resolution using a frequency switched configuration compared to load or sky switching due to the efficient time usage. Nagahama et al. (1999) used a frequency throw of 30 MHz and presented vertical O_3 profiles in the altitude range 30–80 km.

Microwave spectra of CO are much narrower than spectra of O_3 due to the different residence altitudes for the two molecules, which make frequency-switching suitable. Waters et al. (1976) made the first microwave CO observations, using absorption measurements against the sun and on-source off-source switching (the standard Dicke method used by radio astronomers). Kunzi and Carlson (1982), Aellig et al. (1995), Forkman et al. (2003) and Forkman et al. (2012) made frequency-switched observations of CO at 115.3 GHz. de Zafra and Muscari (2004), Hoffmann et al. (2011) and Straub et al. (2013) used load-switching to observe CO at 230.5 GHz.

The mixer is the key component in the heterodyne radiometer. The incoming radio frequency, RF, is mixed with the LO, and the output intermediate frequency, IF, is a mix of the upper and lower sidebands. To avoid the unwanted sideband (or image band) the radiometer can be operated in single sideband mode where the image band is suppressed before the mixing. If none of the sidebands are suppressed, we have a double-sideband system which makes it possible to observe signals from the two bands simultaneously. The disadvantages are that the sideband ratio has to be known and the tropospheric attenuation has to be corrected individually for the two bands if the tropospheric opacity differ between the two frequencies. Except for instruments where the LO is placed on the

center of the observed line, e.g. the 183 GHz water vapor radiometer for the ALMA project (Emrich et al., 2009), most ground-based radiometers today are single sideband instruments. One exception is the 110–116 GHz radiometer for CO and O_3 observations designed and operated by Piddyachiy et al. (2010).

In this study we present the first simultaneous measurements of mesospheric O_3 at 110.8 GHz and CO at 115.3 GHz made by a ground-based, double sideband and frequency-switched radiometer system. The system is operated at the Onsala Space Observatory, OSO, (57.4° N, 11.9° E). The instrument, its calibration scheme, the retrieval procedure and the first results are introduced. Section 2 describes the receiver system and the calibration and Sect. 3 presents the inversions. The results are given in Sect. 4 and the error analyses is described in Sect. 5. Section 6 shows a satellite comparison, and Sect. 7 gives a summary and the conclusions.

2 Instrument and observation technique

We present a double-sideband, frequency-switched heterodyne receiver system for simultaneous spectral measurements of the atmospheric O_3 $6_{15} \rightarrow 6_{06}$ transition at 110.836 GHz and the CO $1 \rightarrow 0$ transition at 115.271 GHz. Model calculations show that the highest signal to noise ratios of the observed mesospheric emission from both CO and O_3 are found at observation elevations larger than $\approx 40°$. To avoid Doppler shift effects due to zonal winds in the middle atmosphere an elevation as close to the zenith direction as possible is preferable. To get close to zenith but to avoid reflections from the housing structure an elevation of 80° was chosen. A 2-bit autocorrelator is used as backend spectrometer. The bandwidth is 20 MHz and the nominal resolution is 25 kHz (800 delay channels). This resolution is sufficient as the smallest line-widths expected from the CO and O_3 line measured due to Doppler broadening has full width, half maximum values of 220 kHz and 160 kHz respectively. A block diagram of the receiver is shown in Fig. 1 and technical specifications are given in Table 1.

2.1 Frontend description

The receiver frontend includes a four stage Low Noise Amplifier, LNA, a fundamental resistive mixer, and a $\times 4$ LO chain, all integrated onto a single Monolithic Microwave Integrated Circuit, MMIC, using a 100 nm mHEMT process. The mixer provides a conversion loss of 8–10 dB for LO power of 4 dBm. The LO chain consists of two doublers followed by a two stage power amplifier. The amplifier delivers about 5 dBm of LO signal to the mixer with an input power of 9 dBm at 29.5 GHz. Vassilev et al. (2010) gives more details on the performance of the receiver and a breakout of the LNA.

2.2 Calibration

Brightness temperature, $T_{\rm b}$, derived from the Rayleigh-Jeans approximation of the Planck law, is often used as a measure of the received radiation in microwave radiometry. The Rayleigh-Jeans approximation can be written:

$$B(\lambda,T) \approx \frac{2kT}{\lambda^2} \tag{1}$$

where B is the brightness describing the energy emitted by a black body, λ the wavelength, k the Boltzmann constant, and T the physical temperature of the black body. Equation (1) is valid when $h\nu \ll kT$, where h is the Planck constant and ν is the frequency. The brightness temperature, $T_{\rm b}$, is defined as:

$$T_{\rm b} = I(\lambda)\frac{\lambda^2}{2k} \tag{2}$$

The proportionality between the received radiation, I, and $T_{\rm b}$ is the reason why $T_{\rm b}$ is used in microwave radiometry. The antenna temperature, $T_{\rm a}$, is defined as the convolution between the observed brightness temperature distribution and the antenna pattern. In the rest of this section a pencil beam is assumed implying that the measured antenna temperature, $T_{\rm a}$, is equal to the brightness temperature, $T_{\rm b}$, in the observed direction.

The system temperature, the radiometer output power measured by the spectrometer, is defined as $T_{\rm sys} = T_{\rm a} + T_{\rm rec}$, where the receiver temperature, $T_{\rm rec}$, is a measure of the power generated in the components along the radiometer system transmission line where the first stages as LNA and mixer contribute the most.

In the mixer, the RF input spectrum is folded around the LO to form the IF output spectrum (see Fig. 2). The IF bandpass filter selects the position and width of both the lower sideband, LSB, and the upper sideband, USB. If any of the two sidebands are terminated ahead the mixer the receiver is called single sideband, SSB. We use the mixer in true double sideband mode, DSB, where LSB is centered at 110.84 GHz and USB at 115.27 GHz, see simulated spectra in Fig. 3. The contributions from LSB and USB are weighted with their relative frontend gains and then added to form $T_{\rm sys}$ (Ulich and Haas, 1976). The system temperature of a calibration blackbody load that fills the antenna beam, $T_{\rm sys}(load)$, can thus be expressed as:

$$T_{\rm sys}(load) = G_{\rm L}\Big(T_{\rm load}(L) + T_{\rm rec}(L)\Big) + G_{\rm U}\Big(T_{\rm load}(U) + T_{\rm rec}(U)\Big) \tag{3}$$

where L and U mark the contributions from the LSB and USB frequencies, $G_{\rm L}$ and $G_{\rm U}$ are the normalized relative frontend power gains ($G_{\rm L} + G_{\rm U} = 1$) in the two sidebands (also called sideband responses), and $T_{\rm load}$ is the temperature of the blackbody load. The sum of the two contributions to the receiver temperature is denoted $T_{\rm rec}$, i.e. $T_{\rm rec} = G_{\rm L}T_{\rm rec}(L) + G_{\rm U}T_{\rm rec}(U)$. If it is assumed that

the load is a blackbody in both sidebands, Eq. 3 is hence simplified to:

$$T_{\rm sys}(load) = T_{\rm load} + T_{\rm rec} \tag{4}$$

To estimate $T_{\rm rec}$ two blackbody loads with physical temperatures $T_{\rm hot}$ (ambient load) and $T_{\rm cold}$ (77 K load) are observed each month. $T_{\rm rec}$ can then be estimated using:

$$\frac{P_{\rm cold}}{P_{\rm hot} - P_{\rm cold}} = \frac{T_{\rm sys}(cold)}{T_{\rm sys}(hot) - T_{\rm sys}(cold)} = \frac{T_{\rm cold} + T_{\rm rec}}{T_{\rm hot} - T_{\rm cold}} \rightarrow T_{\rm rec} = P_{\rm cold}\frac{T_{\rm hot} - T_{\rm cold}}{P_{\rm hot} - P_{\rm cold}} - T_{\rm cold}, \tag{5}$$

which is the classical Y-factor method, where $P_{\rm hot}$ and $P_{\rm cold}$ are the measured powers observing the two loads. The system temperature when observing the sky, $T_{\rm sys}(sky)$, is given by:

$$T_{\rm sys}(sky) = G_{\rm L}T_{\rm a}(L) + G_{\rm U}T_{\rm a}(U) + T_{\rm rec} \tag{6}$$

where $T_{\rm a}(L)$ and $T_{\rm a}(U)$ are the antenna temperatures at 110.84 GHz and 115.27 GHz, respectively.

The following calibration procedure is performed each 15 minutes to estimate the sky brightness temperature:

$$\frac{P_{\rm load} - P_{\rm sky}}{P_{\rm sky}} = \frac{T_{\rm sys}(load) - T_{\rm sys}(sky)}{T_{\rm sys}(sky)} = \frac{\left(T_{\rm load} + T_{\rm rec}\right) - \left(G_{\rm L}T_{\rm a}(L) + G_{\rm U}T_{\rm a}(U) + T_{\rm rec}\right)}{G_{\rm L}T_{\rm a}(L) + G_{\rm U}T_{\rm a}(U) + T_{\rm rec}}, \tag{7}$$

where $P_{\rm load}$ and $P_{\rm sky}$ are the measured powers observing the load and the sky, respectively. The weighted mean of the antenna temperatures at the two sidebands,

$$T_{\rm sky} = G_{\rm L}T_{\rm a}(L) + G_{\rm U}T_{\rm a}(U) \tag{8}$$

can be derived from Eq. 7 since $T_{\rm load}$ and $T_{\rm rec}$ are known. Since a pencil beam is assumed, $T_{\rm sky}$ is denoted as sky brightness temperature (see above). An error in the estimate of $T_{\rm rec}$ introduces an error in the estimation of $T_{\rm sky}$. The hot-cold calibrations (Eq. 5) performed so far indicate that the variation in $T_{\rm rec}$ is less than 3 %. Equations 7 and 8 then gives that the error in $T_{\rm sky}$ is less than 2 %.

The sky brightness temperature at 115.3 GHz is 35–60 K higher than at 110.8 GHz. This is explained both by the frequency variation of absorption due to tropospheric water and by the fact that 115.3 GHz is situated higher on the wing of the 118 GHz O_2 line, see the broadband spectra in Fig. 4 estimated from one year of radiosonde data taken at Landvetter Airport, 38 km N.E. of Onsala Space Observatory.

2.3 Frequency-switching

The particular Dicke-switch method used here is frequency-switching. In this method the frontend mixer LO frequency, f_{LO}, is switched between the phases of the signal, S, and the reference, R, in the measurement cycle. $f_{LO}(S) = f_c - \Delta f$ and $f_{LO}(R) = f_c + \Delta f$ where f_c is the mean of the two local oscillator frequencies. Owing to $S - R$ being a difference, the spectra will show both a negative and a positive peak in the observed spectral characteristic, with a separation equal to the

frequency throw, $2\Delta f$. An averaged spectrum is seen in Fig. 5. The spectrum is a combination of double-sideband measurement and frequency-switching which explains the positions of the negative and positive peaks of O_3 from the lower and CO from the upper sidebands.

Using frequency-switching during the observation cycle we record

$$\begin{aligned}\Delta T_{\rm sky} &= \frac{\Delta P}{P_{\rm load} - P_{\rm sky}}(T_{\rm load} - T_{\rm sky}) = T_{\rm sky}(-\Delta f) - T_{\rm sky}(+\Delta f) \\ &= G_{\rm L}\big(T_{\rm a}(L,-\Delta f) - T_{\rm a}(L,+\Delta f)\big) + G_{\rm U}\big(T_{\rm a}(U,-\Delta f) - T_{\rm a}(U,+\Delta f)\big) \end{aligned} \quad (9)$$

where $\Delta T_{\rm sky}$ is the difference in brightness temperatures (since we assume a pencil beam) and $\Delta P = P_{\rm S} - P_{\rm R}$ is the difference in the measured powers between the two frequencies $f_{LO}(S)$ and $f_{LO}(R)$. The calibration procedure gives $P_{\rm load}$, $P_{\rm sky}$, $T_{\rm load}$ and $T_{\rm sky}$.

2.4 Sideband ratio

The sideband responses G_L and G_U have to be known accurately to be able to retrieve vertical profiles from the measured spectra. The measurement of the sideband responses relies on inserting a continuous wave (CW) of known amplitude in the RF path of the instrument and to measure the down converted IF signal. The measurement is then repeated over several RF/IF frequencies to get the overall sideband response.

Figure 6 shows the setup used for the measurement of the sideband response of the instrument. A millimeter wave source generates a CW in the 110.5 - 115.5 GHz frequency band. A mm-wave spectrum analyzer extender measures the amplitude of the CW signal. The radiometer frontend, and a spectrum analyzer measure the amplitude of the down converted IF. All the measurement equipments are synchronized to a common reference clock.

In the current measurement setup, the mm-wave source is first connected to the extenders to measure the amplitude of the CW signal while sweeping the source frequency $f_{\rm RF} = 110.5 \rightarrow 115.5$ GHz. After taking the RF power sweep, the CW source is connected to the radiometer, and the amplitude of the down converted IF is recorded while sweeping the RF frequency as before. The local oscillator frequency of the radiometer is held constant at $f_{\rm LO} = 113.055$ GHz (28.26375×4). The two sidebands after the IF amplifier bandpass response are,

$$\begin{aligned} f_{\rm LSB} &= 113.055 - (1.5 \rightarrow 2.5) = 110.555 \rightarrow 111.555 \text{ GHz} \\ f_{\rm USB} &= 113.055 + (1.5 \rightarrow 2.5) = 114.555 \rightarrow 115.555 \text{ GHz} \end{aligned} \quad (10)$$

The sideband gains of the instrument can then be estimated by taking the ratios of the measured power at RF frequencies and IF frequencies as,

$$g_{\rm LSB} = \frac{P_{\rm IF}^{\rm LSB}}{P_{\rm RF}^{\rm LSB}} \quad \text{and} \quad g_{\rm USB} = \frac{P_{\rm IF}^{\rm USB}}{P_{\rm RF}^{\rm USB}} \quad (11)$$

The measured sideband ratio, $g_{\rm LSB}/g_{\rm USB}$, is close to unity. However, standing-wave patterns are seen in both the measured RF and IF powers, which introduce an error in our estimation of

the sideband ratio. These standing waves have to be minimized in order to improve the quality of the measurements. Nevertheless, the results obtained so far with the current setup are promising. The linear normalized relative frontend power gains, $G_{\mathrm{L}} = g_{\mathrm{LSB}}/(g_{\mathrm{LSB}} + g_{\mathrm{USB}})$ and $G_{\mathrm{U}} = g_{\mathrm{USB}}/(g_{\mathrm{LSB}} + g_{\mathrm{USB}})$ are estimated at 0.5 ± 0.05 and 0.5 ∓ 0.05 respectively.

2.5 Water vapor radiometer for tropospheric measurements

Due to the nature of DSB mixers, the measured sky brightness temperature is the mean of the brightness temperatures at the lower and upper sideband frequencies, weighted with their respectively sideband gains G_{L} and G_{U}. To be able to correct for the tropospheric attenuation an estimation of the sky brightness temperatures at these two frequency regimes are needed. The OSO site operates two dual-frequency radiometers, ASTRID (Elgered and Jarlemark, 1998) and KONRAD (Stoew et al., 2000), that continuously measure the sky brightness temperature in different directions at 21.0 / 31.4 GHz and 20.6 / 31.6 GHz respectively, see Table 2. The data is used to provide independent corrections for the water vapor induced time delay which affect the accuracy of the geodetic VLBI observations performed at the observatory (Elgered and Jarlemark, 1998). For our purpose, the calibrated zenith sky brightness temperatures, from these instruments will be used in Section 3.3 to estimate the tropospheric opacity at 110.84 and 115.27 GHz.

3 Retrievals

3.1 Forward model

For the retrievals presented in this paper, the Atmospheric Radiative Transfer Simulator (ARTS v.2.3.145) is used as a forward model (Buehler et al., 2005; Eriksson et al., 2011). It is a general radiative transfer model that can provide Jacobians for a large number of different measurement geometries and systems. A 1-D simulation setup is applied using a pressure grid ranging from $1.3 \cdot 10^5$ Pa (0 m) to $7.5 \cdot 10^{-4}$ Pa ($\sim$130 km) with a spacing of $\sim$250 m. Line-by-line simulations of frequencies in two bands between 110.816-110.856 GHz and 115.251-115.291 GHz are run with a monochromatic frequency grid having a spacing of 4.2 MHz at the far end of each band, decreasing to 14.13 kHz in the center of each band. The instrument is modeled as a dual sideband receiver with a flat 50% sideband response in each band. Each channel of the autocorrelator is modeled to have a channel response corresponding to an ideal Hanning filter with a FWHM of 50 kHz. The antenna is modeled as a pencil beam antenna looking at a zenith angle of 10°, and the instrument is positioned at ground level.

The spectroscopic lines included in the forward model are CO at 115.27 GHz, $\mathrm{O_3}$ at 110.77, 110.84, 111.05 and 114.97 GHz as well as complete absorption models for oxygen, nitrogen, water vapour and liquid water (Table 3). The spectrocopic parameters are taken from an updated version of the Verdandi database (Eriksson and Merino, 1997). Line positions and strengths of the database

are mainly taken from the JPL-catalogue (Pickett et al., 1998), while the broadening parameters are mainly taken from HITRAN. The discussed version of Verdandi was created 2002, using the JPL data of that time and HITRAN 2001 (Rothman et al., 2003). For a number of transitions the JPL and HITRAN data are replaced with hand-picked data from the literature. This includes the O_3 line at 110.84 GHz, where the presssure broadening parameters are taken from (Connor and Radford, 1986). A summary of the spectroscopic parameters is given in Table 4.

When comparing the measurements to a forward model simulation with the line positions from the JPL-catalogue, the simulated CO emission occurs at the same frequency in both the simulation and our measurements, while the simulated O_3 line emission at 110.8360400 GHz shows a clear frequency offset compared to the measurements. Since the CO line is positioned correctly a shift in the LO frequency cannot explain the frequency offset of the O_3 line. This indicates that the databases have the wrong frequency for this spectral line. Best agreement between the forward model and measurement was found if the line was shifted 117 kHz (specified uncertainty is 50 kHz) to 110.8359230 GHz. Note that for the purpose of this study, the exact reason for this shift is not relevant, since a pure shift in frequency does not affect the retrieved concentrations as long as the modeled and measured spectra are consistent.

3.2 Retrieval model

To retrieve CO and O_3 concentrations from the measured spectra, the maximum a posteriori method, also called optimal estimation method, OEM, (Rodgers, 2000) is used as implemented in the updated version of the Qpack software (Eriksson et al., 2005). Given the spectra with assumed errors and a statistical distribution of the measured atmosphere, the method returns the maximum a posteriori estimate combining these two pieces of information. If the atmosphere and possible instrument parameters are described by a state vector $\mathbf{x}$, the measured spectrum by $\mathbf{y}$, and the a priori atmosphere as $\mathbf{x_a}$, the estimated atmosphere is

$$\hat{\mathbf{x}} = \mathbf{x_a} + (\mathbf{K^T S_\epsilon^{-1} K} + \mathbf{S_a^{-1}})\mathbf{K^T S_\epsilon^{-1}}(\mathbf{y} - \mathbf{K x_a}), \tag{12}$$

where $\mathbf{S}_\epsilon$, $\mathbf{S_a}$ are the covariance matrices describing the uncertainty (assuming normal distribution) in the measurements and a priori atmosphere respectively. The Jacobian- or Weighting function matrix, $\mathbf{K} \equiv \partial \mathbf{y}/\partial \mathbf{x}$, is the linearized derivative of the forward model and describes how a change in any of the state vector elements influences the measured spectrum. Tropospheric attenuation introduces a non-linearity in Eq. 12, i.e. $\mathbf{K}$ is a function of $\mathbf{x}$. To account for this Eq. 12 is solved iteratively using a Gauss-Newton method, and convergence is concidered to be reached when the change in the state vector betweem two iterations, normalized by the retrieved covariance, is less than 0.01 times the length of the state vector.

To save computational resources, the inverse problem (Eq. 12) is solved on a coarser grid than the forward model. The state vector is specified to contain the concentration of CO as a fraction of the

apriori profile and the concentration of O_3 in vmr at pressure levels between $1 \cdot 10^5$ Pa and $1 \cdot 10^{-3}$ Pa with a spacing of 2 km. In addition to CO and O_3, the state vector includes the concentration (in units relative to the a priori) of water vapor and liquid water between $1 \cdot 10^5$ Pa and $1.3 \cdot 10^3$ Pa with a spacing of 1 km. These species are included to correct for tropospheric influence on the mesospheric emission (see Sec. 3.3). The elements of the state vector containing these species are referred to as $\mathbf{x^{trop}}$. To account for baseline ripple in the instrument a 3^{rd} order polynomial fit is performed, and its coefficients are stored in the four last elements of the state vector.

Each of these state vectors variables needs a priori values stored in $\mathbf{x_a}$. The a priori profile for CO and O_3 is based on a climatology containing the monthly zonal mean values from ACE-FTS at 57.5 °N. It is based on the method described in Jones et al. (2012) but with an updated data quality classification (Sheese et al., 2015). The climatology covers pressure levels from $1 \cdot 10^5$ to $1 \cdot 10^{-4}$ Pa, but lacks data for certain months and altitudes. A linear interpolation between months is used if values are missing. Above $1 \cdot 10^{-4}$ Pa the climatology is extrapolated using the vmr value from $1 \cdot 10^{-4}$ Pa. The temperature, altitude and pressure relationship is, above 100 Pa, taken from a climatology based on the MSISE-90 model (Hedin, 1991), while below 5000 Pa it is based on the database for used tropospheric correction (see 3.3). Between 5000 and 100 Pa the temperatures are obtained by a linear interpolation between the two datasets.

To solve Eq. 12, $\mathbf{S}_\epsilon$ and $\mathbf{S_a}$ must be specified. We describe these covariances with a standard deviation and a correlation function (see e.g. Christensen and Eriksson (2013)). For $\mathbf{S}_\epsilon$ the standard deviation is equal to the thermal noise estimated from the measurements (~ 0.07 K) and correlation between channels is modeled as a Gaussian correlation function with a correlation length equal to 1.6 channels. The specification of $\mathbf{S_a}$ depends on which state vector variable the elements describe. The covariance of CO is described with a standard deviation equal 100% of the apriori profile. This large uncertainty is needed to ensure a reasonable sensitivity despite the low signal to noise ratio of the CO measurements. For O_3 the standard deviation is described simply as 4 ppmv for all altitudes, and for temperature it is set to 5 K for all altitudes. The correlation between altitudes is set to follow a linear correlation function with a correlation length of 8 km for both species and the temperature. Tropospheric water vapor has a standard deviation equal to 10 % of the a priori value and a linear correlation function with a correlation length of 8 km, while the liquid water has a standard deviation equal to 100% of the a priori value, and no correlation between altitudes. The baseline fit has a standard deviation of 4 K for all coefficients.

3.3 Tropospheric correction

In order to accurately estimate the CO and O_3 concentrations in the mesosphere, the tropospheric attenuation needs to be accounted for. A common way of to achieve this is to model the troposphere as a single layer, with an effective temperature and opacity, and performing a correction of the observed spectra prior to performing the retrieval. For the DSB receiver the difference in the opacity

between the two sidebands is too large for such an approach to work, and as such the troposphere needs to be included directly into the forward model. This is done in two steps. First an atmosphere is selected from a database of tropospheric scenarios. The atmosphere selected is the one minimizing the following cost function

$$\chi^2 = \left(\mathbf{y^{trop}} - f(\mathbf{x^{trop}})\right)^T \mathbf{S}_\epsilon^{\mathbf{trop}} \left(\mathbf{y^{trop}} - f(\mathbf{x^{trop}})\right), \quad (13)$$

where $\mathbf{y^{trop}}$ is the measurements used for the tropospheric correction, $f(\mathbf{x^{trop}})$ the radiance from the modeled troposphere and $\mathbf{S}_\epsilon^{\mathbf{trop}}$ the covariance matrix describing the measurement noise for the measurements used for the tropospheric retrieval. For the DSB instrument $\mathbf{y^{trop}}$ consists of two elements, the mean $T_{\rm sky}$ measured across all channels, $T_{\rm sky}^{\rm mean}$, and the ground temperature at OSO at the time of the measurement, $T_{\rm ground}$, measured by the weather station at the site. Both values are averaged over the same time period as the spectral measurements. The second step is to expand $\mathbf{y}$ in Eq. 12 to include $\mathbf{y^{trop}}$ and retrieve $\mathbf{x^{trop}}$ with the OEM method, using the selected troposphere as the a priori. The effect of tropospheric attenuation on the mesospheric spectra are thus also added to $\mathbf{K}$.

The tropospheric states considered in Eq. 13 are taken from a database constructed of data from the ERA-Interim project (Dee et al., 2011), covering years 2009, 2010 and 2011. Data were extracted for the OSO site, at 00 and 12 UTH each day of the 3-year long period. In total, the database contains 2190 atmospheric states. Temperature and humidity data were used as provided by ERA-Interim. The liquid water content, LWC, however depends on the cloud cover, and the distribution of clouds within a resolved grid cell in ERA-interim. For the database used in this study, the liquid water content above OSO has been parameterized as a function of cloud fraction and mean liquid water content in an ERA-Interim grid box. The parametrization was corrected such that the fraction of cloudy to non-cloudy days, and the maximum integrated liquid water path is consistent with measurements from ASTRID and KONRAD. Using this database an apriori troposphere could be selected according to Eq. 13.

Fitting the troposphere using just $T_{\rm sky}^{\rm mean}$ and $T_{\rm ground}$ is a grossly under-determined problem, and thus to test the accuracy of this method the tropospheric attenuation was also simultaneously estimated by including measurements from the water vapor radiometer ASTRID into $\mathbf{y^{trop}}$ (averaged over the same timeperiod as the double sideband receiver). The two channels are simulated as described in Sec. 2.5 using the same settings as described in section 3.1. Simulations were also run for KONRAD, and comparing the simulated brightness temperatures from the two water vapor radiometers and brightness temperature measured, an offset was seen. For clear sky days (i.e. no clouds) ASTRID systematically measured brightness temperatures 3 and 5 K lower than the simulations predicted for the lower and upper frequency channels respectively, while KONRAD had a bias of -2 and +1 K for the two channels. Since both radiometers differ in their bias, we assume that this discrepancy comes from instrumental errors. For the study presented in this paper, the ASTRID instrument alone is used to characterize possible errors in the tropospheric correction described by Eq.

13 (see Sec 5). Thus, in order to ensure consistency between the simulations and the measurements, the ASTRID was bias corrected to match the simulated data before it is used.

4 Results of the OSO measurements

Figure 7 shows retrieved profiles from two example cases, one captured during a winter night and one during a autumn day. The winter spectrum shows stronger emission and less noise than the summer spectrum. The different noise levels mainly come from the higher tropospheric humidity in the autumn leading to more attenuation of the mesospheric signal. Figure 8 shows all retrieved CO and $\mathrm{O_3}$ from the measurement period. From the retrieved profiles, it is clear that stronger emission in the winter come from an increase in CO and $\mathrm{O_3}$ at altitudes above $10\,\mathrm{Pa}$. The general structure of the CO distribution is seen in Figure 8 with a sharp increase in volume mixing in the upper mesosphere.

This initial time series mainly covers the winter period. During the winter the general circulation brings down air from the thermosphere into the mesosphere which increases the mesospheric CO abundance. This down-welling is strongest inside the polar vortex, and the variation of CO seen from day to day is mainly explained by movement of the polar vortex. OSO is sometimes located within and sometimes outside the vortex during the winter. During summer the general circulation is reversed and the abundancy of CO in the mesosphere is reduced as air from the tropics and mid-latidues are transported polewards in the lower mesosphere. This decrease in mesospheric CO can be seen at the end of our time-series.

The time series of $\mathrm{O_3}$ both show the upper part of the stratospheric peak and a nighttime peak at altitudes above $10\,\mathrm{Pa}$ during the winter. Due to the poor resolution of the instrument the observed mesospheric diurnal peak can be a mixture of both "the secondary ozone peak" at $\sim 90\,\mathrm{km}$ and "the tertiary ozone peak", located at $72\mathrm{km}$, see Section 1.

Example averaging kernels are shown in Fig. 9. For CO, the averaging kernels are shown with respect to a change in the atmosphere relative to the apriori profile, while for ozone the averaging kernels are shown with respect vmr changes in the atmosphere. The reason for using different units for the two species is that for CO large changes in terms of volume mixing ratio are more probable at high altitude than at lower. This strong vertical gradient of the CO concentration across the altitude range covered by the instrument must be accounted for in the retrieval procedure, and hence $\mathbf{S_a}$ is specified relative to the apriori. This in turn results in averaging kernels optimized with respect to such relative changes, and these averaging kernels are thus most descriptive of how the retrieved atmosphere changes with changes in the real atmosphere. The variability of $\mathrm{O_3}$ around the apriori can be better represented with a constant vmr value, and hence AVKs with respect to this is shown.

The retrievals have a measurement response above 0.8 between 20 and 0.3 Pa for CO and 200 to 0.8 Pa for $\mathrm{O_3}$. Calculating the degrees of freedom of the retrievals (trace of averaging kernel matrix) CO is retrieved with 1-2 degrees of freedom (depending on season) and $\mathrm{O_3}$ with 3-4.5 degrees of

freedom. Resulting to an average vertical resolution of 20 and 10 km for CO and $\mathrm{O_3}$ respectively. For altitudes above 70 km both lines are dominated by doppler broadening, and thus retrieved values above this level may contain information from changes in the true atmosphere anywhere within this region. This is reflected by the fact that the averaging kernel for 2.4 Pa and 1 Pa remains non-zero at the top of figure 9.

5 Sensitivity to errors in forward model and retrieval parameters

Errors are introduced from uncertainties in the forward model and the retrieval parameters. These include uncertainties in the modeling of the instrument, uncertainties in the spectroscopic parameters used, uncertainties in the tropospheric correction as well as a dependence on the a priori assumptions used in the retrievals. These errors introduce a bias in the mean atmospheric state retrieved, which we will describe as an systematic error. Additionally they add variability to the data which we will describe as a random error source, implying that it affects the scatter of the data set rather than the total mean.

To estimate these errors the retrievals are rerun with each parameter perturbed with its 1-σ uncertainty. For the tropospheric correction the error was estimated by comparing the nominal correction method (using only $T_{\mathrm{sky}}^{\mathrm{mean}}$ and T_{ground}) to the extended tropospheric correction including ASTRID. The error estimation was carried out over the sub-set of measurements where simultaneous data from the OSO instrument and ASTRID was available (172 in total). For the spectroscopic parameters the uncertainty was estimated using either the difference between HITRAN 2012 and the value used in our retrieval, or the 1-σ uncertainty reported in HITRAN 2001. The option leading to the greatest difference in the retrieved values was selected as a worst-case scenario. A summary of the values used is given Table 5.

The mean difference (systematic errors) and the standard deviation (random errors) between each of the perturbed retrievals and the standard retrievals are shown in Fig. 10, together with the total root-sum-square error from all the parameters. For CO, the estimated systematic errors are around 0.2 ppmv for altitudes around 20 Pa, while degrading at altitudes above this, to 2.7 ppmv at 1 Pa. The largest source of systematic uncertainty is the characterization of the sideband response, followed by uncertainties in apriori profile . The total estimated random errors for CO from the retrieval parameters are of the same size as the random error from thermal noise in the measurements ($\sim$0.2 ppmv at 20 Pa and $\sim$3 ppmv at 1 Pa). For $\mathrm{O_3}$, the estimated systematic and random errors from the simulated error sources, are less than 0.5 ppmv between 50 and 1 Pa, with the largest source of systematic errors being uncertainties in the pressure broadening coefficient at low altitudes and the sideband response at high altitudes. Errors due to thermal noise in the measurements are better than 0.5 ppmv across all altitudes where the measurement response is greater than 0.8. A summary estimated random and systematic errors for the retrieved data at example pressure levels is given

in Table 6. For the estimate of the random errors, the maximum error from either thermal noise or forward model parameters is used.

6 Satellite comparisons

The vertical profiles from the OSO instruments have been compared to version V-3-3 of CO and O_3 data from the microwave limb sounder MLS on the Aura satellite (Pumphrey et al., 2007) and (Froidevaux et al., 2008), see Table 7. The comparison covers the time period October 2014 until April 2015. MLS data taken closer to the OSO-site than latitude $\pm 5^\circ$ and longitude $\pm 10^\circ$ has been used, see Figure 11. MLS has measurements solely from either night (UTC 1–2) or day (UTC 11–12) within the used position range. Since the OSO data is 6–h averages the 6–h period with the best overlap with the MLS measurement times has been used in the comparison. The MLS data was interpolated onto the OSO retrieval grid. To compensate for the different vertical resolution of the two instruments the MLS data was convolved with the averaging kernels, A, of the OSO instrument (Rodgers and Connor, 2003)

$$\mathbf{x}_\mathrm{s} = \mathbf{x}_\mathrm{a} + \mathbf{A}(\mathbf{x}_\mathrm{sat} - \mathbf{x}_\mathrm{a}), \tag{14}$$

where $\mathbf{x}_\mathrm{a}$ is the OSO a priori profile and $\mathbf{x}_\mathrm{s}$ is the smoothed MLS profile.

Figures 12 and 14 show mean profiles of O_3 and CO for the two instruments. Figure 12 shows averaged night and day O_3 profiles from December 2014 and Figure 13 shows the difference in vmr between OSO and MLS. The averaged day profiles from the two instrument are very similar within their measurement ranges. The night profiles however differ at altitudes above 5 Pa (~ 70 km), where OSO shows a more pronounced peak in the upper mesosphere. The MLS peak seen in the night profile at 2 Pa is probably "The tertiary ozone peak".

There is no clear diurnal variation of the CO profiles. Figure 14 shows averaged day profiles from December 2014 and March 2015 and Figure 15 shows the difference in vmr between OSO and MLS. OSO shows higher CO abundances than MLS at altitudes above 5 Pa during December. During March the difference between the two instruments is much less pronounced.

Figures 16 and 17 show time series for the measurement period for OSO and MLS at three different pressure levels (100, 18, and 2.4 Pa) for O_3 and at two different pressure levels (18 and 1 Pa) for CO. The average measurement response for OSO is higher than 80 % for both O_3 and CO at these pressure levels and MLS reports valid mesospheric data at altitudes with pressures $\geq$2 Pa for O_3 and $\geq$1 Pa for CO. Note that due to the vertical resolution of the OSO instrument, the values at these pressure levels are not necessarily completely independent. The CO and O_3 data from the two instruments shows the same general features, both in terms of the overall variation and in sporadic events. The main differences between the two instruments are both the higher OSO values of upper mesospheric O_3 mixing ratios during winter nights and the higher OSO values of upper mesospheric CO mixing ratios during the winter compared to MLS (see also Figures 12 and 14).

MLS data are often used for comparison with ground-based instruments. Boyd et al. (2007) (latitude $< 40°$) and Palm et al. (2010) (high latitudes) found good agreement between ground-based datasets of mesospheric daytime volume mixing ratios of O_3 compared to MLS. The nighttime values of Boyd et al. (2007) were also close to MLS, however Palm et al. (2010) obtained higher O_3 mixing ratios above ≈ 70 km during winter nights. The "tertiary ozone peak" above ≈ 70 km is only present in winter nights at high latitudes (Marsh et al., 2001) and can hence not be seen in the Boyd et al. (2007) dataset. The altitude of the "tertiary ozone peak" is close to the upper limit of MLS O_3 data which can explain the low bias of MLS winter nighttime O_3 above ≈ 70 km compared to the data presented in this report and to the dataset of Palm et al. (2010).

Similar discrepancies between mesospheric CO measurements from MLS and ground-based instruments, as presented above, have been reported earlier by Forkman et al. (2012) using an older receiver system and by Hoffmann et al. (2011).

7 Summary and conclusions

The first simultaneous measurements of mesospheric O_3 at 110.8 GHz and CO at 115.3 GHz made by a ground-based, double sideband and frequency-switched radiometer system operated at the Onsala Space Observatory, OSO, (57.4° N, 11.9° E) are presented.

Dicke-switching is the generally used observation method in microwave radiometry to diminish effects of gain variations in the receiver system. Frequency-switching is the most time effective Dicke-switching variant since no reference load is observed except in the calibrations. Since the frequency throw has to be less than ~ 20 MHz to avoid gain differences, the method is restricted for studies of the spectral shapes of emission lines from high altitudes where the pressure broadening is limited. The method is hence well-adapted for observations of mesospheric CO and O_3.

Most ground-based microwave heterodyne radiometers for atmospheric remote sensing are operated in single sideband mode. In a double sideband system simultaneous measurements of two emission lines at rather different frequencies, as O_3 at 110.84 GHz and CO at 115.27 GHz, are possible. The drawbacks of a system were both sidebands are used are both that the sideband ratio has to be measured and that the tropospheric attenuation can differ between the two line frequencies.

In this study the gain between the frontend RF input and IF output was estimated by measuring the IF power when a calibrated RF source was connected to the frontend. The RF source was swept across the lower and upper sidebands and the sideband ratio was estimated by comparing the IF and RF powers in the measured frequency range. Standing waves arising from reflections in the transmission line affects the result. In order to reduce the reported error in the sideband ratio estimation, the measurement setup will be refined to try diminish the standing waves.

The commonly used method to compensate measured spectra for the tropospheric attenuation is to use an one-layer model of the troposphere with constant effective temperature and opacity and to

correct the observed spectra before the retrieval process. The difference between the opacities in the two sidebands is however too large for this method to work. An approach where the troposphere is included in the forward model has been used.

To calculate vertical profiles of CO and O_3 from the measured spectra the Optimal Estimation Method, OEM, has been used in the retrieval process. To present as exact error estimations as possible, the systematic effects arising from the uncertainties in the different measurement and retrieval parameters, have been carefully studied.

The OSO CO and O_3 data have been compared to measurements from the satellite instrument MLS (v3-3) on Aura. The data from two instruments shows the same general features in both sporadic events and in the overall variation. The main differences between the instruments are the higher OSO values of O_3 mixing ratios in the upper mesosphere during the winter nights and the higher OSO winter values of CO mixing ratios in the upper mesosphere compared to MLS.

Microwave radiometry is the only ground-based remote sensing technique that can monitor the mesosphere day and night even during cloudy conditions. Simple and reliable microwave radiometers measuring in the frequency range below 150 GHz can be very valuable for mesospheric research since they can be operated at almost every ground-based site. The described instrument shows the potential of a double-sideband and frequency-switched radiometer system for simultaneous measurements of mesospheric CO and O_3.

Acknowledgements. The Swedish Natural Science Research Council supported the maintenance and development of the OSO receiver system. We thank the teams behind HITRAN and JPL for providing spectroscopic data to the retrievals. We thank the community behind ARTS for software used in the retrieval process and ECMWF for meteorological data and Kaley Walker and Ja-Ho Koo for providing the climatology for CO and O_3 from the Atmospheric Chemistry Experiment (ACE). ACE, also known as SCISAT, is a Canadian-led mission mainly supported by the Canadian Space Agency and the Natural Sciences and Engineering Research Council of Canada. Finally we thank Rüdiger Haas for downloading and preparing of ERA-Interim data and the laboratory and workshop of Onsala Space Observatory for keeping the OSO receiver up and running.

References

Aellig, C., Kaempfer, N., and Hauchecorne, A.: Variability of mesospheric CO in the fall and winter as observed with ground-based microwave radiometry at 115 GHz, J. Geophys. Res., 100, 14 125–14, doi:10.1029/95JD00984, 1995.

Boyd, I. S., Parrish, A. D., Froidevaux, L., Von Clarmann, T., Kyrölä, E., Russell, J. M., and Zawodny, J. M.: Ground-based microwave ozone radiometer measurements compared with Aura-MLS v2. 2 and other instruments at two Network for Detection of Atmospheric Composition Change sites, J. Geophys. Res., 112, doi:10.1029/2007JD008720, 2007.

Brasseur, G. and Solomon, S.: Aeronomy of the Middle Atmosphere, Springer-Verlag, Berlin, 2008.

Buehler, S. A., Eriksson, P., Kuhn, T., von Engeln, A., and Verdes, C.: ARTS, the Atmospheric Radiative Transfer Simulator, J. Quant. Spectrosc. Radiat. Transfer, 91, 65–93, doi:10.1016/j.jqsrt.2004.05.051, 2005.

Caton, W. M., Mannella, G. G., Kalaghan, P. M., Barrington, A. E., and Ewen, H. I.: Radio Measurement of the Atmospheric Ozone Transition at 101.7 GHz, Astrophys. J., 151, L153, doi:10.1086/180163, 1968.

Chapman, S.: A theory of upper-atmospheric ozone, Edward Stanford, 1930.

Christensen, O. M. and Eriksson, P.: Time series inversion of spectra from ground-based radiometers, Atmos. Meas. Tech., 6, 1597–1609, doi:10.5194/amt-6-1597-2013, 2013.

Connor, B. J. and Radford, H.: Pressure broadening of millimeter-wave ozone lines by atmospheric gases, J. Mol. Spectrosc., 117, 15–29, doi:10.1016/0022-2852(86)90088-3, 1986.

Connor, B. J., Siskind, D. E., Tsou, J. J., Parrish, A., and Remsberg, E. E.: Ground-based microwave observations of ozone in the upper stratosphere and mesosphere, J. Geophys. Res., 99, 16 757–16 770, doi:10.1029/94JD01153, 1994.

de Zafra, R. L. and Muscari, G.: CO as an important high-altitude tracer of dynamics in the polar stratosphere and mesosphere, J. Geophys. Res, 109, doi:10.1002/qj.828, 2004.

Dee, D., Uppala, S., Simmons, A., Berrisford, P., Poli, P., Kobayashi, S., Andrae, U., Balmaseda, M., Balsamo, G., Bauer, P., et al.: The ERA-Interim reanalysis: Configuration and performance of the data assimilation system, Q. J. R. Meteorolog. Soc., 137, 553–597, doi:10.1002/qj.828, 2011.

Elgered, G. and Jarlemark, P. O. J.: Ground-based microwave radiometry and long-term observations of atmospheric water vapor, Radio Sci., 33, 707–717, doi:10.1029/98RS00488, 1998.

Emrich, A., Andersson, S., Wannerbratt, M., Sobis, P., Cherednichenko, S., Runesson, D., Ekebrand, T., Krus, M., Tegnader, C., and Krus, U.: Water Vapor Radiometer for ALMA, in: Twentieth International Symposium on Space Terahertz Technology, vol. 1, pp. 174–177, www.nrao.edu/meetings/isstt/papers/2009/2009174177.pdf, 2009.

Eriksson, P. and Merino, F.: On simulating passive observations of the middle atmosphere in the range 1-1000 GHz, Tech. rep., Chalmers University of Technology, Göteborg, Sweden, 1997.

Eriksson, P., Jiménez, C., and Buehler, S. A.: Qpack, a tool for instrument simulation and retrieval work, J. Quant. Spectrosc. Radiat. Transfer, 91, 47–64, doi:10.1016/j.jqsrt.2004.05.050, 2005.

Eriksson, P., Buehler, S. A., Davis, C. P., Emde, C., and Lemke, O.: ARTS, the atmospheric radiative transfer simulator, Version 2, J. Quant. Spectrosc. Radiat. Transfer, 112, 1551–1558, doi:10.1016/j.jqsrt.2011.03.001, 2011.

Fernandez, S., Murk, A., and Kämpfer, N.: GROMOS-C, a novel ground-based microwave radiometer for ozone measurement campaigns, Atmos. Meas. Tech., 8, 2649–2662, doi:10.5194/amt-8-2649-2015, 2015.

Forkman, P., Eriksson, P., Winnberg, A., Garcia, R., and Kinnison, D.: Longest continuous ground-based measurements of mesospheric CO, Geophys. Res. Lett., 30, 1532, doi:10.1029/2003GL016931, 2003.

Forkman, P., Christensen, O. M., Eriksson, P., Urban, J., and Funke, B.: Six years of mesospheric CO estimated from ground-based frequency-switched microwave radiometry at 57° N compared with satellite instruments, Atmos. Meas. Tech., 5, 2827–2841, doi:10.5194/amt-5-2827-2012, 2012.

Froidevaux, L., Jiang, Y. B., Lambert, A., Livesey, N. J., Read, W. G., Waters, J. W., Browell, E. V., Hair, J. W., Avery, M. A., McGee, T. J., Twigg, L. W., Sumnicht, G. K., Jucks, K. W., Margitan, J. J., Sen, B., Stachnik, R. A., Toon, G. C., Bernath, P. F., Boone, C. D., Walker, K. A., Filipiak, M. J., Harwood, R. S., Fuller, R. A., Manney, G. L., Schwartz, M. J., Daffer, W. H., Drouin, B. J., Cofield, R. E., Cuddy, D. T., Jarnot, R. F., Knosp, B. W., Perun, V. S., Snyder, W. V., Stek, P. C., Thurstans, R. P., and Wagner, P. A.: Validation of Aura Microwave Limb Sounder stratospheric ozone measurements, J. Geophys. Res., 113, doi:10.1029/2007JD008771, 2008.

Hartogh, P., Hartmann, G., and Zimmerman, P.: Simultaneous Water Vapour And Ozone Measurements with Millimeterwaves In The Stratosphere And Mesosphere, in: Geoscience and Remote Sensing Symposium, 1991. IGARSS '91. Remote Sensing: Global Monitoring for Earth Management., International, vol. I, pp. 227–230, doi:10.1109/IGARSS.1991.577719, 1991.

Hartogh, P., Jarchow, C., Sonnemann, G. R., and Grygalashvyly, M.: Ozone distribution in the middle latitude mesosphere as derived from microwave measurements at Lindau (51.66°N, 10.13°E), J. Geophys. Res., 116, doi:10.1029/2010JD014393, 2011.

Hays, P. and Roble, R. G.: Observation of mesospheric ozone at low latitudes, Planet. Space Sci., 21, 273–279, doi:10.1016/0032-0633(73)90011-1, 1973.

Hedin, A. E.: Extension of the MSIS thermosphere model into the middle and lower atmosphere, J. Geophys. Res., 96, 1159–1172, doi:10.1029/90JA02125, 1991.

Hocke, K., Kämpfer, N., Ruffieux, D., Froidevaux, L., Parrish, A., Boyd, I., von Clarmann, T., Steck, T., Timofeyev, Y. M., Polyakov, A. V., and Kyrölä, E.: Comparison and synergy of stratospheric ozone measurements by satellite limb sounders and the ground-based microwave radiometer SOMORA, Atmos. Chem. Phys., 7, 4117–4131, doi:10.5194/acp-7-4117-2007, 2007.

Hoffmann, C. G.: Application of CO as a tracer for dynamics in the polar winter middle atmosphere - A study based on ground-based microwave observations in Kiruna, Ph.D. thesis, Universität Bremen, http://elib.suub.uni-bremen.de/edocs/00102610-1.pdf, 2012.

Hoffmann, C. G., Raffalski, U., Palm, M., Funke, B., Golchert, S. H. W., Hochschild, G., and Notholt, J.: Observation of strato-mesospheric CO above Kiruna with ground-based microwave radiometry - retrieval and satellite comparison, Atmos. Meas. Tech., 4, 2389–2408, doi:10.5194/amt-4-2389-2011, 2011.

Janssen, M. A.: Atmospheric Remote Sensing by Microwave Radiometry, John Wiley, New York, 1993.

Jones, A., Walker, K. A., Jin, J. J., Taylor, J. R., Boone, C. D., Bernath, P. F., Brohede, S., Manney, G. L., McLeod, S., Hughes, R., and Daffer, W. H.: Technical Note: A trace gas climatology derived from the Atmospheric Chemistry Experiment Fourier Transform Spectrometer (ACE-FTS) data set, Atmospheric Chemistry and Physics, 12, 5207–5220, doi:10.5194/acp-12-5207-2012, 2012.

Kunzi, K. F. and Carlson, E. R.: Atmospheric CO volume mixing ratio profiles determined from ground-based measurements of the J = 1 $\rightarrow$ O and J = 2 $\rightarrow$ 1 emission lines, J. Geophys. Res., 87, 7235–7241, doi:10.1029/JC087iC09p07235, 1982.

Liebe, H. J., Hufford, G. A., and Cotton, M. G.: Propagation modeling of moist air and suspended water/ice particles at frequencies below 1000 GHz., in: AGARD 52nd Specialists Meeting of the Electromagnetic Wave Propagation Panel, Palma de Mallorca, Spain, 1993.

Lobsiger, E.: Ground-based microwave radiometry to determine stratospheric and mesospheric ozone profiles, J. Atmos. Terr. Phys., 49, 493 – 501, doi:10.1016/0021-9169(87)90043-2, 1987.

Lopez-Puertas, M., Lopez-Valverde, M., Garcia, R., and Roble, R.: A review of CO_2 and CO abundances in the middle atmosphere, Geophysical monograph, 123, 83–100, doi:10.1029/GM123p0083, 2000.

Marsh, D., Smith, A., Brasseur, G., Kaufmann, M., and Grossmann, K.: The existence of a tertiary ozone maximum in the high-latitude middle mesosphere, Geophys. Res. Lett., 28, 4531–4534, doi:10.1029/2001GL013791, 2001.

Moreira, L., Hocke, K., Eckert, E., von Clarmann, T., and Kämpfer, N.: Trend analysis of the 20-year time series of stratospheric ozone profiles observed by the GROMOS microwave radiometer at Bern, Atmos. Chem. Phys., 15, 10 999–11 009, doi:10.5194/acp-15-10999-2015, 2015.

Nagahama, T., Nakane, H., Fujinuma, Y., Ninomiya, M., Ogawa, H., and Fukui, Y.: Ground-based millimeter-wave observations of ozone in the upper stratosphere and mesosphere over Tsukuba, Earth Planets Space, 51, 1287–1296, doi:10.1186/BF03351602, 1999.

Nedoluha, G. E., Boyd, I. S., Parrish, A., Gomez, R. M., Allen, D. R., Froidevaux, L., Connor, B. J., and Querel, R. R.: Unusual stratospheric ozone anomalies observed in 22 years of measurements from Lauder, New Zealand, Atmos. Chem. Phys., 15, 6817–6826, doi:10.5194/acp-15-6817-2015, 2015.

Palm, M., Hoffmann, C. G., Golchert, S. H. W., and Notholt, J.: The ground-based MW radiometer OZORAM on Spitsbergen â€“ description and status of stratospheric and mesospheric O_3-measurements, Atmos. Meas. Tech., 3, 1533–1545, doi:10.5194/amt-3-1533-2010, 2010.

Parrish, A.: Millimeter-wave remote sensing of ozone and trace constituents in the stratosphere, Proceedings of the IEEE, 82, 1915–1929, doi:10.1109/5.338079, 1994.

Parrish, A., deZafra, R. L., Solomon, P. M., and Barrett, J. W.: A ground-based technique for millimeter wave spectroscopic observations of stratospheric trace constituents, Radio Sci., 23, 106–118, doi:10.1029/RS023i002p00106, 1988.

Parrish, A., Connor, B. J., Tsou, J. J., McDermid, I. S., and Chu, W. P.: Ground-based microwave monitoring of stratospheric ozone, J. Geophys. Res, 97, 2541–2546, doi:10.1029/91JD02914, 1992.

Peter, R., Caliseri, Y., and Kämpfer, N.: Variability of middle atmospheric ozone abundances derived from continuous ground-based millimeter wave measurements, in: Proceedings of the XVIII Quadrennial Ozone Symposium, pp. 559–562, 1998.

Pickett, H., Poynter, R., Cohen, E., Delitsky, M., Pearson, J., and Müller, H.: Submillimeter, millimeter, and microwave spectral line catalog, J. Quant. Spectrosc. Radiat. Transfer, 60, 883–890, doi:10.1016/S0022-4073(98)00091-0, 1998.

Piddyachiy, V., Shulga, V., Myshenko, V., Korolev, A., Myshenko, A., Antyufeyev, A., Poladich, A., and Shkodin, V.: 3-mm wave spectroradiometer for studies of atmospheric trace gases, Radiophys. Quantum Electron., 53, 326–333, doi:10.1007/s11141-010-9231-y, 2010.

Pumphrey, H. C., Filipiak, M., Livesey, N., Schwartz, M., Boone, C., Walker, K., Bernath, P., Ricaud, P., Barret, B., Clerbaux, C., Jarnot, R., Manney, G., and Waters, J.: Validation of middle-atmosphere carbon monoxide retrievals from MLS on Aura, J. Geophys. Res., 112, D24S38, doi:10.1029/2007JD008723, 2007.

Rodgers, C.: Inverse methods for atmospheric sounding: Theory and practice, World Scientific, Singapore, 2000.

Rodgers, C. D. and Connor, B.: Intercomparison of remote sounding instruments, J. Geophys. Res, 108, 4116, doi:10.1029/2002JD002299, 2003.

Rosenkranz, P. W.: Absorption of microwaves by atmospheric gases, in: Atmospheric remote sensing by microwave radiometry, edited by Janssen, M. A., pp. 37–90, John Wiley & Sons, Inc., 1993.

Rosenkranz, P. W.: Water Vapor Microwave Continuum Absorption: A Comparison of Measurements and Models, Radio Sci., 33, 919–928, doi:10.1029/98RS01182, (correction in 34, 1025, 1999), 1998.

Rothman, L., Barbe, A., Chris Benner, D., Brown, L., Camy-Peyret, C., Carleer, M., Chance, K., Clerbaux, C., Dana, V., Devi, V., et al.: The HITRAN molecular spectroscopic database: edition of 2000 including updates through 2001, J. Quant. Spectrosc. Radiat. Transfer, 82, 5–44, doi:10.1016/S0022-4073(03)00146-8, 2003.

Sheese, P. E., Boone, C. D., and Walker, K. A.: Detecting physically unrealistic outliers in ACE-FTS atmospheric measurements, Atmospheric Measurement Techniques, 8, 741–750, doi:10.5194/amt-8-741-2015, 2015.

Stoew, B., Rieck, C., and Elgered, G.: First results from a new dual-channel water vapor radiometer, in: Proc. of the 14th Working Meeting on European VLBI for Geodesy and Astrometry, P. Tomasi, F. Mantovani and M.-A. Perez-Torres (eds.), pp. 79–82, http://www.evga.org/files/2000EVGA-proc_SanPietro.pdf, 2000.

Straub, C., Espy, P. J., Hibbins, R. E., and Newnham, D. A.: Mesospheric CO above Troll station, Antarctica observed by a ground based microwave radiometer, Earth Syst. Sci. Data, 5, 199–208, doi:10.5194/essd-5-199-2013, 2013.

Ulich, B. L. and Haas, R. W.: Absolute calibration of millimeter-wavelength spectral lines, Astrophys. J. Suppl. Ser., 30, 247–258, doi:10.1086/190361, 1976.

Vassilev, V., Wadefalk, N., Kozhuharov, R., Abbasi, M., Gunnarsson, S. E., Zirath, H., Pellikka, T., Emrich, A., Pantaleev, M., Kallfass, I., et al.: MMIC-Based Components for MM-Wave Instrumentation, Microwave and Wireless Components Letters, IEEE, 20, 578–580, doi:10.1109/LMWC.2010.2065797, 2010.

Waters, J., Wilson, W., and Shimabukuro, F.: Microwave measurement of mesospheric carbon monoxide, Science, 191, 1174, doi:10.1126/science.191.4232.1174, 1976.

Table 1: Receiver specifications

Radio frequency	110–116 GHz, DSB
Mirror edge taper	-35 dB
Elevation	80°, fixed
Horn	Aluminium, corrugated
Beam width, FWHM	6°
First stage	LNA +20 dB, Ambient temperature
Image sideband rejection	None, DSB
Sideband response	0.50 / 0.50 $\pm$ 0.05
Local oscillator (LO)	Synth. + multipliers
LO frequency	113 GHz
Frequency throw ($2\Delta f$)	8 MHz
Mixer IF	2.21 GHz
DSB receiver temperature	$\sim$450 K
Backend spectrometer	800 channel autocorrelator
Bandwidth	20 MHz
Nominal resolution	25 kHz
Integration time	6 h centered at UTC 05, 11, 17, and 23

Table 2: Specifications for the total power dual channel radiometers

Radiometer	ASTRID	KONRAD	Unit
Radio frequencies	21.0 / 31.4	20.6 / 31.6	[GHz]
Antenna (one for each frequency)	Dielectrically loaded horn	Conical lens horns	
Beam width, FWHM	6 / 6	2.9 / 2.0	[°]
Pointing resolution	0.1	0.1	[°]
Reference load temperatures	313 / 360	313 / 373	[K]
System noise temperature	450 / 550	450 / 550	[K]
RF bandwidth (both channels)	1000	320	[MHz]
Accuracy	< 1	0.5	[K]

Table 3: Summary of the complete absorption models. The model name refers to the name used internally in ARTS, while the model is described in the reference given.

Species	Absorption model	Reference
N_2	N2-SelfContStandardType	Rosenkranz (1993)
O_2	O2-PWR98	Rosenkranz (1998)
H_2O	H2O-PWR98	Rosenkranz (1998)
LiquidWater	liquidcloud-MPM93	Liebe et al. (1993)

Table 4: Summary of the two major spectroscopic lines.

Line parameter	CO	O_3	Unit
Center frequency, f_0	115.2712018	110.8359230	$[\mathrm{GHz}]$
Line intensity, I_0	$9.761128 \cdot 10^{-18}$	$3.567796 \cdot 10^{-17}$	$[\mathrm{m^2\,Hz^{-1}}]$
Ref. temp. for Line intensity	300	300	$[\mathrm{K}]$
Air broadened width	23332.68	23932.87	$[\mathrm{Hz\,Pa^{-1}}]$
Self broadened width	25958.54	30009.87	$[\mathrm{Hz\,Pa^{-1}}]$
Ref. temp. for broad. param.	296	296	$[\mathrm{K}]$
Temp. dep. exp. for broad. param.	0.69	0.73	$[-]$

Table 5: Summary of the perturbations applied to the forward model and retrieval parameters in the sensitivity study. Method indicates how the perturbation values were estimated.

Parameter	Perturbation (1σ)	Method
Line strength (O_3 / CO)	$\sim$2%	Comparison to HITRAN 2012
Pressure broadening parameter (O_3 / CO)	10%	Uncertainty given in HITRAN 2001
A priori profile	50%	-
A priori uncertainty	50%	-
Temperature profile	$\pm$5 K	1σ of MSISE-90 is 3 K
Sideband response	5%	Sec. 2.4
Tropospheric correction	Comparison to method using ASTRID	-

Table 6: Summary of error estimates.

Species	Pressure (Pa)	Systematic error (ppmv)	Random error (ppmv)
O_3	100	1.01	0.39
O_3	18	0.22	0.44
O_3	2.4	0.27	0.34
CO	18	0.18	0.19
CO	1	2.76	1.66

Table 7: Satellite characteristics.

Satellite instrument	Aura-MLS
Launch	15 July 2004
Orbit inclination	90°
Measurement principle	Limb sounding, emission
Frequency band	240 GHz
CO and O_3 versions	V-3-3
CO validation	Pumphrey et al. (2007)
O_3 validation	Froidevaux et al. (2008)
Vertical range	10–75 (85) km for O_3 (CO)
Vertical resolution (mesosphere)	7–8 km
Horizontal resolution (mesosphere)	200 km
Systematic errors (above 60 km)	$\sim \pm 20$ %
Co-location range satellite-OSO	Lat. $\pm 5°$ & Long. $\pm 10°$
Co-located measurement days	140

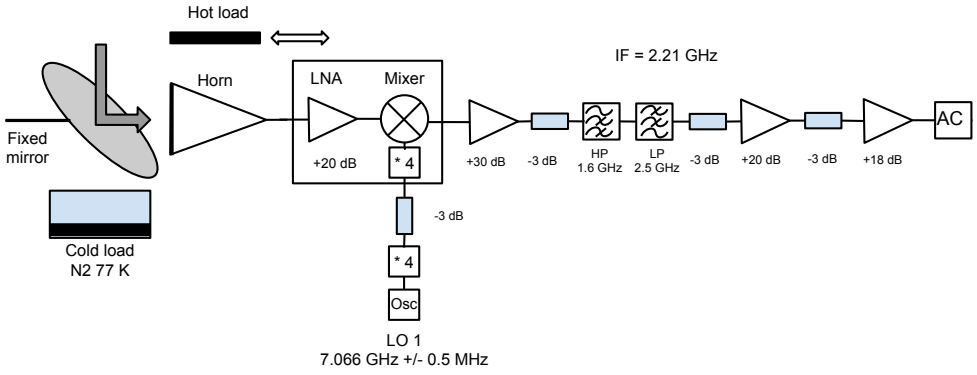

Figure 1: Block diagram of the DSB 110-115 GHz O_3/ CO receiver system. The cold load is regularly mounted and used.

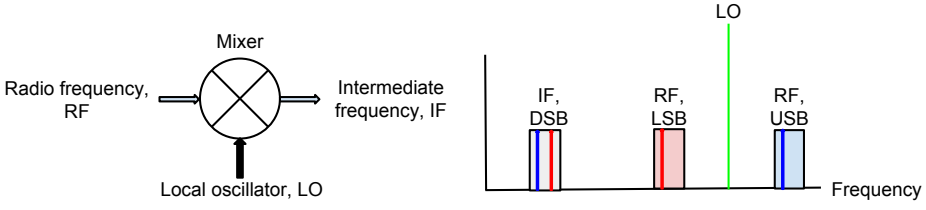

Figure 2: Mixer fundamentals.

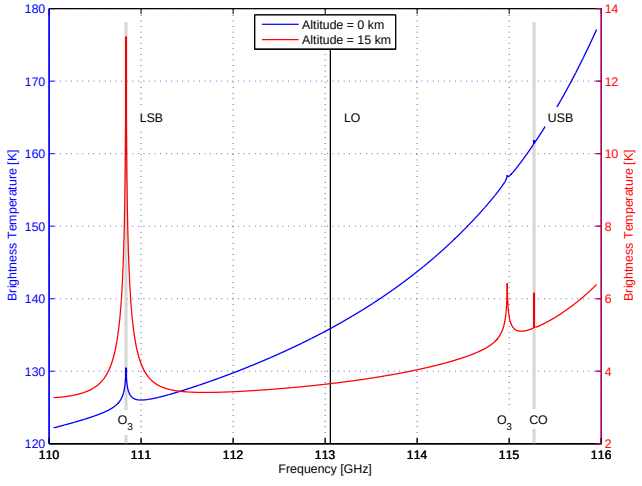

Figure 3: Simulated atmospheric spectra as seen with an elevation of 80° from the ground (blue) and, for clarity, from an altitude of 15 km (red). The 20 MHz wide LSB and USB frequency ranges and the LO frequency are marked.

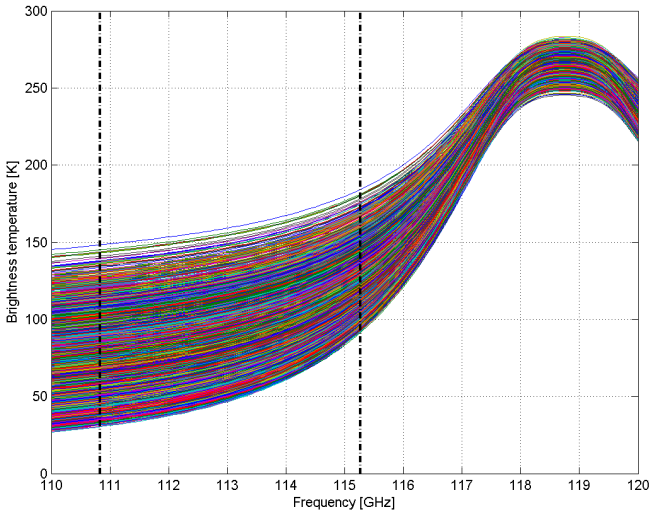

Figure 4: Simulated atmospheric spectra from one year of radiosonde data taken at the Landvetter airport 38 km NE of the Onsala site. Different tropospheric conditions explain the seen variation.

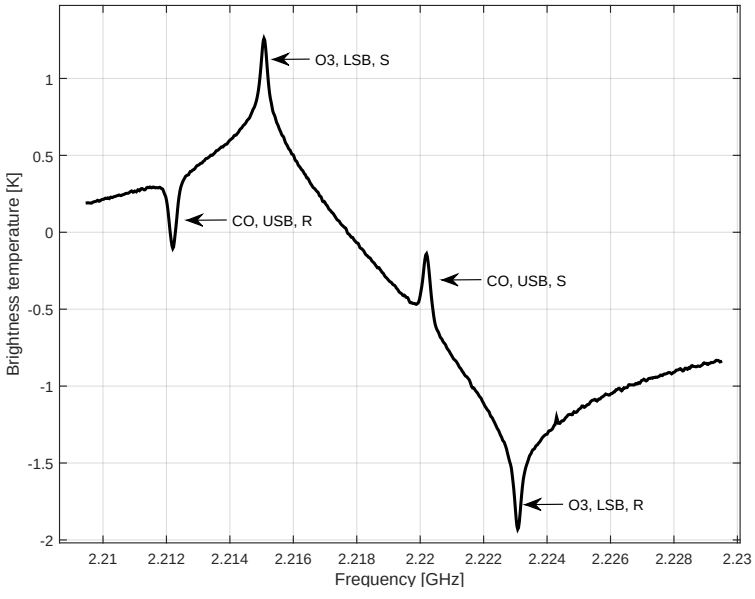

Figure 5: Average frequency-switched spectrum from December 2014 of $\mathrm{O_3}$ from the lower sideband, LSB, and CO from the upper sideband, USB. S and R are the frequency-switching signal and reference phases. The wide wings of the $\mathrm{O_3}$-line explain the general baseline shape.

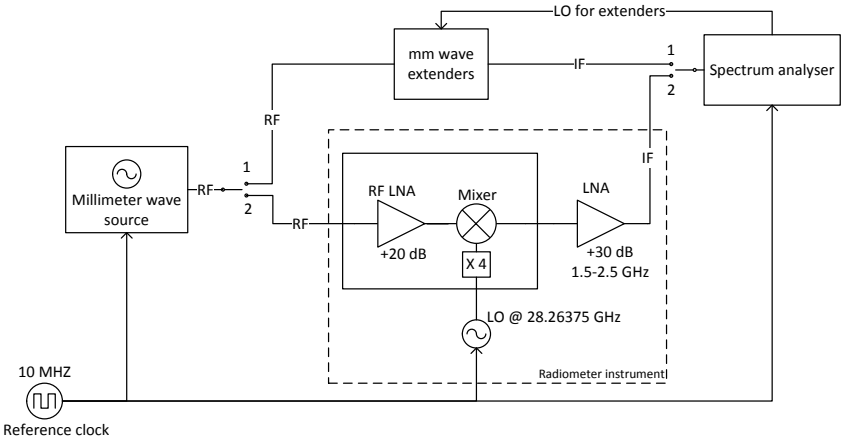

Figure 6: Setup for sideband ratio measurement.

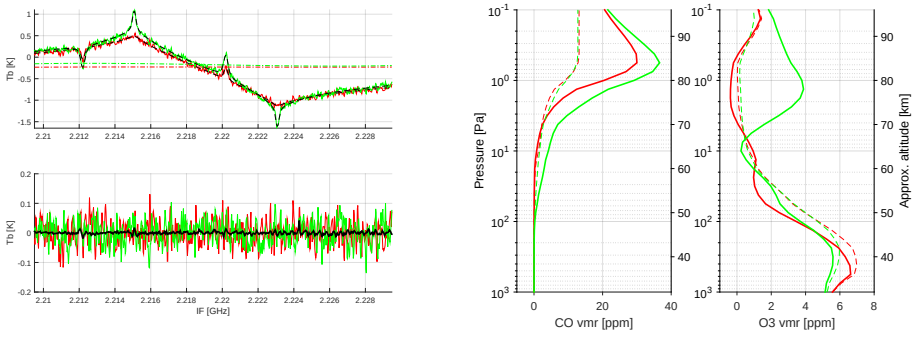

Figure 7: The top left panel shows measured spectra (solid lines) and fitted spectra (black-dashed lines) at two different times. The green line corresponds to a mid-winter night, while the red is an autumn day. The near horizontal dashed-dotted lines are the fitted baselines for the two spectra. The lower left panel shows the residuals from the fitting of the two spectra together with the mean residual of all spectra (black line). The two right panels show the retrieved profiles for the corresponding cases, together with the a priori profile used (dashed).

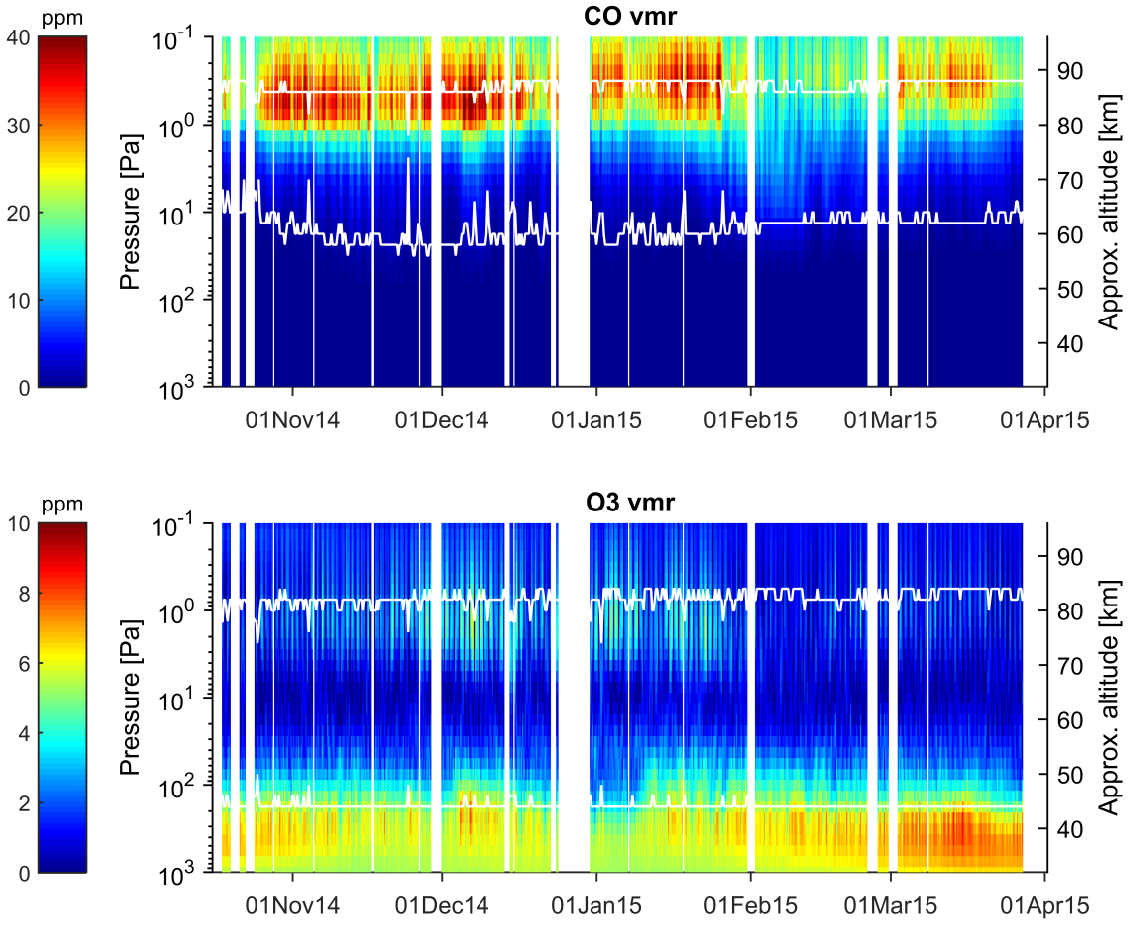

Figure 8: Retrieved vmr of CO and O3 (ppm) for the measurement period. The white lines mark where the a priori affects the result with 20 % (< 20 % between the lines).

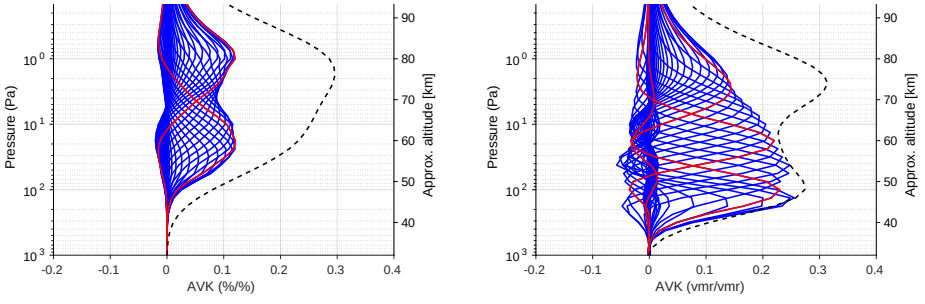

Figure 9: Averaging kernels for CO and O_3 for November 16 2014. The kernels at 100, 18, 2.4 Pa for O_3 and 18, 1 Pa for CO are highlighted with red lines. The dashed line is the measurement response divided by 4.

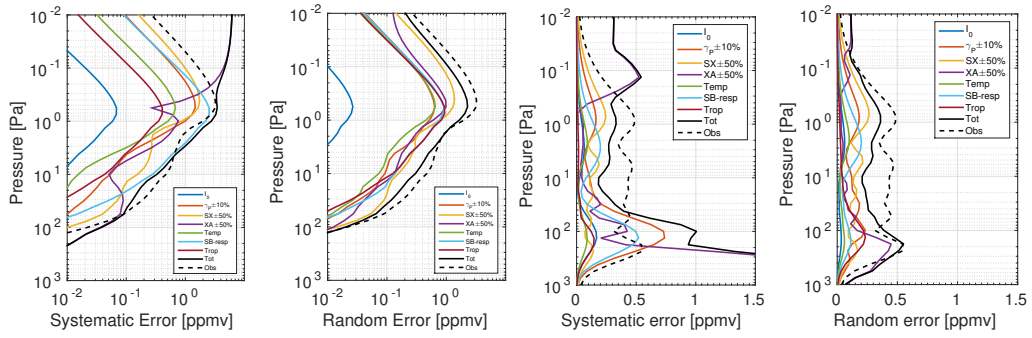

Figure 10: Estimated systematic and random errors for CO (two leftmost panels) and O_3 (two rightmost panels) estimated by perturbation of forward model and retrieval parameters. The parameters perturbed are line strength, I_0, pressure broadening parameter, γ_p, a priori variance, SX, a priori profile, XA, a priori temperature profile, $Temp$, the sideband response $SB - resp$ and the tropospheric correction $Trop$. The total RMS error expected is given by the solid black line, and the observation error by the dashed black line.

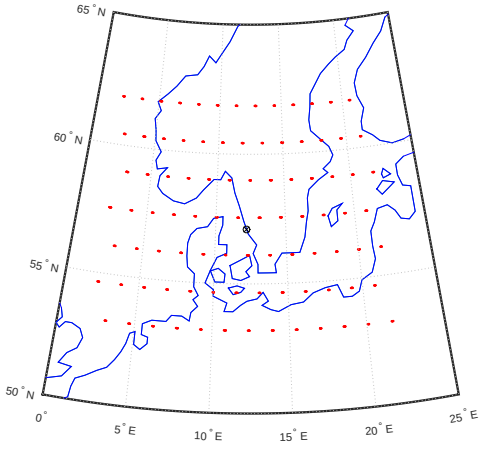

Figure 11: Collocations MLS–OSO.

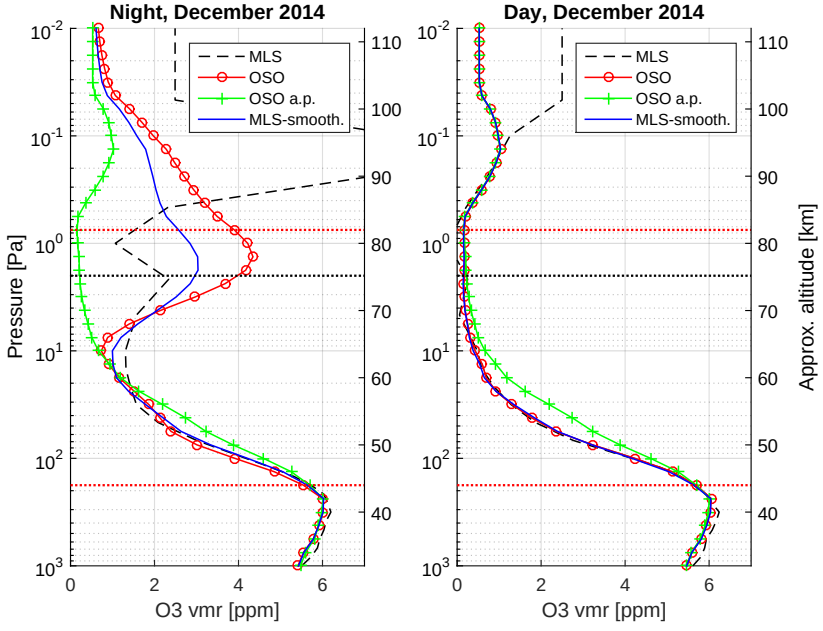

Figure 12: Average night and day vertical profiles of O_3 from December 2014. The a priori affects the OSO result < 20 % between the red dotted horizontal lines. The black dotted horizontal line mark the upper altitude for the MLS data.

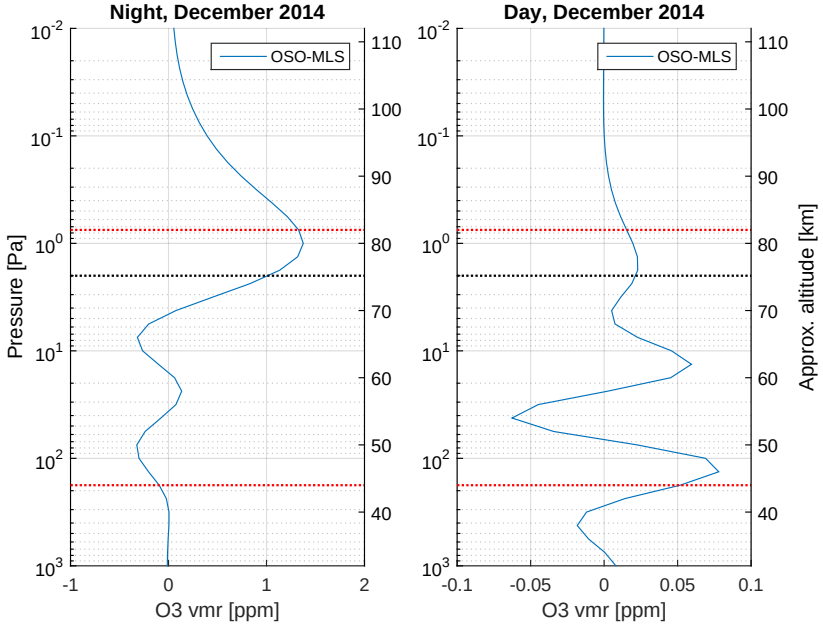

Figure 13: Difference between OSO and MLS (OSO-MLS) for night and day vertical profiles of O_3 from December 2014. The a priori affects the OSO result < 20 % between the red dotted horizontal lines. The black dotted horizontal line mark the upper altitude for the MLS data.

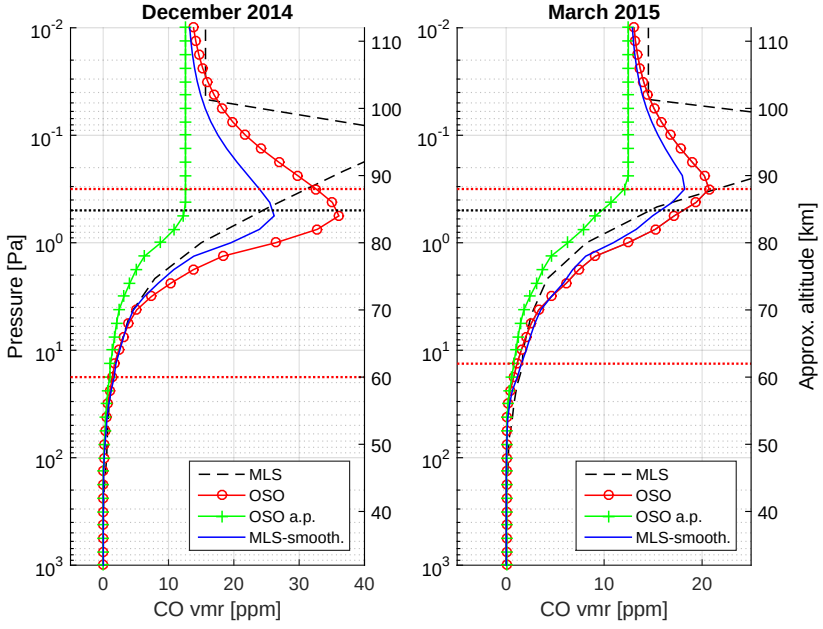

Figure 14: Average December and March vertical profiles of CO. The a priori affects the OSO result < 20 % between the red dotted horizontal lines. The black dotted horizontal line mark the upper altitude for the MLS data.

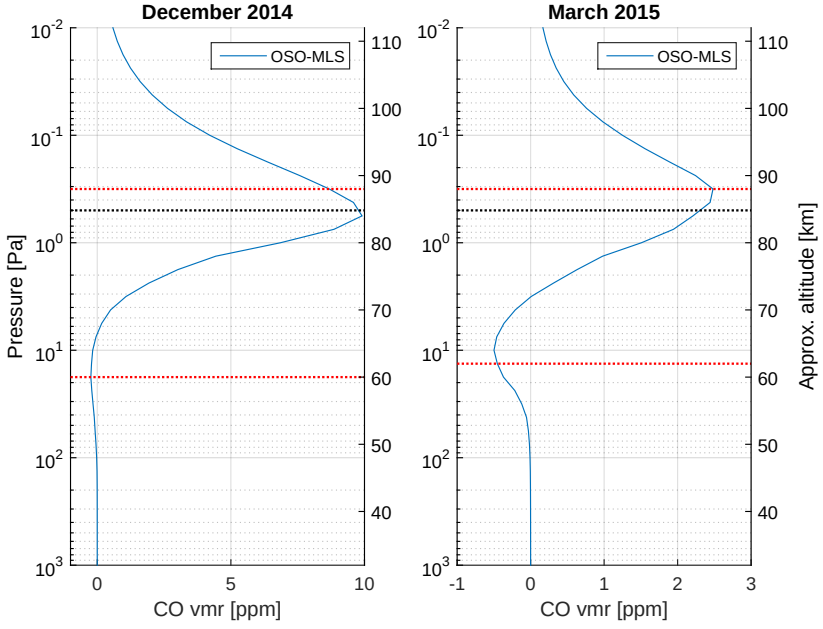

Figure 15: Difference between OSO and MLS (OSO-MLS) for December and March vertical profiles of CO. The a priori affects the OSO result < 20 % between the red dotted horizontal lines. The black dotted horizontal line mark the upper altitude for the MLS data.

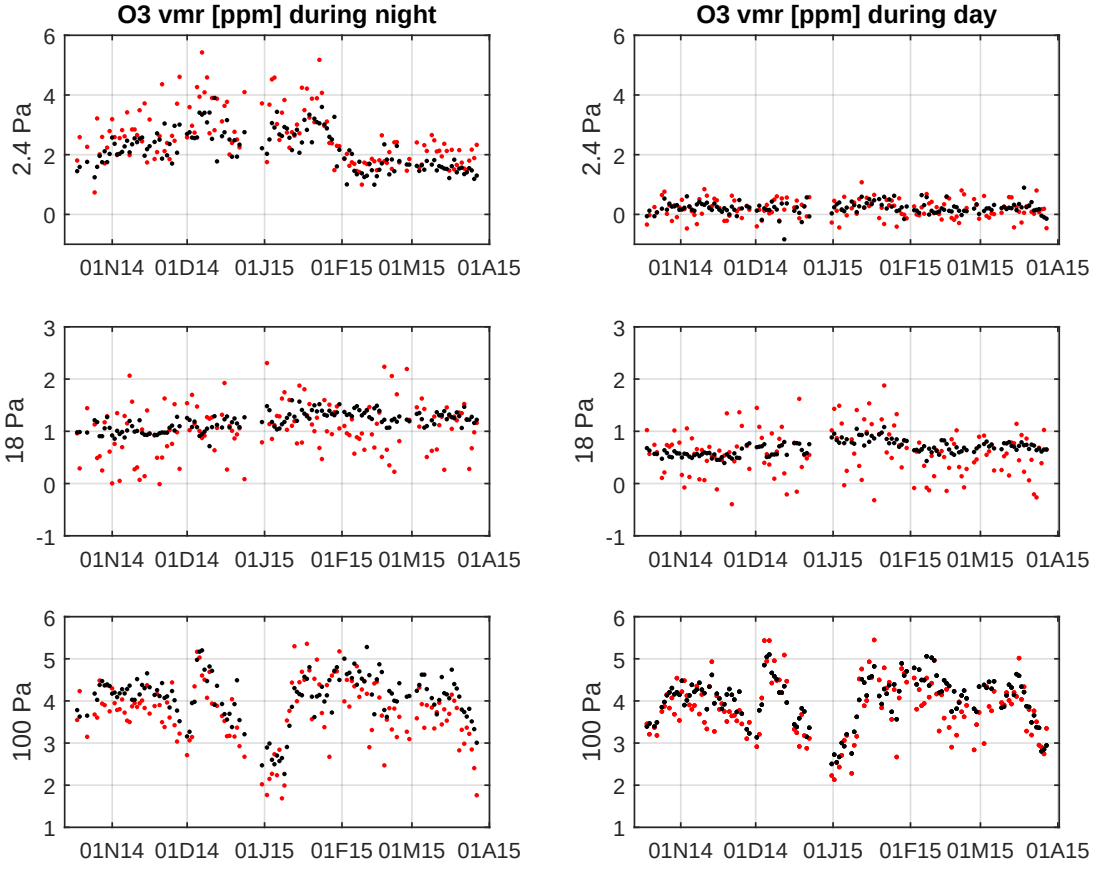

Figure 16: O_3 at 3 different altitudes, October–April (ddmyy), OSO (red), MLS (black).

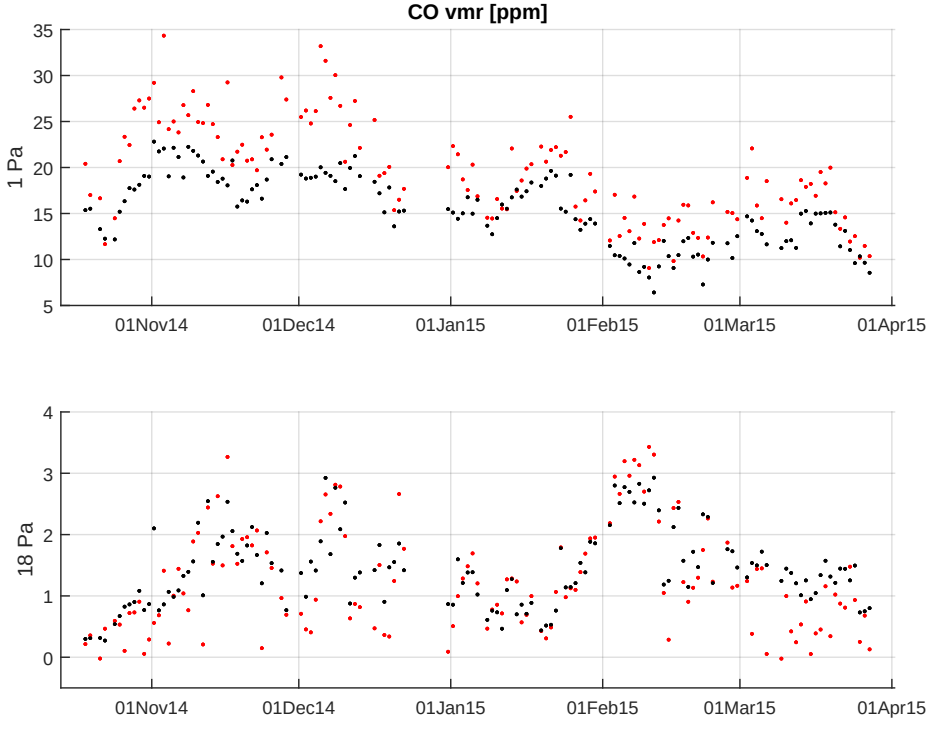

Figure 17: CO at 2 different altitudes, October–April (ddmmmyy), OSO (red), MLS (black).

Manuscript prepared for Geosci. Instrum. Method. Data Syst.
with version 2014/09/16 7.15 Copernicus papers of the LaTeX class copernicus.cls.
Date: 23 December 2015

A compact receiver system for simultaneous measurements of mesospheric CO and O_3

P. Forkman[1], O. M. Christensen[1], P. Eriksson[1], B. Billade[1], V. Vassilev[2], and V. M. Shulga[3]

[1]Department of Earth and Space Sciences, Chalmers University of Technology, Sweden
[2]Department of Microtechnology and Nanoscience, Chalmers University of Technology, Sweden
[3]Institute of Radio Astronomy, Ukrainian Academy of Sciences

Correspondence to: P. Forkman (peter.forkman@chalmers.se)

Abstract. During the last decades, ground-based microwave radiometry has matured to an established remote sensing technique for measuring vertical profiles of a number of gases in the stratosphere and the mesosphere. Microwave radiometry is the only ground-based technique that can provide vertical profiles of gases in the upper stratosphere and mesosphere both day and night, and even during cloudy conditions. Except for microwave instruments placed at high altitude sites, or at sites with dry atmospheric conditions, only molecules with significant emission lines below 150 GHz, such as CO, H_2O and O_3 can be observed. Vertical profiles of these molecules can give important information about chemistry and dynamics in the middle atmosphere.

Today these measurements are performed at relatively few sites, more simple and reliable instrument solutions are required to make the measurement technique more widely spread. This need is today urgent as the number of satellite sensors observing the middle atmosphere is about to decrease drastically. In this study a compact double-sideband frequency-switched radiometer system for simultaneous observations of mesospheric CO at 115.27 GHz and O_3 at 110.84 GHz is presented.

The radiometer, its calibration scheme and observation method are presented. The retrieval procedure, including compensation of the different tropospheric attenuation at the two frequencies, and error characterization are also described. The first measurement series from October 2014 until April 2015 taken at the Onsala Space Observatory, OSO, (57° N, 12° E) is analysed. The retrieved vertical profiles are compared with co-located CO and O_3 data from the MLS instrument on the Aura satellite. The datasets from the instruments agree well to each other. The main differences are the higher OSO volume mixing ratios of O_3 in the upper mesosphere during the winter nights and the higher OSO volume mixing ratios of CO in the mesosphere during the winter. The low bias of mesospheric winter values of CO from MLS compared to ground-based instruments has been reported earlier.

1 Introduction

Simultaneous measurements of mesospheric gases with different chemical lifetimes, such as ozone (fraction of hour) and carbon monoxide (order of weeks), can give important information on both chemical and dynamical processes in this altitude region. The middle atmospheric distribution of ozone, O_3, is characterized by a stratospheric volume mixing ratio (vmr) peak at $\sim 35\,\mathrm{km}$ altitude, first described by Chapman (1930), and a diurnally varying secondary mesospheric peak at $\sim 90\,\mathrm{km}$ altitude (Hays and Roble, 1973). The secondary peak is formed during night by reactions between atomic and molecular oxygen and partly destroyed by photo-dissociation during day. Additionally, a tertiary, also diurnally varying, peak is present at $\sim 72\,\mathrm{km}$ in winter at high latitudes (Marsh et al., 2001; Hartogh et al., 2011).

The main source of middle atmospheric carbon monoxide, CO, is photo-dissociation of carbon dioxide, CO_2, in the upper mesosphere/thermosphere region. Reactions with hydroxyl, OH, is the main sink. Low vmr in the stratosphere, significantly increasing values with altitude up through the mesosphere, and high values in the thermosphere is the typical vertical distribution of middle atmospheric CO (Lopez-Puertas et al., 2000).

The vertical component of the mesospheric dynamics can at high latitudes be described as an annual cycle with air ascending in the summer and descending in the winter. The horizontal component is weak during summer, while it is controlled by the polar vortex and stronger during winter (Brasseur and Solomon, 2008). Due to its long lifetime in the mesosphere CO is an excellent tracer of dynamics in this altitude region, especially at high latitudes during winter (Hoffmann, 2012) .

Microwave radiometry is the only ground-based remote-sensing technique that both day and night, even during cloud cover, can provide vertical profiles of different trace gases up to the mesopause region. In microwave radiometry, emission spectra from rotational transitions within the observed molecular species are measured. Due to pressure broadening, the measured spectra contain information about the vertical distribution of the molecule. Except from very dry sites, or sites at high altitudes, only frequencies up to about 150 GHz can be observed since higher frequencies are effectively attenuated by tropospheric water (Janssen, 1993). The gases CO, H_2O, O_2 and O_3 all have sufficiently strong emissions at frequencies below 150 GHz. Thus, there is a need for simple and reliable radiometers operating below 150 GHz, since they can observe important gases from almost every ground-based site. If such a radiometer could also observe two of the gases simultaneously (e.g. O_3 and CO) it would be even more useful for the microwave community.

Dicke-switching is the generally used observation technique in microwave radiometry, meaning that the radiation from the sky is compared to an equally intense reference source to diminish the effects of gain variations. Three main Dicke-switching variants can be recognized. In load-switching the reference is a blackbody or other noise source. The zenith sky is the reference in sky-switching. In frequency-switching the mixer's local oscillator frequency, LO, is changed between the signal and the reference phases. Parrish (1994) gives an overview of the mentioned observation methods.

Since the pioneering work by Caton et al. (1968) several heterodyne radiometer systems dedicated for middle atmospheric O_3 observations have been developed, primarily for the relatively strong O_3 transitions at 110.8 and 142.2 GHz. Lobsiger (1987) developed a load-switching technique where the sky, a liquid nitrogen cold load at 80 K, and an ambient load were measured during each observation cycle; several 142.2 GHz instruments use variants of this method ~~(Hartogh et al., 1991; Peter et al., 1998; Studer et al., 2013)~~ (Hartogh et al., 1991; Peter et al., 1998; Hocke et al., 2007; Palm et al., Recently the technique has been developed further by implementing a noise diode and a Peltier cooled load (Fernandez et al., 2015).

~~Nedoluha et al. (2015) use~~ Parrish et al. (1988) and Parrish et al. (1992) developed a sky-switching procedure at 110.8 GHz ~~developed by Parrish et al. (1988) and Parrish et al. (1992) ,~~ where the reference zenith beam passes a "lossy" window at Brewster angle to compensate for the higher intensity in the signal beam. This observation technique has been widely used, for example by Connor et al. (1994) , Boyd et al. (2007) and Nedoluha et al. (2015) .

The drawback of load and sky switching is that a reference is observed during half the observation time. The advantage of frequency-switching is that the wanted sky emission is present in both signal and reference, which doubles the effective observation time compared to load or sky switching. The drawback is that the frequency dependent impedances in the frontend components can change the overall gain between the signal and reference phases if the frequency throw is more than $\sim$ ~~20~~ 30 MHz. As the pressure broadening in the stratosphere exceeds the bandwidth limitation of frequency-switching this method can only be used for studies of mesospheric and upper stratospheric O_3. However, narrow mesospheric lines can be resolved with a higher temporal resolution using a frequency switched configuration compared to load or sky switching due to the efficient time usage. Nagahama et al. (1999) used a frequency throw of 30 MHz and presented vertical O_3 profiles in the altitude range 30–80 km.

Microwave spectra of CO are much narrower than spectra of O_3 due to the different residence altitudes for the two molecules, which make frequency-switching suitable. Waters et al. (1976) made the first microwave CO observations, using absorption measurements against the sun and on-source off-source switching (the standard Dicke method used by radio astronomers). Kunzi and Carlson (1982) , Aellig et al. (1995), Forkman et al. (2003) and Forkman et al. (2012) made frequency-switched observations of CO at 115.3 GHz. de Zafra and Muscari (2004) , Hoffmann et al. (2011) and Straub et al. (2013) used load-switching to observe CO at 230.5 GHz.

The mixer is the key component in the heterodyne radiometer. The incoming radio frequency, RF, is mixed with the LO, and the output intermediate frequency, IF, is a mix of the upper and lower sidebands. To avoid the unwanted sideband (or image band) the radiometer can be operated in single sideband mode where the image band is suppressed before the mixing. If none of the sidebands are suppressed, we have a double-sideband system which makes it possible to observe signals from the two bands simultaneously. The disadvantages are that the sideband ratio has to be known and

the tropospheric attenuation has to be corrected individually for the two bands if the tropospheric opacity differ between the two frequencies. Except for instruments where the LO is placed on the center of the observed line, e.g. the 183 GHz water vapor radiometer for the ALMA project (Emrich et al., 2009), most ground-based radiometers today are single sideband instruments. One exception is the 110–116 GHz radiometer for CO and O_3 observations designed and operated by Piddyachiy et al. (2010).

In this study we present the first simultaneous measurements of mesospheric O_3 at 110.8 GHz and CO at 115.3 GHz made by a ground-based, double sideband and frequency-switched radiometer system. The system is operated at the Onsala Space Observatory, OSO, (57.4° N, 11.9° E). The instrument, its calibration scheme, the retrieval procedure and the first results are introduced. Section 2 describes the receiver system and the calibration and Sect. 3 presents the inversions. The results are given in Sect. 4 and the error analyses is described in Sect. 5. Section 6 shows a satellite comparison, and Sect. 7 gives a summary and the conclusions.

2 Instrument and observation technique

We present a double-sideband, frequency-switched heterodyne receiver system for simultaneous spectral measurements of the atmospheric O_3 $6_{15} \rightarrow 6_{06}$ transition at ~~110.83604~~110.836 GHz and the CO 1→0 transition at ~~115.27120~~115.271 GHz~~, observed at an elevation~~ . Model calculations show that the highest signal to noise ratios of the observed mesospheric emission from both CO and O_3 are found at observation elevations larger than ≈ 40°. To avoid Doppler shift effects due to zonal winds in the middle atmosphere an elevation as close to the zenith direction as possible is preferable. To get close to zenith but to avoid reflections from the housing structure an elevation of 80° ~~. A block diagram of the receiver is shown in Fig. 1 and technical specifications are given in Table 1. A~~ was chosen. A 2-bit autocorrelator is used as backend spectrometer. The bandwidth is 20 MHz and the nominal resolution is 25 kHz (800 delay channels). This resolution is sufficient as the smallest line-widths expected from the CO and O_3 line measured due to Doppler broadening has full width, half maximum values of 220 kHz and 160 kHz respectively. A block diagram of the receiver is shown in Fig. 1 and technical specifications are given in Table 1.

2.1 Frontend description

The receiver frontend includes a four stage Low Noise Amplifier, LNA, a fundamental resistive mixer, and a ×4 LO chain, all integrated onto a single Monolithic Microwave Integrated Circuit, MMIC, using a 100 nm mHEMT process. The mixer provides a conversion loss of 8–10 dB for LO power of 4 dBm. The LO chain consists of two doublers followed by a two stage power amplifier. The amplifier delivers about 5 dBm of LO signal to the mixer with an input power of 9 dBm at 29.5

GHz. Vassilev et al. (2010) gives more details on the performance of the receiver and a breakout of the LNA.

2.2 Calibration

Brightness temperature, $T_{\rm b}$, derived from the Rayleigh-Jeans approximation of the Planck law, is often used as a measure of the received radiation in microwave radiometry. The Rayleigh-Jeans approximation can be written:

$$B(\lambda,T) \approx \frac{2kT}{\lambda^2} \tag{1}$$

where B is the brightness describing the energy emitted by a black body, λ the wavelength, k the Boltzmann constant, and T the physical temperature of the black body. Equation (1) is valid when $h\nu \ll kT$, where h is the Planck constant and ν is the frequency. The brightness temperature, $T_{\rm b}$, is defined as:

$$T_{\rm b} = I(\lambda)\frac{\lambda^2}{2k} \tag{2}$$

The proportionality between the received radiation, I, and $T_{\rm b}$ is the reason why $T_{\rm b}$ is used in microwave radiometry. The antenna temperature, $T_{\rm a}$, is defined as the convolution between the observed brightness temperature distribution and the antenna pattern. In the rest of this section a pencil beam is assumed implying that the measured antenna temperature, $T_{\rm a}$, is equal to the brightness temperature, $T_{\rm b}$, in the observed direction.

The system temperature, the radiometer output power measured by the spectrometer, is defined as $T_{\rm sys} = T_{\rm a} + T_{\rm rec}$, where the receiver temperature, $T_{\rm rec}$, is a measure of the power generated in the components along the radiometer system transmission line where the first stages as LNA and mixer contribute the most.

In the mixer, the RF input spectrum is folded around the LO to form the IF output spectrum (see Fig. 2). The IF bandpass filter selects the position and width of both the lower sideband, LSB, and the upper sideband, USB. If any of the two sidebands are terminated ahead the mixer the receiver is called single sideband, SSB. We use the mixer in true double sideband mode, DSB, where LSB is centered at 110.84 GHz and USB at 115.27 GHz, see simulated spectra in Fig. 3. The contributions from LSB and USB are weighted with their relative frontend gains and then added to form $T_{\rm sys}$ (Ulich and Haas, 1976). The system temperature of a calibration blackbody load that fills the antenna beam, $T_{\rm sys}(load)$, can thus be expressed as:

$$T_{\rm sys}(load) = G_{\rm L}\Big(T_{\rm load}(L) + T_{\rm rec}(L)\Big) + G_{\rm U}\Big(T_{\rm load}(U) + T_{\rm rec}(U)\Big) \tag{3}$$

where L and U mark the contributions from the LSB and USB frequencies, $G_{\rm L}$ and $G_{\rm U}$ are the normalized relative frontend power gains ($G_{\rm L} + G_{\rm U} = 1$) in the two sidebands (also called sideband

responses), and $T_{\rm load}$ is the temperature of the blackbody load. The sum of the two contributions to the receiver temperature is denoted $T_{\rm rec}$, i.e. $T_{\rm rec} = G_{\rm L}T_{\rm rec}(L) + G_{\rm U}T_{\rm rec}(U)$. If it is assumed that the load is a blackbody in both sidebands, Eq. 3 is hence simplified to:

$$T_{\rm sys}(load) = T_{\rm load} + T_{\rm rec} \tag{4}$$

To estimate $T_{\rm rec}$ two blackbody loads with physical temperatures $T_{\rm hot}$ (ambient load) and $T_{\rm cold}$ (77 K load) are observed each month. $T_{\rm rec}$ can then be estimated using:

$$\frac{P_{\rm cold}}{P_{\rm hot} - P_{\rm cold}} = \frac{T_{\rm sys}(cold)}{T_{\rm sys}(hot) - T_{\rm sys}(cold)} = \frac{T_{\rm cold} + T_{\rm rec}}{T_{\rm hot} - T_{\rm cold}} \rightarrow T_{\rm rec} = P_{\rm cold}\frac{T_{\rm hot} - T_{\rm cold}}{P_{\rm hot} - P_{\rm cold}} - T_{\rm cold}, \tag{5}$$

which is the classical Y-factor method, where $P_{\rm hot}$ and $P_{\rm cold}$ are the measured powers observing the two loads. The system temperature when observing the sky, $T_{\rm sys}(sky)$, is given by:

$$T_{\rm sys}(sky) = G_{\rm L}T_{\rm a}(L) + G_{\rm U}T_{\rm a}(U) + T_{\rm rec} \tag{6}$$

where $T_{\rm a}(L)$ and $T_{\rm a}(U)$ are the antenna temperatures at 110.84 GHz and 115.27 GHz, respectively.

The following calibration procedure is performed each 15 minutes to estimate the sky brightness temperature:

$$\frac{P_{\rm load} - P_{\rm sky}}{P_{\rm sky}} = \frac{T_{\rm sys}(load) - T_{\rm sys}(sky)}{T_{\rm sys}(sky)} = \frac{\left(T_{\rm load} + T_{\rm rec}\right) - \left(G_{\rm L}T_{\rm a}(L) + G_{\rm U}T_{\rm a}(U) + T_{\rm rec}\right)}{G_{\rm L}T_{\rm a}(L) + G_{\rm U}T_{\rm a}(U) + T_{\rm rec}}, \tag{7}$$

where $P_{\rm load}$ and $P_{\rm sky}$ are the measured powers observing the load and the sky, respectively. The weighted mean of the antenna temperatures at the two sidebands,

$$T_{\rm sky} = G_{\rm L}T_{\rm a}(L) + G_{\rm U}T_{\rm a}(U) \tag{8}$$

can be derived from Eq. 7 since $T_{\rm load}$ and $T_{\rm rec}$ are known. Since a pencil beam is assumed, $T_{\rm sky}$ is denoted as sky brightness temperature (see above). An error in the estimate of $T_{\rm rec}$ introduces an error in the estimation of $T_{\rm sky}$. The hot-cold calibrations (Eq. 5) performed so far indicate that the variation in $T_{\rm rec}$ is less than 3 %. Equations 7 and 8 then gives that the error in $T_{\rm sky}$ is less than 2 %.

The sky brightness temperature at 115.3 GHz is 35–60 K higher than at 110.8 GHz. This is explained both by the frequency variation of absorption due to tropospheric water and by the fact that 115.3 GHz is situated higher on the wing of the 118 GHz O_2 line, see the broadband spectra in Fig. 4 estimated from one year of radiosonde data taken at Landvetter Airport, 38 km N.E. of Onsala Space Observatory.

2.3 Frequency-switching

The particular Dicke-switch method used here is frequency-switching. In this method the frontend mixer LO frequency, f_{LO}, is switched between the phases of the signal, S, and the reference, R, in the measurement cycle. $f_{LO}(S) = f_c - \Delta f$ and $f_{LO}(R) = f_c + \Delta f$ where f_c is the mean of the

two local oscillator frequencies. Owing to $S - R$ being a difference, the spectra will show both a negative and a positive peak in the observed spectral characteristic, with a separation equal to the frequency throw, $2\Delta f$. An averaged spectrum is seen in Fig. 5. The spectrum is a combination of double-sideband measurement and frequency-switching which explains the positions of the negative and positive peaks of O_3 from the lower and CO from the upper sidebands.

Using frequency-switching during the observation cycle we record

$$\begin{aligned}\Delta T_{\rm sky} &= \frac{\Delta P}{P_{\rm load} - P_{\rm sky}}(T_{\rm load} - T_{\rm sky}) = T_{\rm sky}(-\Delta f) - T_{\rm sky}(+\Delta f) \\ &= G_{\rm L}\big(T_{\rm a}(L,-\Delta f) - T_{\rm a}(L,+\Delta f)\big) + G_{\rm U}\big(T_{\rm a}(U,-\Delta f) - T_{\rm a}(U,+\Delta f)\big) \end{aligned} \quad (9)$$

where $\Delta T_{\rm sky}$ is the difference in brightness temperatures (since we assume a pencil beam) and $\Delta P = P_{\rm S} - P_{\rm R}$ is the difference in the measured powers between the two frequencies $f_{LO}(S)$ and $f_{LO}(R)$. The calibration procedure gives $P_{\rm load}$, $P_{\rm sky}$, $T_{\rm load}$ and $T_{\rm sky}$.

2.4 Sideband ratio

The sideband responses G_L and G_U have to be known accurately to be able to retrieve vertical profiles from the measured spectra. The measurement of the sideband responses relies on inserting a continuous wave (CW) of known amplitude in the RF path of the instrument and to measure the down converted IF signal. The measurement is then repeated over several RF/IF frequencies to get the overall sideband response.

Figure 6 shows the setup used for the measurement of the sideband response of the instrument. A millimeter wave source generates a CW in the 110.5 - 115.5 GHz frequency band. A mm-wave spectrum analyzer extender measures the amplitude of the CW signal. The radiometer frontend, and a spectrum analyzer measure the amplitude of the down converted IF. All the measurement equipments are synchronized to a common reference clock.

In the current measurement setup, the mm-wave source is first connected to the extenders to measure the amplitude of the CW signal while sweeping the source frequency $f_{\rm RF} = 110.5 \rightarrow 115.5$ GHz. After taking the RF power sweep, the CW source is connected to the radiometer, and the amplitude of the down converted IF is recorded while sweeping the RF frequency as before. The local oscillator frequency of the radiometer is held constant at $f_{\rm LO} = 113.055$ GHz (28.26375×4). The two sidebands after the IF amplifier bandpass response are,

$$\begin{aligned} f_{\rm LSB} &= 113.055 - (1.5 \rightarrow 2.5) = 110.555 \rightarrow 111.555 \text{ GHz} \\ f_{\rm USB} &= 113.055 + (1.5 \rightarrow 2.5) = 114.555 \rightarrow 115.555 \text{ GHz} \end{aligned} \quad (10)$$

The sideband gains of the instrument can then be estimated by taking the ratios of the measured power at RF frequencies and IF frequencies as,

$$g_{\rm LSB} = \frac{P_{\rm IF}^{\rm LSB}}{P_{\rm RF}^{\rm LSB}} \quad \text{and} \quad g_{\rm USB} = \frac{P_{\rm IF}^{\rm USB}}{P_{\rm RF}^{\rm USB}} \quad (11)$$

The measured sideband ratio, $g_{\mathrm{LSB}}/g_{\mathrm{USB}}$, is close to unity. However, standing-wave patterns are seen in both the measured RF and IF powers, which introduce an error in our estimation of the sideband ratio. These standing waves have to be minimized in order to improve the quality of the measurements. Nevertheless, the results obtained so far with the current setup are promising. The linear normalized relative frontend power gains, ~~G_{L} and G_{U}~~ $G_{\mathrm{L}} = g_{\mathrm{LSB}}/(g_{\mathrm{LSB}} + g_{\mathrm{USB}})$ and $G_{\mathrm{U}} = g_{\mathrm{USB}}/(g_{\mathrm{LSB}} + g_{\mathrm{USB}})$ are estimated at 0.5 ± 0.05 and 0.5 ∓ 0.05 respectively.

2.5 Water vapor radiometer for tropospheric measurements

Due to the nature of DSB mixers, the measured sky brightness temperature is the mean of the brightness temperatures at the lower and upper sideband frequencies, weighted with their respectively sideband gains G_{L} and G_{U}. To be able to correct for the tropospheric attenuation an estimation of the sky brightness temperatures at these two frequency regimes are needed. The OSO site operates two dual-frequency radiometers, ASTRID ~~and KONRAD~~(Elgered and Jarlemark, 1998) and KONRAD (Stoew et al., 2000) , that continuously measure the sky brightness temperature in different directions at 21.0 / 31.4 GHz and 20.6 / 31.6 GHz respectively, see Table 2. The data is used to provide independent corrections for the water vapor induced time delay which affect the accuracy of the geodetic VLBI observations performed at the observatory (Elgered and Jarlemark, 1998). ~~In Section 3.3 the use of the~~ For our purpose, the calibrated zenith sky brightness temperatures, from these instruments ~~,~~ will be used in Section 3.3 to estimate the tropospheric opacity at 110.84 and 115.27 GHz~~, is discussed~~.

3 Retrievals

3.1 Forward model

For the retrievals presented in this paper, the Atmospheric Radiative Transfer Simulator (ARTS v.2.3.145) is used as a forward model (Buehler et al., 2005; Eriksson et al., 2011). It is a general radiative transfer model that can provide Jacobians for a large number of different measurement geometries and systems. A 1-D simulation setup is applied using a pressure grid ranging from $1.3 \cdot 10^5$ Pa (0 m) to $7.5 \cdot 10^{-4}$ Pa ($\sim$130 km) with a spacing of $\sim$250 m. Line-by-line simulations of frequencies in two bands between 110.816-110.856 GHz and 115.251-115.291 GHz are run with a monochromatic frequency grid having a spacing of 4.2 MHz at the far end of each band, decreasing to 14.13 kHz in the center of each band. The instrument is modeled as a dual sideband receiver with a flat 50% sideband response in each band. Each channel of the autocorrelator is modeled to have a ~~channels~~ channel response corresponding to an ideal Hanning filter with a FWHM of 50 kHz. The antenna is modeled as a pencil beam antenna looking at a zenith angle of 10°, and the instrument is positioned at ground level.

The spectroscopic lines included in the forward model are CO at 115.27 GHz, O_3 at ~~110.5, 110.7, 110.8 and 115~~ 110.77, 110.84, 111.05 and 114.97 GHz as well as complete absorption models for ~~molecular oxygen, molecular~~ oxygen, nitrogen, water ~~vapor~~ vapour and liquid water ~~. A summary of the spectroscopic parameters is given in Tables 4 and 3. For~~ (Table 3). The spectrocopic parameters are taken from an updated version of the Verdandi database (Eriksson and Merino, 1997) . Line positions and strengths of the database are mainly taken from the JPL-catalogue (Pickett et al., 1998) , while the broadening parameters are mainly taken from HITRAN. The discussed version of Verdandi was created 2002, using the JPL data of that time and HITRAN 2001 (Rothman et al., 2003) . For a number of transitions the JPL and HITRAN data are replaced with hand-picked data from the ~~emission lines the line position and strength is taken from JPL-catalog (Pickett et al., 1998) while the~~ literature. This includes the O_3 line at 110.84 GHz, where the presssure broadening parameters are taken from ~~HITRAN04 (Rothman et al., 2005) .~~ (Connor and Radford, 1986) . A summary of the spectroscopic parameters is given in Table 4.

~~Comparing~~ When comparing the measurements to a forward model simulation with the line positions from the JPL-catalogue~~(as well as HITRAN04 (Rothman et al., 2005))~~ , the simulated CO emission occurs at the same frequency in both the simulation and our measurements, while the simulated O_3 line emission at 110.8360400 GHz shows a clear frequency offset compared to the measurements. Since the CO line is positioned correctly a shift in the LO frequency cannot explain the frequency offset of the O_3 line. This ~~thus~~ indicates that the databases have the wrong frequency for this spectral line. Best agreement between the forward model and measurement was found if the line was shifted 117 kHz (specified uncertainty is 50 kHz) to 110.8359230 GHz. Note that for the purpose of this study, the exact reason for this shift is not relevant, since a pure shift in frequency does not affect the retrieved concentrations as long as the modeled and measured spectra are consistent.

3.2 Retrieval model

To retrieve CO and O_3 concentrations from the measured spectra, the maximum a posteriori method, also called optimal estimation method, OEM, (Rodgers, 2000) is used as implemented in the updated version of the Qpack software (Eriksson et al., 2005). Given the spectra with assumed errors and a statistical distribution of the measured atmosphere, the method returns the maximum a posteriori estimate combining these two pieces of information. If the atmosphere and possible instrument parameters are described by a state vector $\mathbf{x}$, the measured spectrum by $\mathbf{y}$, and the a priori atmosphere as $\mathbf{x_a}$, the estimated atmosphere is

$$\hat{\mathbf{x}} = \mathbf{x_a} + (\mathbf{K^T S_\epsilon^{-1} K} + \mathbf{S_a^{-1}})\mathbf{K^T S_\epsilon^{-1}}(\mathbf{y} - \mathbf{K x_a}), \tag{12}$$

where $\mathbf{S}_\epsilon$, $\mathbf{S_a}$ are the covariance matrices describing the uncertainty (assuming normal distribution) in the measurements and a priori atmosphere respectively. The Jacobian- or Weighting function ma-

trix, $\mathbf{K} \equiv \partial \mathbf{y} / \partial \mathbf{x}$, is the linearized derivative of the forward model and describes how a change in any of the state vector elements influences the measured spectrum. Tropospheric attenuation introduces a non-linearity in Eq. 12, i.e. $\mathbf{K}$ is a function of $\mathbf{x}$. To account for this Eq. 12 is solved iteratively using a Gauss-Newton method, and convergence is concidered to be reached when the change in the state vector betweem two iterations, normalized by the retrieved covariance, is less than 0.01 times the length of the state vector.

To save computational resources, the inverse problem (Eq. 12) is solved on a coarser grid than the forward model. The state vector is specified to contain the concentration ~~(vmr)~~ of CO ~~and~~ as a fraction of the apriori profile and the concentration of O_3 in vmr at pressure levels between $1 \cdot 10^5$ Pa and $1 \cdot 10^{-3}$ Pa with a spacing of 2 km. In addition to CO and O_3, the state vector includes the concentration (in units relative to the a priori~~concentration~~) of water vapor and liquid water between $1 \cdot 10^5$ Pa and $1.3 \cdot 10^3$ Pa with a spacing of 1 km. These species are included to correct for tropospheric influence on the mesospheric emission (see Sec. 3.3). The elements of the state vector containing these species are referred to as $\mathbf{x^{trop}}$. To account for baseline ripple in the instrument a 3^{rd} order polynomial fit is performed, and its coefficients are stored in the four last elements of the state vector.

Each of these state vectors variables needs a priori values stored in $\mathbf{x_a}$. The a priori profile for CO and O_3 is based on a climatology containing the monthly zonal mean values from ACE-FTS at 57.5 °N. It is based on the method described in Jones et al. (2012) but with an updated data quality classification (Sheese et al., 2015). The climatology covers pressure levels from $1 \cdot 10^5$ to $1 \cdot 10^{-4}$ Pa, but lacks data for certain months and altitudes. A linear interpolation between months is used if values are missing. Above $1 \cdot 10^{-4}$ Pa the climatology is extrapolated using the vmr value from $1 \cdot 10^{-4}$ Pa. The temperature, altitude and pressure relationship is, above 100 Pa, taken from a climatology based on the MSISE-90 model (Hedin, 1991), while below 5000 Pa it is based on the database for used tropospheric correction (see 3.3). Between 5000 and 100 Pa the temperatures are obtained by a linear interpolation between the two datasets.

To solve Eq. 12, $\mathbf{S}_\epsilon$ and $\mathbf{S_a}$ must be specified. We describe these covariances with a standard deviation and a correlation function (see e.g. Christensen and Eriksson (2013)). For $\mathbf{S}_\epsilon$ the standard deviation is equal to the thermal noise estimated from the measurements (~ 0.07 K) and correlation between channels is modeled as a Gaussian correlation function with a correlation length equal to 1.6 channels. The specification of $\mathbf{S_a}$ depends on which state vector variable the elements describe. The covariance of CO is described with a standard deviation equal ~~to 1 plus~~ 100% of the ~~annual mean CO profile() from the a priori~~apriori profile. This large uncertainty is needed to ensure a reasonable sensitivity despite the low signal to noise ratio of the CO measurements. For O_3 the standard deviation is described simply as 4 ppmv for all altitudes, and for temperature it is set to 5 K for all altitudes. The correlation between altitudes is set to follow a linear correlation function with a correlation length of 8 km for both species and the temperature. Tropospheric water vapor

has a standard deviation equal to 10 % of the a priori value and a linear correlation function with a correlation length of 8 km, while the liquid water has a standard deviation equal to 100% of the a priori value, and no correlation between altitudes. The baseline fit has a standard deviation of 4 K for all coefficients.

3.3 Tropospheric correction

In order to accurately estimate the CO and O_3 concentrations in the mesosphere, the tropospheric attenuation needs to be accounted for. A common way of to achieve this is to model the troposphere as a single layer, with an effective temperature and opacity, and performing a correction of the observed spectra prior to performing the retrieval. For the DSB receiver the difference in the opacity between the two sidebands is too large for such an approach to work, and as such the troposphere needs to be included directly into the forward model. This is done in two steps. First an atmosphere is selected from a database of tropospheric scenarios. The atmosphere selected is the one minimizing the following cost function

$$\chi^2 = \left(\mathbf{y^{trop}} - f(\mathbf{x^{trop}})\right)^T \mathbf{S}_\epsilon^{\mathbf{trop}} \left(\mathbf{y^{trop}} - f(\mathbf{x^{trop}})\right), \tag{13}$$

where $\mathbf{y^{trop}}$ is the measurements used for the tropospheric correction, $f(\mathbf{x^{trop}})$ the radiance from the modeled troposphere and $\mathbf{S}_\epsilon^{\mathbf{trop}}$ the covariance matrix describing the measurement noise for the measurements used for the tropospheric retrieval. For the DSB instrument $\mathbf{y^{trop}}$ consists of two elements, the mean $T_{\rm sky}$ measured across all channels, $T_{\rm sky}^{\rm mean}$, and the ground temperature at OSO at the time of the measurement, $T_{\rm ground}$, measured by the weather station at the site. Both ~~these~~ values are averaged over the same time period as the spectral measurements. The second step is to expand $\mathbf{y}$ in Eq. 12 to include $\mathbf{y^{trop}}$ and retrieve $\mathbf{x^{trop}}$ with the OEM method, using the selected troposphere as the a priori. The effect of tropospheric attenuation on the mesospheric spectra are thus also added to $\mathbf{K}$.

The tropospheric states considered in Eq. 13 are taken from a database constructed ~~on~~ of data from the ERA-Interim project (Dee et al., 2011), covering years 2009, 2010 and 2011. Data were extracted for the OSO site, at 00 and 12 UTH each day of the 3-year long period. In total, the database contains 2190 atmospheric states. Temperature and humidity data were used as provided by ERA-Interim. ~~In a first step, LWCwas set to zero if $r > f$, where f is the ERA-interim cloud fraction and r a random number with flat probability between 0 and 1. If $r \leq f$, LWC was set to LWC_0/f, where LWC_0 is the~~ The liquid water content, LWC, however depends on the cloud cover, and the distribution of clouds within a resolved grid cell in ERA-interim. For the database used in this study, the liquid water content above OSO has been parameterized as a function of cloud fraction and mean liquid water content in an ERA-Interim grid box~~mean LWC. However, in comparison with ASTRID and KONRAD retrievals, this was found to underestimate both the amount of cloudy situations and~~ . The parametrization was corrected such that the fraction of cloudy to non-cloudy days, and the maximum

integrated liquid water ~~(LWP). A better agreement was created artificially by instead selecting r between 0 and 0.5, and increasing LWC_0 with a random factor, uniformly distributed between 1 and 2.~~ path is consistent with measurements from ASTRID and KONRAD. Using this database an apriori troposphere could be selected according to Eq. 13.

Fitting the troposphere using just $T_{\mathrm{sky}}^{\mathrm{mean}}$ and T_{ground} is a grossly under-determined problem, and thus to test the accuracy of this method the tropospheric attenuation was also simultaneously estimated by including measurements from the water vapor radiometer ASTRID into $\mathbf{y}^{\mathbf{trop}}$ (averaged over the same timeperiod as the double sideband receiver). The two channels are simulated as described in Sec. 2.5 using the same settings as described in section 3.1. Simulations were also run for KONRAD, and comparing the simulated brightness temperatures from the two water vapor radiometers and brightness temperature measured, an offset was seen. For clear sky days (i.e. no clouds) ASTRID systematically measured brightness temperatures 3 and 5 K lower than the simulations predicted for the lower and upper frequency channels respectively, while KONRAD had a bias of -2 and +1 K for the two channels. Since both radiometers differ in their bias, we assume that this discrepancy comes from instrumental errors. For ~~this study~~ the study presented in this paper, the ASTRID instrument alone is used to characterize possible errors in the tropospheric correction described by Eq. 13 (see Sec 5). Thus, in order to ensure consistency between the simulations and the measurements, the ASTRID was bias corrected to match the simulated data before it is used.

4 Results of the OSO measurements

Figure 7 shows retrieved profiles from two example cases, one captured during a winter night and one during a autumn day. The winter spectrum shows stronger emission and less noise than the summer spectrum. The different noise levels mainly come from the higher tropospheric humidity in the autumn leading to more attenuation of the mesospheric signal. Figure 8 shows all retrieved CO and O_3 from the measurement period. From the retrieved profiles, it is clear that stronger emission in the winter come from an increase in CO and O_3 at altitudes above 10 Pa. The general structure of the CO distribution is seen in Figure 8 with a sharp increase in volume mixing in the upper mesosphere.

This initial time series mainly ~~cover~~ covers the winter period. During the winter the general circulation brings down air from the thermosphere into the mesosphere which increases the mesospheric CO abundance. This down-welling is strongest inside the polar vortex, and the variation of CO seen from day to day is mainly explained by movement of the polar vortex. OSO is sometimes located within and sometimes outside the vortex during the winter. During summer the general circulation is reversed and ~~hence is characterized by up-welling air which decrease the~~ the abundancy of CO in the mesosphere is reduced as air from the tropics and mid-latidues are transported polewards in the lower mesosphere. This decrease in mesospheric CO ~~abundance, which~~ can be seen ~~in~~ at the end of ~~the measurement series~~our time-series.

The time series of O_3 both show the upper part of the stratospheric peak and a nighttime peak at altitudes above 10 Pa during the winter. Due to the poor resolution of the instrument the observed mesospheric diurnal peak can be a mixture of both "the secondary ozone peak" at ~ 90 km and "the tertiary ozone peak", located at 72km, see Section 1.

Example averaging kernels are shown in Fig. 9. ~~The large negative values for the higher altitude~~ For CO~~averaging kernels~~, the averaging kernels are shown with respect to a change in the atmosphere relative to the apriori profile, while for ozone the averaging kernels are shown with respect vmr changes in the atmosphere. The reason for using different units for the two species is that for CO large changes in ~~vmr at lower altitudes are common in ground based microwave radiometers retrieving (Hoffmann et al., 2011; Forkman et al., 2012; Straub et al., 2013) . However, since the probability of a large change in~~ terms of volume mixing ratio ~~at lower altitudes is small, these negative values are not problematic. The~~ are more probable at high altitude than at lower. This strong vertical gradient of the CO concentration across the altitude range covered by the instrument must be accounted for in the retrieval procedure, and hence $\mathbf{S_a}$ is specified relative to the apriori. This in turn results in averaging kernels optimized with respect to such relative changes, and these averaging kernels are thus most descriptive of how the retrieved atmosphere changes with changes in the real atmosphere. The variability of O_3 around the apriori can be better represented with a constant vmr value, and hence AVKs with respect to this is shown.

The retrievals have a measurement response above 0.8 between ~~100 and 0.2~~ 20 and 0.3 Pa for CO and 200 to ~~0.6~~ 0.8 Pa for O_3. Calculating the degrees of freedom of the retrievals (trace of averaging kernel matrix) CO is retrieved with ~~1.5-2.5~~ 1-2 degrees of freedom (depending on season) and O_3 with ~~3.5-5~~ 3-4.5 degrees of freedom. Resulting to an average vertical resolution of 20 and 10 km for CO and O_3 respectively. For ~~the highest altitudes (e.g. 0.1~~ altitudes above 70 km both lines are dominated by doppler broadening, and thus retrieved values above this level may contain information from changes in the true atmosphere anywhere within this region. This is reflected by the fact that the averaging kernel for 2.4 Pa ~~), the peak of the averaging kernel also deviates from the altitude which the averaging kernel represents~~and 1 Pa remains non-zero at the top of figure 9.

5 Sensitivity to errors in forward model and retrieval parameters

Errors are introduced from uncertainties in the forward model and the retrieval parameters. These include uncertainties in the modeling of the instrument, uncertainties in the spectroscopic parameters used, uncertainties in the tropospheric correction as well as a dependence on the a priori assumptions used in the retrievals. These errors introduce a bias in the mean atmospheric state retrieved, which we will describe as an systematic error. Additionally they add variability to the data which we will describe as a random error source, implying that it affects the scatter of the data set rather than the total mean.

To estimate these errors the retrievals are rerun with each parameter perturbed with its 1-σ uncertainty~~(see Table 5)~~. For the tropospheric correction the error was estimated by comparing the nominal correction method (using only $T_{\rm sky}^{\rm mean}$ and $T_{\rm ground}$) to the extended tropospheric correction including ASTRID. The error estimation was carried out over the sub-set of measurements where simultaneous data from the OSO instrument and ASTRID was available ~~.~~(172 in total). For the spectroscopic parameters the uncertainty was estimated using either the difference between HITRAN 2012 and the value used in our retrieval, or the 1-σ uncertainty reported in HITRAN 2001. The option leading to the greatest difference in the retrieved values was selected as a worst-case scenario. A summary of the values used is given Table 5.

The mean difference (systematic errors) and the standard deviation (random errors) between each of the perturbed retrievals and the standard retrievals are shown in Fig. 10, together with the total root-sum-square error from all the parameters. For CO~~the estimated accuracy is better than 0.3~~, the estimated systematic errors are around 0.2 ppmv for altitudes ~~below 10~~ around 20 Pa, while degrading at altitudes above this, to ~~2~~2.7 ppmv at 1 Pa. The largest source of systematic uncertainty is the characterization of the sideband response, followed by uncertainties in ~~the temperature~~ apriori profile . The total estimated random errors for CO from the retrieval parameters are of the same size as the random error from thermal noise in the measurements (~~< 0.3~~ ~0.2 ppmv ~~below 10~~ at 20 Pa and ~~1~~ ~3 ppmv at 1 Pa). For O_3, the estimated systematic and random ~~uncertainties~~ errors from the simulated error sources, are ~~better~~ less than 0.5 ppmv between ~~100~~ 50 and 1 Pa, with the largest source of systematic errors being ~~the~~ uncertainties in the ~~sideband response and the a priori variability~~pressure broadening coefficient at low altitudes and the sideband response at high altitudes. Errors due to thermal noise in the measurements are better than 0.5 ppmv across all altitudes where the measurement response is greater than 0.8. A summary estimated ~~precision and accuracy~~ random and systematic errors for the retrieved data at ~~three~~ example pressure levels is given in Table 6. For the ~~precision estimate~~ estimate of the random errors, the maximum error from either thermal noise or forward model parameters is used.

6 Satellite comparisons

The vertical profiles from the OSO instruments have been compared to version V-3-3 of CO and O_3 data from the microwave limb sounder MLS on the Aura satellite (Pumphrey et al., 2007) and (Froidevaux et al., 2008), see Table 7. The comparison covers the time period October 2014 until April 2015. MLS data taken closer to the OSO-site than latitude $\pm5^\circ$ and longitude $\pm10^\circ$ has been used, see Figure 11. MLS has measurements solely from either night (UTC 1–2) or day (UTC 11–12) within the used position range. Since the OSO data is 6–h averages the 6–h period with the best overlap with the MLS measurement times has been used in the comparison. The MLS data was interpolated onto the OSO retrieval grid. To compensate for the different vertical resolution of the

two instruments the MLS data was convolved with the averaging kernels, A, of the OSO instrument (Rodgers and Connor, 2003)

$$\mathbf{x}_\mathrm{s} = \mathbf{x}_\mathrm{a} + \mathbf{A}(\mathbf{x}_\mathrm{sat} - \mathbf{x}_\mathrm{a}), \tag{14}$$

where $\mathbf{x}_\mathrm{a}$ is the OSO a priori profile and $\mathbf{x}_\mathrm{s}$ is the smoothed MLS profile.

Figures 12 and 14 show mean profiles of O_3 and CO for the two instruments. Figure 12 shows averaged night and day O_3 profiles from December 2014 and Figure 13 shows the difference in vmr between OSO and MLS. The averaged day profiles from the two instrument are very similar within their measurement ranges. The night profiles however differ at altitudes above 5 Pa ($\sim$ 70 km), where OSO shows a more pronounced peak in the upper mesosphere. The MLS peak seen in the night profile at 2 Pa is probably "The tertiary ozone peak".

There is no clear diurnal variation of the CO profiles. Figure 14 shows averaged day profiles from December 2014 and March 2015 and Figure 15 shows the difference in vmr between OSO and MLS. OSO shows higher CO abundances than MLS at altitudes above 5 Pa during December. During March the difference between the two instruments is much less pronounced.

Figures ~~?? and ??~~ 16 and 17 show time series for the measurement period for OSO and MLS at three different pressure levels (100, ~~10, and~~ 18, and 2.4 Pa) for O_3 and at two different pressure levels (18 and 1 Pa) for CO. The average measurement response for OSO is higher than 80 % for both O_3 and CO at these pressure levels and MLS reports valid ~~data at pressures below ~~mesospheric data at altitudes with pressures $\geq$2 Pa for O_3 and $\geq$1 Pa for CO. Note that due to the vertical resolution of the OSO instrument, the values at these pressure levels are not necessarily completely independent. The CO and O_3 data from the two instruments shows the same general features, both in terms of the overall variation and in sporadic events. The main differences between the two instruments are both the higher OSO values of upper mesospheric O_3 mixing ratios during winter nights and the higher OSO values of upper mesospheric CO mixing ratios during the winter compared to MLS (see also Figures 12 and 14).

MLS data are often used for comparison with ground-based instruments. Boyd et al. (2007) (latitude $< 40°$) and Palm et al. (2010) (high latitudes) found good agreement between ground-based datasets of mesospheric daytime volume mixing ratios of O_3 compared to MLS. The nighttime values of Boyd et al. (2007) were also close to MLS, however Palm et al. (2010) obtained higher O_3 mixing ratios above $\approx$ 70 km during winter nights. The "tertiary ozone peak" above $\approx$ 70 km is only present in winter nights at high latitudes (Marsh et al., 2001) and can hence not be seen in the Boyd et al. (2007) dataset. The altitude of the "tertiary ozone peak" is close to the upper limit of MLS O_3 data which can explain the low bias of MLS winter nighttime O_3 above $\approx$ 70 km compared to the data presented in this report and to the dataset of Palm et al. (2010) .

Similar discrepancies between mesospheric CO measurements from MLS and ground-based instruments, as presented above, have been reported earlier by Forkman et al. (2012) using an older receiver system and by Hoffmann et al. (2011).

7 Summary and conclusions

The first simultaneous measurements of mesospheric O_3 at 110.8 GHz and CO at 115.3 GHz made by a ground-based, double sideband and frequency-switched radiometer system operated at the Onsala Space Observatory, OSO, (57.4° N, 11.9° E) are presented.

Dicke-switching is the generally used observation method in microwave radiometry to diminish effects of gain variations in the receiver system. Frequency-switching is the most time effective Dicke-switching variant since no reference load is observed except in the calibrations. Since the frequency throw has to be less than ~ 20 MHz to avoid gain differences, the method is restricted for studies of the spectral shapes of emission lines from high altitudes where the pressure broadening is limited. The method is hence well-adapted for observations of mesospheric CO and O_3.

Most ground-based microwave heterodyne radiometers for atmospheric remote sensing are operated in single sideband mode. In a double sideband system simultaneous measurements of two emission lines at rather different frequencies, as O_3 at 110.84 GHz and CO at 115.27 GHz, are possible. The drawbacks of a system were both sidebands are used are both that the sideband ratio has to be measured and that the tropospheric attenuation can differ between the two line frequencies.

In this study the gain between the frontend RF input and IF output was estimated by measuring the IF power when a calibrated RF source was connected to the frontend. The RF source was swept across the lower and upper sidebands and the sideband ratio was estimated by comparing the IF and RF powers in the measured frequency range. Standing waves arising from reflections in the transmission line affects the result. In order to reduce the reported error in the sideband ratio estimation, the measurement setup will be refined to try diminish the standing waves.

The commonly used method to compensate measured spectra for the tropospheric attenuation is to use an one-layer model of the troposphere with constant effective temperature and opacity and to correct the observed spectra before the retrieval process. The difference between the opacities in the two sidebands is however too large for this method to work. ~~A new~~ An approach where the troposphere is included in the forward model has been ~~developed~~used.

To calculate vertical profiles of CO and O_3 from the measured spectra the Optimal Estimation Method, OEM, has been used in the retrieval process. To present as exact error estimations as possible, the systematic effects arising from the uncertainties in the different measurement and retrieval parameters, have been carefully studied.

The OSO CO and O_3 data have been compared to measurements from the satellite instrument MLS (v3-3) on Aura. The data from two instruments shows the same general features in both spo-

radic events and in the overall variation. The main differences between the instruments are the higher OSO values of O_3 mixing ratios in the upper mesosphere during the winter nights and the higher OSO winter values of CO mixing ratios in the upper mesosphere compared to MLS.

Microwave radiometry is the only ground-based remote sensing technique that can monitor the mesosphere day and night even during cloudy conditions. Simple and reliable microwave radiometers measuring in the frequency range below 150 GHz can be very valuable for mesospheric research since they can be operated at almost every ground-based site. The described instrument shows the potential of a double-sideband and frequency-switched radiometer system for simultaneous measurements of mesospheric CO and O_3.

Acknowledgements. The Swedish Natural Science Research Council supported the maintenance and development of the OSO receiver system. We thank the teams behind HITRAN and JPL for providing spectroscopic data to the retrievals. We thank the community behind ARTS for software used in the retrieval process and ECMWF for meteorological data and Kaley Walker and Ja-Ho Koo for providing the climatology for CO and O_3 from the Atmospheric Chemistry Experiment (ACE). ACE, also known as SCISAT, is a Canadian-led mission mainly supported by the Canadian Space Agency and the Natural Sciences and Engineering Research Council of Canada. Finally we thank Rüdiger Haas for downloading and preparing of ERA-Interim data and the laboratory and workshop of Onsala Space Observatory for keeping the OSO receiver up and running.

References

Aellig, C., Kaempfer, N., and Hauchecorne, A.: Variability of mesospheric CO in the fall and winter as observed with ground-based microwave radiometry at 115 GHz, J. Geophys. Res., 100, 14 125–14, doi:10.1029/95JD00984, 1995.

Boyd, I. S., Parrish, A. D., Froidevaux, L., Von Clarmann, T., Kyrölä, E., Russell, J. M., and Zawodny, J. M.: Ground-based microwave ozone radiometer measurements compared with Aura-MLS v2. 2 and other instruments at two Network for Detection of Atmospheric Composition Change sites, J. Geophys. Res., 112, doi:10.1029/2007JD008720, 2007.

Brasseur, G. and Solomon, S.: Aeronomy of the Middle Atmosphere, Springer-Verlag, Berlin, 2008.

Buehler, S. A., Eriksson, P., Kuhn, T., von Engeln, A., and Verdes, C.: ARTS, the Atmospheric Radiative Transfer Simulator, J. Quant. Spectrosc. Radiat. Transfer, 91, 65–93, doi:10.1016/j.jqsrt.2004.05.051, 2005.

Caton, W. M., Mannella, G. G., Kalaghan, P. M., Barrington, A. E., and Ewen, H. I.: Radio Measurement of the Atmospheric Ozone Transition at 101.7 GHz, Astrophys. J., 151, L153, doi:10.1086/180163, 1968.

Chapman, S.: A theory of upper-atmospheric ozone, Edward Stanford, 1930.

Christensen, O. M. and Eriksson, P.: Time series inversion of spectra from ground-based radiometers, Atmos. Meas. Tech., 6, 1597–1609, doi:10.5194/amt-6-1597-2013, 2013.

Connor, B. J. and Radford, H.: Pressure broadening of millimeter-wave ozone lines by atmospheric gases, J. Mol. Spectrosc., 117, 15–29, doi:10.1016/0022-2852(86)90088-3, 1986.

Connor, B. J., Siskind, D. E., Tsou, J. J., Parrish, A., and Remsberg, E. E.: Ground-based microwave observations of ozone in the upper stratosphere and mesosphere, J. Geophys. Res., 99, 16 757–16 770, doi:10.1029/94JD01153, 1994.

de Zafra, R. L. and Muscari, G.: CO as an important high-altitude tracer of dynamics in the polar stratosphere and mesosphere, J. Geophys. Res, 109, doi:10.1002/qj.828, 2004.

Dee, D., Uppala, S., Simmons, A., Berrisford, P., Poli, P., Kobayashi, S., Andrae, U., Balmaseda, M., Balsamo, G., Bauer, P., et al.: The ERA-Interim reanalysis: Configuration and performance of the data assimilation system, Q. J. R. Meteorolog. Soc., 137, 553–597, doi:10.1002/qj.828, 2011.

Elgered, G. and Jarlemark, P. O. J.: Ground-based microwave radiometry and long-term observations of atmospheric water vapor, Radio Sci., 33, 707–717, doi:10.1029/98RS00488, 1998.

Emrich, A., Andersson, S., Wannerbratt, M., Sobis, P., Cherednichenko, S., Runesson, D., Ekebrand, T., Krus, M., Tegnader, C., and Krus, U.: Water Vapor Radiometer for ALMA, in: Twentieth International Symposium on Space Terahertz Technology, vol. 1, pp. 174–177, www.nrao.edu/meetings/isstt/papers/2009/2009174177.pdf, 2009.

Eriksson, P. and Merino, F.: On simulating passive observations of the middle atmosphere in the range 1-1000 GHz, Tech. rep., Chalmers University of Technology, Göteborg, Sweden, 1997.

Eriksson, P., Jiménez, C., and Buehler, S. A.: Qpack, a tool for instrument simulation and retrieval work, J. Quant. Spectrosc. Radiat. Transfer, 91, 47–64, doi:10.1016/j.jqsrt.2004.05.050, 2005.

Eriksson, P., Buehler, S. A., Davis, C. P., Emde, C., and Lemke, O.: ARTS, the atmospheric radiative transfer simulator, Version 2, J. Quant. Spectrosc. Radiat. Transfer, 112, 1551–1558, doi:10.1016/j.jqsrt.2011.03.001, 2011.

Fernandez, S., Murk, A., and Kämpfer, N.: GROMOS-C, a novel ground-based microwave radiometer for ozone measurement campaigns, Atmos. Meas. Tech., 8, 2649–2662, doi:10.5194/amt-8-2649-2015, 2015.

Forkman, P., Eriksson, P., Winnberg, A., Garcia, R., and Kinnison, D.: Longest continuous ground-based measurements of mesospheric CO, Geophys. Res. Lett., 30, 1532, doi:10.1029/2003GL016931, 2003.

Forkman, P., Christensen, O. M., Eriksson, P., Urban, J., and Funke, B.: Six years of mesospheric CO estimated from ground-based frequency-switched microwave radiometry at 57° N compared with satellite instruments, Atmos. Meas. Tech., 5, 2827–2841, doi:10.5194/amt-5-2827-2012, 2012.

Froidevaux, L., Jiang, Y. B., Lambert, A., Livesey, N. J., Read, W. G., Waters, J. W., Browell, E. V., Hair, J. W., Avery, M. A., McGee, T. J., Twigg, L. W., Sumnicht, G. K., Jucks, K. W., Margitan, J. J., Sen, B., Stachnik, R. A., Toon, G. C., Bernath, P. F., Boone, C. D., Walker, K. A., Filipiak, M. J., Harwood, R. S., Fuller, R. A., Manney, G. L., Schwartz, M. J., Daffer, W. H., Drouin, B. J., Cofield, R. E., Cuddy, D. T., Jarnot, R. F., Knosp, B. W., Perun, V. S., Snyder, W. V., Stek, P. C., Thurstans, R. P., and Wagner, P. A.: Validation of Aura Microwave Limb Sounder stratospheric ozone measurements, J. Geophys. Res., 113, doi:10.1029/2007JD008771, 2008.

Hartogh, P., Hartmann, G., and Zimmerman, P.: Simultaneous Water Vapour And Ozone Measurements with Millimeterwaves In The Stratosphere And Mesosphere, in: Geoscience and Remote Sensing Symposium, 1991. IGARSS '91. Remote Sensing: Global Monitoring for Earth Management., International, vol. I, pp. 227–230, doi:10.1109/IGARSS.1991.577719, 1991.

Hartogh, P., Jarchow, C., Sonnemann, G. R., and Grygalashvyly, M.: Ozone distribution in the middle latitude mesosphere as derived from microwave measurements at Lindau (51.66°N, 10.13°E), J. Geophys. Res., 116, doi:10.1029/2010JD014393, 2011.

Hays, P. and Roble, R. G.: Observation of mesospheric ozone at low latitudes, Planet. Space Sci., 21, 273–279, doi:10.1016/0032-0633(73)90011-1, 1973.

Hedin, A. E.: Extension of the MSIS thermosphere model into the middle and lower atmosphere, J. Geophys. Res., 96, 1159–1172, doi:10.1029/90JA02125, 1991.

Hocke, K., Kämpfer, N., Ruffieux, D., Froidevaux, L., Parrish, A., Boyd, I., von Clarmann, T., Steck, T., Timofeyev, Y. M., Polyakov, A. V., and Kyrölä, E.: Comparison and synergy of stratospheric ozone measurements by satellite limb sounders and the ground-based microwave radiometer SOMORA, Atmos. Chem. Phys., 7, 4117–4131, doi:10.5194/acp-7-4117-2007, 2007.

Hoffmann, C. G.: Application of CO as a tracer for dynamics in the polar winter middle atmosphere - A study based on ground-based microwave observations in Kiruna, Ph.D. thesis, Universität Bremen, http://elib.suub.uni-bremen.de/edocs/00102610-1.pdf, 2012.

Hoffmann, C. G., Raffalski, U., Palm, M., Funke, B., Golchert, S. H. W., Hochschild, G., and Notholt, J.: Observation of strato-mesospheric CO above Kiruna with ground-based microwave radiometry - retrieval and satellite comparison, Atmos. Meas. Tech., 4, 2389–2408, doi:10.5194/amt-4-2389-2011, 2011.

Janssen, M. A.: Atmospheric Remote Sensing by Microwave Radiometry, John Wiley, New York, 1993.

Jones, A., Walker, K. A., Jin, J. J., Taylor, J. R., Boone, C. D., Bernath, P. F., Brohede, S., Manney, G. L., McLeod, S., Hughes, R., and Daffer, W. H.: Technical Note: A trace gas climatology derived from the Atmospheric Chemistry Experiment Fourier Transform Spectrometer (ACE-FTS) data set, Atmospheric Chemistry and Physics, 12, 5207–5220, doi:10.5194/acp-12-5207-2012, 2012.

Kunzi, K. F. and Carlson, E. R.: Atmospheric CO volume mixing ratio profiles determined from ground-based measurements of the J = 1 $\rightarrow$ O and J = 2 $\rightarrow$ 1 emission lines, J. Geophys. Res., 87, 7235–7241, doi:10.1029/JC087iC09p07235, 1982.

Liebe, H. J., Hufford, G. A., and Cotton, M. G.: Propagation modeling of moist air and suspended water/ice particles at frequencies below 1000 GHz., in: AGARD 52nd Specialists Meeting of the Electromagnetic Wave Propagation Panel, Palma de Mallorca, Spain, 1993.

Lobsiger, E.: Ground-based microwave radiometry to determine stratospheric and mesospheric ozone profiles, J. Atmos. Terr. Phys., 49, 493 – 501, doi:10.1016/0021-9169(87)90043-2, 1987.

Lopez-Puertas, M., Lopez-Valverde, M., Garcia, R., and Roble, R.: A review of CO_2 and CO abundances in the middle atmosphere, Geophysical monograph, 123, 83–100, doi:10.1029/GM123p0083, 2000.

Marsh, D., Smith, A., Brasseur, G., Kaufmann, M., and Grossmann, K.: The existence of a tertiary ozone maximum in the high-latitude middle mesosphere, Geophys. Res. Lett., 28, 4531–4534, doi:10.1029/2001GL013791, 2001.

Moreira, L., Hocke, K., Eckert, E., von Clarmann, T., and Kämpfer, N.: Trend analysis of the 20-year time series of stratospheric ozone profiles observed by the GROMOS microwave radiometer at Bern, Atmos. Chem. Phys., 15, 10 999–11 009, doi:10.5194/acp-15-10999-2015, 2015.

Nagahama, T., Nakane, H., Fujinuma, Y., Ninomiya, M., Ogawa, H., and Fukui, Y.: Ground-based millimeter-wave observations of ozone in the upper stratosphere and mesosphere over Tsukuba, Earth Planets Space, 51, 1287–1296, doi:10.1186/BF03351602, 1999.

Nedoluha, G. E., Boyd, I. S., Parrish, A., Gomez, R. M., Allen, D. R., Froidevaux, L., Connor, B. J., and Querel, R. R.: Unusual stratospheric ozone anomalies observed in 22 years of measurements from Lauder, New Zealand, Atmos. Chem. Phys., 15, 6817–6826, doi:10.5194/acp-15-6817-2015, 2015.

Palm, M., Hoffmann, C. G., Golchert, S. H. W., and Notholt, J.: The ground-based MW radiometer OZORAM on Spitsbergen â€“ description and status of stratospheric and mesospheric O_3-measurements, Atmos. Meas. Tech., 3, 1533–1545, doi:10.5194/amt-3-1533-2010, 2010.

Parrish, A.: Millimeter-wave remote sensing of ozone and trace constituents in the stratosphere, Proceedings of the IEEE, 82, 1915–1929, doi:10.1109/5.338079, 1994.

Parrish, A., deZafra, R. L., Solomon, P. M., and Barrett, J. W.: A ground-based technique for millimeter wave spectroscopic observations of stratospheric trace constituents, Radio Sci., 23, 106–118, doi:10.1029/RS023i002p00106, 1988.

Parrish, A., Connor, B. J., Tsou, J. J., McDermid, I. S., and Chu, W. P.: Ground-based microwave monitoring of stratospheric ozone, J. Geophys. Res, 97, 2541–2546, doi:10.1029/91JD02914, 1992.

Peter, R., Caliseri, Y., and Kämpfer, N.: Variability of middle atmospheric ozone abundances derived from continuous ground-based millimeter wave measurements, in: Proceedings of the XVIII Quadrennial Ozone Symposium, pp. 559–562, 1998.

Pickett, H., Poynter, R., Cohen, E., Delitsky, M., Pearson, J., and Müller, H.: Submillimeter, millimeter, and microwave spectral line catalog, J. Quant. Spectrosc. Radiat. Transfer, 60, 883–890, doi:10.1016/S0022-4073(98)00091-0, 1998.

Piddyachiy, V., Shulga, V., Myshenko, V., Korolev, A., Myshenko, A., Antyufeyev, A., Poladich, A., and Shkodin, V.: 3-mm wave spectroradiometer for studies of atmospheric trace gases, Radiophys. Quantum Electron., 53, 326–333, doi:10.1007/s11141-010-9231-y, 2010.

Pumphrey, H. C., Filipiak, M., Livesey, N., Schwartz, M., Boone, C., Walker, K., Bernath, P., Ricaud, P., Barret, B., Clerbaux, C., Jarnot, R., Manney, G., and Waters, J.: Validation of middle-atmosphere carbon monoxide retrievals from MLS on Aura, J. Geophys. Res., 112, D24S38, doi:10.1029/2007JD008723, 2007.

Rodgers, C.: Inverse methods for atmospheric sounding: Theory and practice, World Scientific, Singapore, 2000.

Rodgers, C. D. and Connor, B.: Intercomparison of remote sounding instruments, J. Geophys. Res, 108, 4116, doi:10.1029/2002JD002299, 2003.

Rosenkranz, P. W.: Absorption of microwaves by atmospheric gases, in: Atmospheric remote sensing by microwave radiometry, edited by Janssen, M. A., pp. 37–90, John Wiley & Sons, Inc., 1993.

Rosenkranz, P. W.: Water Vapor Microwave Continuum Absorption: A Comparison of Measurements and Models, Radio Sci., 33, 919–928, doi:10.1029/98RS01182, (correction in 34, 1025, 1999), 1998.

Rothman, L., Barbe, A., Chris Benner, D., Brown, L., Camy-Peyret, C., Carleer, M., Chance, K., Clerbaux, C., Dana, V., Devi, V., et al.: The HITRAN molecular spectroscopic database: edition of 2000 including updates through 2001, J. Quant. Spectrosc. Radiat. Transfer, 82, 5–44, doi:10.1016/S0022-4073(03)00146-8, 2003.

Rothman, L., Jacquemart, D., Barbe, A., Chris Benner, D., Birk, M., Brown, L., Carleer, M., Chackerian, C., et al.: The HITRAN 2004 molecular spectroscopic database, J. Quant. Spectrosc. Radiat. Transfer, 96, 139–204, doi:10.1016/j.jqsrt.2004.10.008, 2005.

Sheese, P. E., Boone, C. D., and Walker, K. A.: Detecting physically unrealistic outliers in ACE-FTS atmospheric measurements, Atmospheric Measurement Techniques, 8, 741–750, doi:10.5194/amt-8-741-2015, 2015.

Stoew, B., Rieck, C., and Elgered, G.: First results from a new dual-channel water vapor radiometer, in: Proc. of the 14th Working Meeting on European VLBI for Geodesy and Astrometry, P. Tomasi, F. Mantovani and M.-A. Perez-Torres (eds.), pp. 79–82, http://www.evga.org/files/2000EVGA-proc_SanPietro.pdf, 2000.

Straub, C., Espy, P. J., Hibbins, R. E., and Newnham, D. A.: Mesospheric CO above Troll station, Antarctica observed by a ground based microwave radiometer, Earth Syst. Sci. Data, 5, 199–208, doi:10.5194/essd-5-199-2013, 2013.

Studer, S., Hocke, K., Pastel, M., Godin-Beekmann, S., and Kämpfer, N.: Intercomparison of stratospheric ozone profiles for the assessment of the upgraded GROMOS radiometer at Bern, Atmos. Meas. Tech. Discuss., 6, 6097–6146, doi:10.5194/amtd-6-6097-2013, 2013.

Ulich, B. L. and Haas, R. W.: Absolute calibration of millimeter-wavelength spectral lines, Astrophys. J. Suppl. Ser., 30, 247–258, doi:10.1086/190361, 1976.

Vassilev, V., Wadefalk, N., Kozhuharov, R., Abbasi, M., Gunnarsson, S. E., Zirath, H., Pellikka, T., Emrich, A., Pantaleev, M., Kallfass, I., et al.: MMIC-Based Components for MM-Wave Instrumentation, Microwave and Wireless Components Letters, IEEE, 20, 578–580, doi:10.1109/LMWC.2010.2065797, 2010.

Waters, J., Wilson, W., and Shimabukuro, F.: Microwave measurement of mesospheric carbon monoxide, Science, 191, 1174, doi:10.1126/science.191.4232.1174, 1976.

~~urlstyle~~

Aellig, C., Kaempfer, N., and Hauchecorne, A.: Variability of mesospheric COin the fall and winter as observed with ground-based microwave radiometry at 115 GHz, J. Geophys. Res., 100, 14125–14, , 1995.

Brasseur, G. and Solomon, S.: Aeronomy of the Middle Atmosphere, Springer-Verlag, Berlin, 2008.

Buehler, S. A., Eriksson, P., Kuhn, T., von Engeln, A., and Verdes, C.: ARTS, the Atmospheric Radiative Transfer Simulator, J. Quant. Spectrosc. Radiat. Transfer, 91, 65–93, , 2005.

Caton, W. M., Mannella, G. G., Kalaghan, P. M., Barrington, A. E., and Ewen, H. I.: Radio Measurement of the Atmospheric Ozone Transition at 101.7 GHz, Astrophys. J., 151, L153, , 1968.

Chapman, S.: A theory of upper-atmospheric ozone, Edward Stanford, 1930.

Christensen, O. M. and Eriksson, P.: Time series inversion of spectra from ground-based radiometers, Atmos. Meas. Tech., 6, 1597–1609, , 2013.

Dee, D., Uppala, S., Simmons, A., Berrisford, P., Poli, P., Kobayashi, S., Andrae, U., Balmaseda, M., Balsamo, G., Bauer, P., et al.: The ERA-Interim reanalysis: Configuration and performance of the data assimilation system, Q. J. R. Meteorolog. Soc., 137, 553–597, , 2011.

Elgered, G. and Jarlemark, P. O. J.: Ground-based microwave radiometry and long-term observations of atmospheric water vapor, Radio Sci., 33, 707–717, , 1998.

Emrich, A., Andersson, S., Wannerbratt, M., Sobis, P., Cherednichenko, S., Runesson, D., Ekebrand, T., Krus, M., Tegnader, C., and Krus, U.: Water Vapor Radiometer for ALMA, in: Twentieth International Symposium on Space Terahertz Technology, vol. 1, pp. 174–177, 2009.

Eriksson, P., Jimnez, C., and Buehler, S. A.: Qpack, a tool for instrument simulation and retrieval work, J. Quant. Spectrosc. Radiat. Transfer, 91, 47–64, , 2005.

Eriksson, P., Buehler, S. A., Davis, C. P., Emde, C., and Lemke, O.: ARTS, the atmospheric radiative transfer simulator, Version 2, J. Quant. Spectrosc. Radiat. Transfer, 112, 1551–1558, , 2011.

Fernandez, S., Murk, A., and Kämpfer, N.: GROMOS-C, a novel ground based microwave radiometer for ozone measurement campaigns, Atmos. Meas. Tech. Discuss., 8, 3001–3048, , 2015.

Forkman, P., Eriksson, P., Winnberg, A., Garcia, R., and Kinnison, D.: Longest continuous ground-based measurements of mesospheric CO, Geophys. Res. Lett., 30, 1532, , 2003.

Forkman, P., Christensen, O. M., Eriksson, P., Urban, J., and Funke, B.: Six years of mesospheric CO estimated from ground-based frequency-switched microwave radiometry at 57° N compared with satellite instruments, Atmos. Meas. Tech., 5, 2827–2841, , 2012.

Froidevaux, L., Jiang, Y. B., Lambert, A., Livesey, N. J., Read, W. G., Waters, J. W., Browell, E. V., Hair, J. W., Avery, M. A., McGee, T. J., Twigg, L. W., Sumnicht, G. K., Jucks, K. W., Margitan, J. J., Sen, B., Stachnik, R. A., Toon, G. C., Bernath, P. F., Boone, C. D., Walker, K. A., Filipiak, M. J., Harwood, R. S., Fuller, R. A., Manney, G. L., Schwartz, M. J., Daffer, W. H., Drouin, B. J.,

Cofield, R. E., Cuddy, D. T., Jarnot, R. F., Knosp, B. W., Perun, V. S., Snyder, W. V., Stek, P. C., Thurstans, R. P., and Wagner, P. A.: Validation of Aura Microwave Limb Sounder stratospheric ozone measurements, J. Geophys. Res., 113, , 2008.

Hartogh, P., Hartmann, G., and Zimmerman, P.: Simultaneous Water Vapour And Ozone Measurements with Millimeterwaves In The Stratosphere And Mesosphere, in: Geoscience and Remote Sensing Symposium, 1991. IGARSS '91. Remote Sensing: Global Monitoring for Earth Management., International, vol. I, pp. 227–230, , 1991.

Hartogh, P., Jarchow, C., Sonnemann, G. R., and Grygalashvyly, M.: Ozone distribution in the middle latitude mesosphere as derived from microwave measurements at Lindau (51.66°N, 10.13°E), J. Geophys. Res., 116, , 2011.

Hays, P. and Roble, R. G.: Observation of mesospheric ozone at low latitudes, Planet. Space Sci., 21, 273–279, , 1973.

Hedin, A. E.: Extension of the MSISthermosphere model into the middle and lower atmosphere, J. Geophys. Res., 96, 1159–1172, , 1991.

Hoffmann, C. G., Raffalski, U., Palm, M., Funke, B., Golchert, S. H. W., Hochschild, G., and Notholt, J.: Observation of strato-mesospheric CO above Kiruna with ground-based microwave radiometry - retrieval and satellite comparison, Atmos. Meas. Tech., 4, 2389–2408, , 2011.

Janssen, M. A.: Atmospheric Remote Sensing by Microwave Radiometry, John Wiley, New York, 1993.

Jones, A., Walker, K. A., Jin, J. J., Taylor, J. R., Boone, C. D., Bernath, P. F., Brohede, S., Manney, G. L., McLeod, S., Hughes, R., and Daffer, W. H.: Technical Note: A trace gas climatology derived from the Atmospheric Chemistry Experiment Fourier Transform Spectrometer (ACE-FTS) data set, Atmospheric Chemistry and Physics, 12, 5207–5220, , 2012.

Liebe, H. J., Hufford, G. A., and Cotton, M. G.: Propagation modeling of moist air and suspended water/ice particles at frequencies below 1000 GHz., in: AGARD 52nd Specialists Meeting of the Electromagnetic Wave Propagation Panel, Palma de Mallorca, Spain, 1993.

Lobsiger, E.: Ground-based microwave radiometry to determine stratospheric and mesospheric ozone profiles, J. Atmos. Terr. Phys., 49, 493 – 501, , 1987.

Lopez-Puertas, M., Lopez-Valverde, M., Garcia, R., and Roble, R.: A review of CO_2 and COabundances in the middle atmosphere, Geophysical monograph, 123, 83–100, , 2000.

Marsh, D., Smith, A., Brasseur, G., Kaufmann, M., and Grossmann, K.: The existence of a tertiary ozone maximum in the high-latitude middle mesosphere, Geophys. Res. Lett., 28, 4531–4534, , 2001.

Nagahama, T., Nakane, H., Fujinuma, Y., Ninomiya, M., Ogawa, H., and Fukui, Y.: Ground-based millimeter-wave observations of ozone in the upper stratosphere and mesosphere over Tsukuba, Earth Planets Space, 51, 1287–1296, , 1999.

Nedoluha, G. E., Boyd, I. S., Parrish, A., Gomez, R. M., Allen, D. R., Froidevaux, L., Connor, B. J., and Querel, R. R.: Unusual stratospheric ozone anomalies observed in 22 years of measurements from Lauder, New Zealand, Atmos. Chem. Phys. Discuss., 15, 5241–5267, , 2015.

Parrish, A.: Millimeter-wave remote sensing of ozone and trace constituents in the stratosphere, Proceedings of the IEEE, 82, 1915–1929, , 1994.

Parrish, A., deZafra, R. L., Solomon, P. M., and Barrett, J. W.: A ground-based technique for millimeter wave spectroscopic observations of stratospheric trace constituents, Radio Sci., 23, 106–118, , 1988.

Parrish, A., Connor, B. J., Tsou, J. J., McDermid, I. S., and Chu, W. P.: Ground-based microwave monitoring of stratospheric ozone, J. Geophys. Res, 97, 2541–2546, , 1992.

Peter, R., Caliseri, Y., and Kämpfer, N.: Variability of middle atmospheric ozone abundances derived from continuous ground-based millimeter wave measurements, in: Proceedings of the XVIII Quadrennial Ozone Symposium, pp. 559–562, 1998.

Pickett, H., Poynter, R., Cohen, E., Delitsky, M., Pearson, J., and Mller, H.: Submillimeter, millimeter, and microwave spectral line catalog, J. Quant. Spectrosc. Radiat. Transfer, 60, 883–890, , 1998.

Piddyachiy, V., Shulga, V., Myshenko, V., Korolev, A., Myshenko, A., Antyufeyev, A., Poladich, A., and Shkodin, V.: 3-mm wave spectroradiometer for studies of atmospheric trace gases, Radiophys. Quantum Electron., 53, 326–333, , 2010.

Pumphrey, H. C., Filipiak, M., Livesey, N., Schwartz, M., Boone, C., Walker, K., Bernath, P., Ricaud, P., Barret, B., Clerbaux, C., Jarnot, R., Manney, G., and Waters, J.: Validation of middle-atmosphere carbon monoxide retrievals from MLSon Aura, J. Geophys. Res., 112, D24S38, , 2007.

Rodgers, C.: Inverse methods for atmospheric sounding: Theory and practice, World Scientific, Singapore, 2000.

Rodgers, C. D. and Connor, B.: Intercomparison of remote sounding instruments, J. Geophys. Res, 108, 4116, , 2003.

Rosenkranz, P. W.: Absorption of microwaves by atmospheric gases, in: Atmospheric remote sensing by microwave radiometry, edited by Janssen, M. A., pp. 37–90, John Wiley Sons, Inc., 1993.

Rosenkranz, P. W.: Water Vapor Microwave Continuum Absorption: A Comparison of Measurements and Models, Radio Sci., 33, 919–928, , (correction in 34, 1025, 1999), 1998.

Rothman, L., Jacquemart, D., Barbe, A., Chris Benner, D., Birk, M., Brown, L., Carleer, M., Chackerian, C., et al.: The HITRAN 2004 molecular spectroscopic database, J. Quant. Spectrosc. Radiat. Transfer, 96, 139–204, , 2005.

Sheese, P. E., Boone, C. D., and Walker, K. A.: Detecting physically unrealistic outliers in ACE-FTS atmospheric measurements, Atmospheric Measurement Techniques, 8, 741–750, , 2015.

Straub, C., Espy, P. J., Hibbins, R. E., and Newnham, D. A.: Mesospheric CO above Troll station, Antarctica observed by a ground based microwave radiometer, Earth Syst. Sci. Data, 5, 199–208, , 2013.

Studer, S., Hocke, K., Pastel, M., Godin-Beekmann, S., and Kämpfer, N.: Intercomparison of stratospheric ozone profiles for the assessment of the upgraded GROMOS radiometer at Bern, Atmos. Meas. Tech. Discuss., 6, 6097–6146, , 2013.

Ulich, B. L. and Haas, R. W.: Absolute calibration of millimeter-wavelength spectral lines, Astrophys. J. Suppl. Ser., 30, 247–258, , 1976.

Vassilev, V., Wadefalk, N., Kozhuharov, R., Abbasi, M., Gunnarsson, S. E., Zirath, H., Pellikka, T., Emrich, A., Pantaleev, M., Kallfass, I., et al.: MMIC-Based Components for MM-Wave Instrumentation, Microwave and Wireless Components Letters, IEEE, 20, 578–580, , 2010.

Waters, J., Wilson, W., and Shimabukuro, F.: Microwave measurement of mesospheric carbon monoxide, Science, 191, 1174, , 1976.

Table 1: Receiver specifications

Radio frequency	110–116 GHz, DSB
Mirror edge taper	-35 dB
Elevation	80°, fixed
Horn	Aluminium, corrugated
Beam width, FWHM	6°
First stage	LNA +20 dB, Ambient temperature
Image sideband rejection	None, DSB
Sideband response	0.50 / 0.50 $\pm$ 0.05
Local oscillator (LO)	Synth. + multipliers
LO frequency	113 GHz
Frequency throw ($2\Delta f$)	8 MHz
Mixer IF	2.21 GHz
DSB receiver temperature	$\sim$450 K
Backend spectrometer	800 channel autocorrelator
Bandwidth	20 MHz
Nominal resolution	25 kHz
Integration time	6 h centered at UTC 05, 11, 17, and 23

Table 2: Specifications for the total power dual channel radiometers

Radiometer	ASTRID	KONRAD	Unit
Radio frequencies	21.0 / 31.4	20.6 / 31.6	[GHz]
Antenna (one for each frequency)	Dielectrically loaded horn	Conical lens horns	
Beam width, FWHM	6 / 6	2.9 / 2.0	[°]
Pointing resolution	0.1	0.1	[°]
Reference load temperatures	313 / 360	313 / 373	[K]
System noise temperature	450 / 550	450 / 550	[K]
RF bandwidth (both channels)	1000	320	[MHz]
Accuracy	< 1	0.5	[K]

Table 3: Summary of the complete absorption models. The model name refers to the name used internally in ARTS, while the model is described in the reference given.

Species	Absorption model	Reference
N_2	N2-SelfContStandardType	Rosenkranz (1993)
O_2	O2-PWR98	Rosenkranz (1998)
H_2O	H2O-PWR98	Rosenkranz (1998)
LiquidWater	liquidcloud-MPM93	Liebe et al. (1993)

Table 4: Summary of the two major spectroscopic lines.

Line parameter	CO	O_3	Unit
Center frequency, f_0	115.2712018	110.8359230	$[\mathrm{GHz}]$
Line intensity, I_0	$9.761128 \cdot 10^{-18}$	$3.567796 \cdot 10^{-17}$	$[\mathrm{m^2\,Hz^{-1}}]$
Ref. temp. for Line intensity	300	300	$[\mathrm{K}]$
Air broadened width	23332.68	23932.87	$[\mathrm{Hz\,Pa^{-1}}]$
Self broadened width	25958.54	30009.87	$[\mathrm{Hz\,Pa^{-1}}]$
Ref. temp. for broad. param.	296	296	$[\mathrm{K}]$
Temp. dep. exp. for broad. param.	0.69	0.73	$[-]$

~~Summary of the complete absorption models. The model name refers to the name used internally in ARTS, while the model is described in the reference given. Species Absorption model ReferenceN2-SelfContStandardType Rosenkranz (1993) O2-PWR98 Rosenkranz (1998) H2O-PWR98 Rosenkranz (1998) liquidcloud-MPM93 Liebe et al. (1993)~~

Table 5: Summary of the perturbations applied to the forward model and retrieval parameters in the sensitivity study. Method indicates how the perturbation values were estimated.

Parameter	Perturbation (1σ)	Method
Line strength (O_3 / CO)	~2%	~~Pickett et al. (19~~
Pressure broadening parameter (O_3 / CO)	10%	~~Rothman et al. (2~~
A priori profile	50%	-
A priori uncertainty	50%	-
Temperature profile	± 5 K	1σ of MSISE-90
Sideband response	5%	Sec. 2.4
Tropospheric correction	~~comparison to method using ASTRID~~ Comparison to method using ASTRID	-

Table 6: Summary of error ~~estimate~~estimates.

Species	~~Error (~~Pressure (Pa)	Systematic error (ppmv)	Random error (ppmv)
O_3	100	~~10~~1.01	~~1~~0.39
O_3	~~Precision~~ 18	~~0.31~~ 0.22	0.44 ~~0.49~~
O_3	~~Accuracy~~ 2.4	~~0.68~~ 0.27	~~0.15 0.28~~ 0.34
CO	~~Precision~~ 18	~~0.19~~ 0.18	~~0.29 1.30~~ 0.19
CO	~~Accuracy~~ 1	~~0.07~~ 2.76	~~0.24 1.78~~ 1.66

Table 7: Satellite characteristics.

Satellite instrument	Aura-MLS
Launch	15 July 2004
Orbit inclination	90°
Measurement principle	Limb sounding, emission
Frequency band	240 GHz
CO and O_3 versions	V-3-3
CO validation	Pumphrey et al. (2007)
O_3 validation	Froidevaux et al. (2008)
Vertical range	~~16–80~~10–75 (85) km for O_3 (CO)
Vertical resolution (mesosphere)	7–8 km
Horizontal resolution (mesosphere)	200 km
Systematic errors (above 60 km)	$\sim \pm 20$ %
Co-location range satellite-OSO	Lat. $\pm 5°$ & Long. $\pm 10°$
Co-located measurement days	140

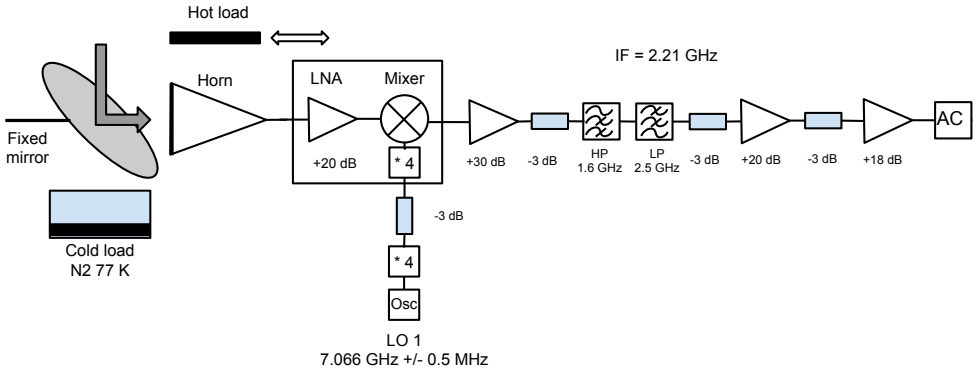

Figure 1: Block diagram of the DSB 110-115 GHz O_3/ CO receiver system. The cold load is regularly mounted and used.

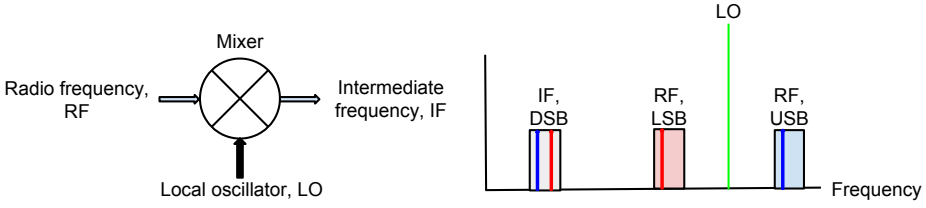

Figure 2: Mixer fundamentals.

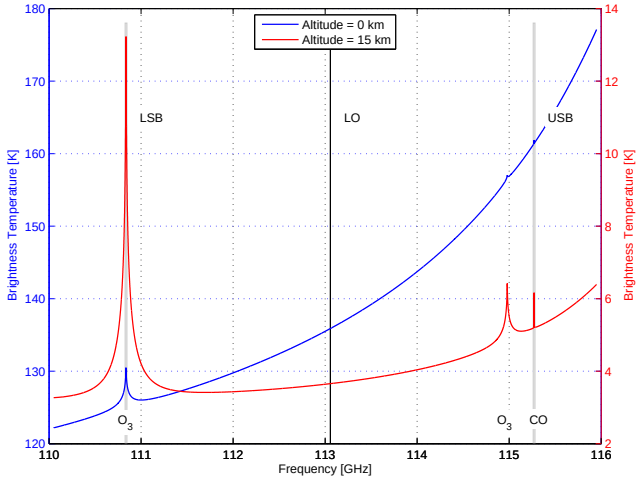

Figure 3: Simulated atmospheric spectra as seen with an elevation of 80° from the ground (blue) and, for clarity, from an altitude of 15 km (red). The 20 MHz wide LSB and USB frequency ranges and the LO frequency are marked.

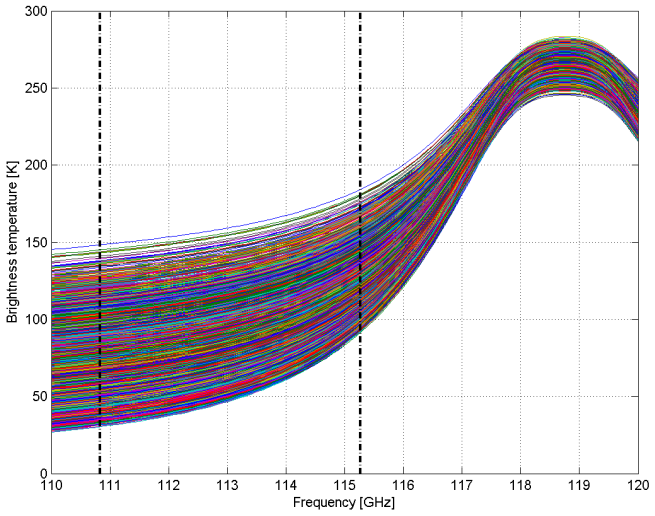

Figure 4: Simulated atmospheric spectra from one year of radiosonde data taken at the Landvetter airport 38 km NE of the Onsala site. Different tropospheric conditions explain the seen variation.

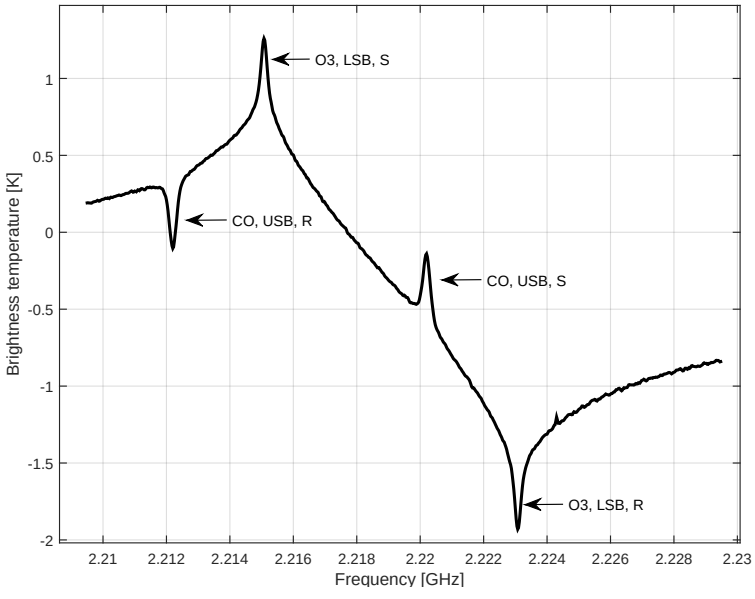

Figure 5: Average frequency-switched spectrum from December 2014 of $\mathrm{O_3}$ from the lower sideband, LSB, and CO from the upper sideband, USB. S and R are the frequency-switching signal and reference phases. The wide wings of the $\mathrm{O_3}$-line explain the general baseline shape.

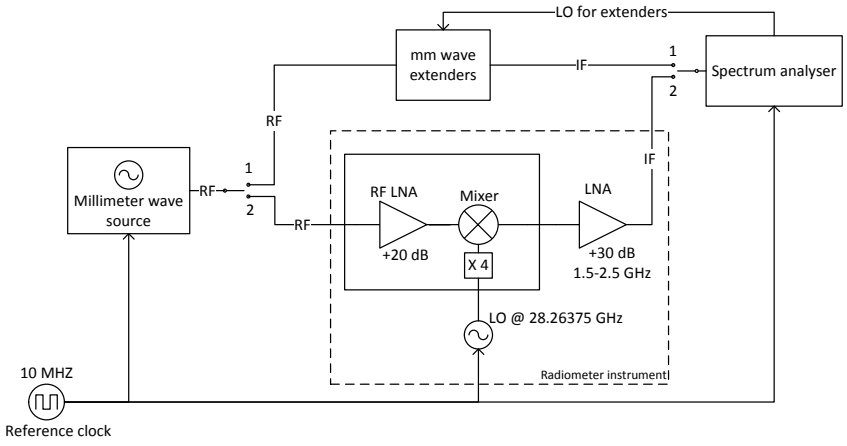

Figure 6: Setup for sideband ratio measurement.

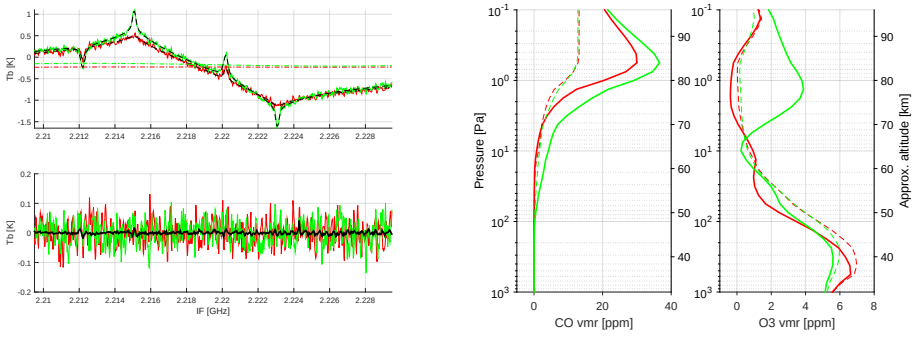

Figure 7: The top left panel shows measured spectra (solid lines) and fitted spectra (black-dashed lines) at two different times. The green line corresponds to a mid-winter night, while the red is an autumn day. The near horizontal dashed-dotted lines are the fitted baselines for the two spectra. The lower left panel shows the residuals from the fitting of the two spectra together with the mean residual of all spectra (black line). The two right panels show the retrieved profiles for the corresponding cases, together with the a priori profile used (dashed).

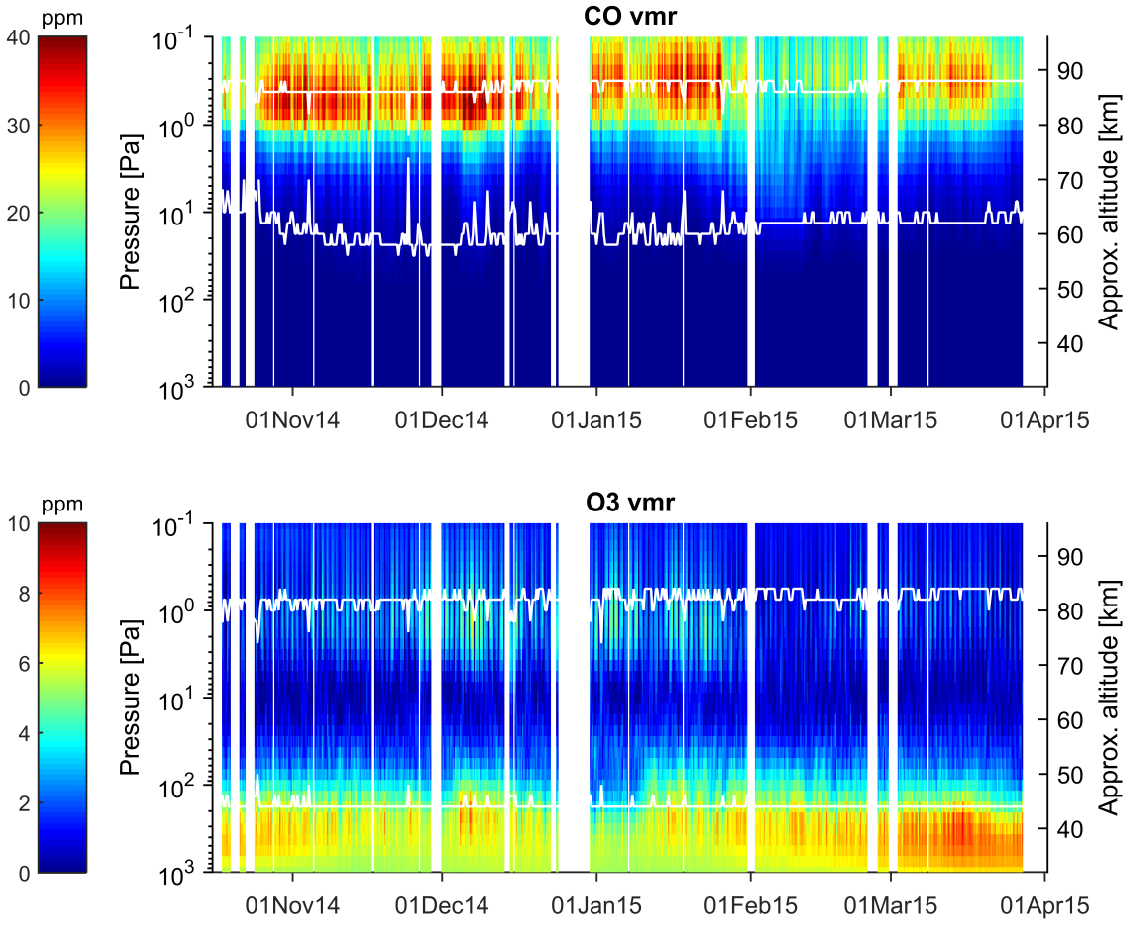

Figure 8: Retrieved vmr of CO and O3 (ppm) for the measurement period. The white lines mark where the a priori affects the result with 20 % (< 20 % between the lines).

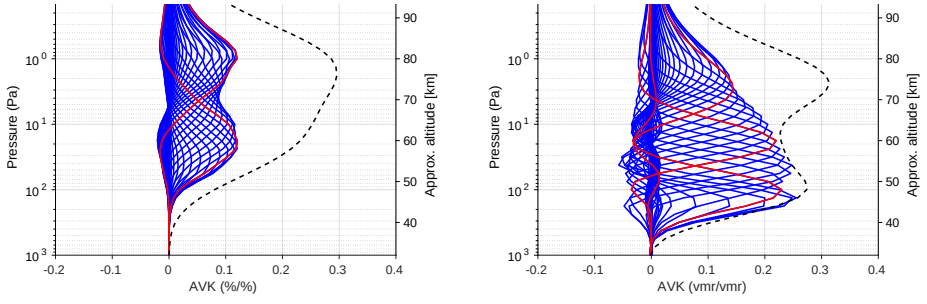

Figure 9: Averaging kernels ~~(vmr/vmr)~~ for CO and O_3 for November ~~15~~ 16 2014. The kernels ~~for~~ at 100, ~~10~~18, ~~1~~ 2.4 Pa for O_3 and ~~0.1~~18, 1 Pa for CO are highlighted with red lines. The dashed line is the measurement response divided by 4.

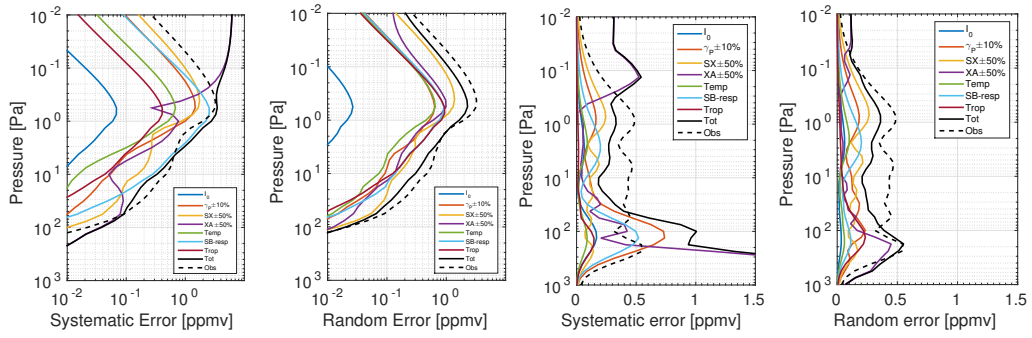

Figure 10: ~~Accuracy~~ Estimated systematic and ~~precision~~ random errors for ~~CO~~ CO (two leftmost panels) and ~~O3~~ O_3 (two rightmost panels) estimated by perturbation of forward model and retrieval parameters. The parameters perturbed are line strength, I_0, pressure broadening parameter, γ_p, a priori variance, SX, a priori profile, XA, a priori temperature profile, $Temp$, the sideband response $SB-resp$ and the tropospheric correction $Trop$. The total RMS error expected is given by the solid black line, and the observation error by the dashed black line.

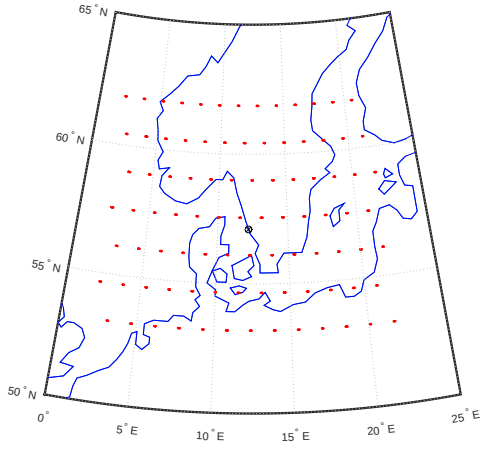

Figure 11: Collocations MLS–OSO.

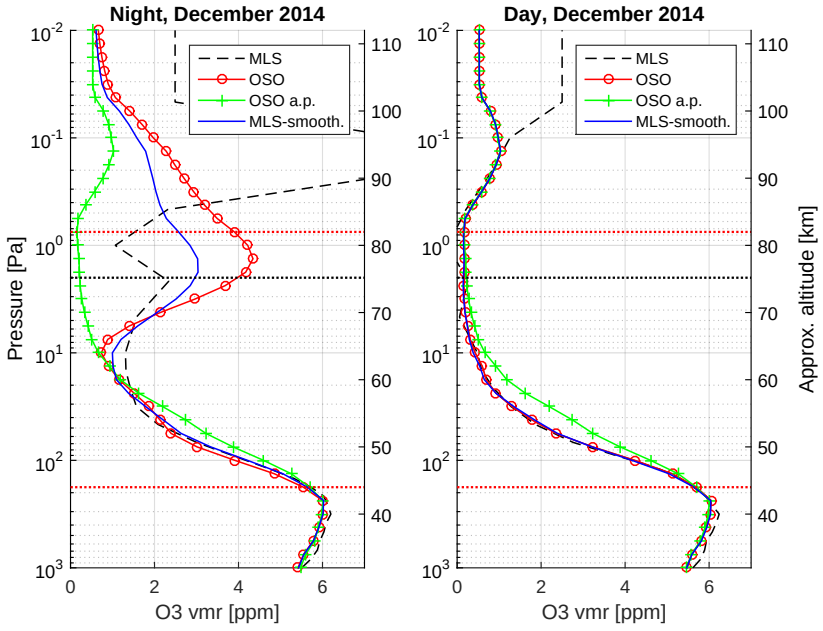

Figure 12: Average night and day vertical profiles of O_3 from December 2014. The a priori affects the OSO result < 20 % between the red dotted horizontal lines. The black dotted horizontal line mark the upper altitude for the MLS data.

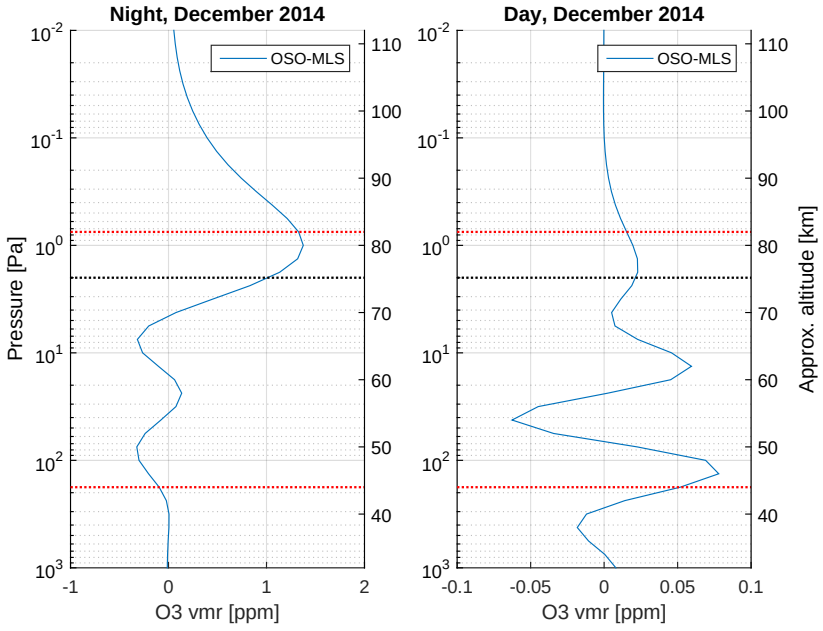

Figure 13: Difference between OSO and MLS (OSO-MLS) for night and day vertical profiles of O_3 from December 2014. The a priori affects the OSO result < 20 % between the red dotted horizontal lines. The black dotted horizontal line mark the upper altitude for the MLS data.

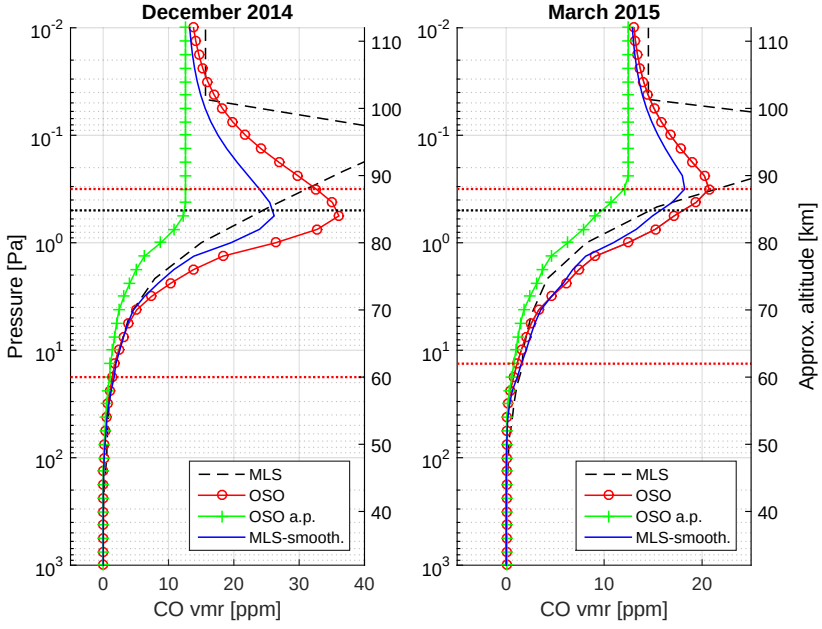

Figure 14: Average December and March vertical profiles of CO. The a priori affects the OSO result < 20 % between the red dotted horizontal lines. The black dotted horizontal line mark the upper altitude for the MLS data.

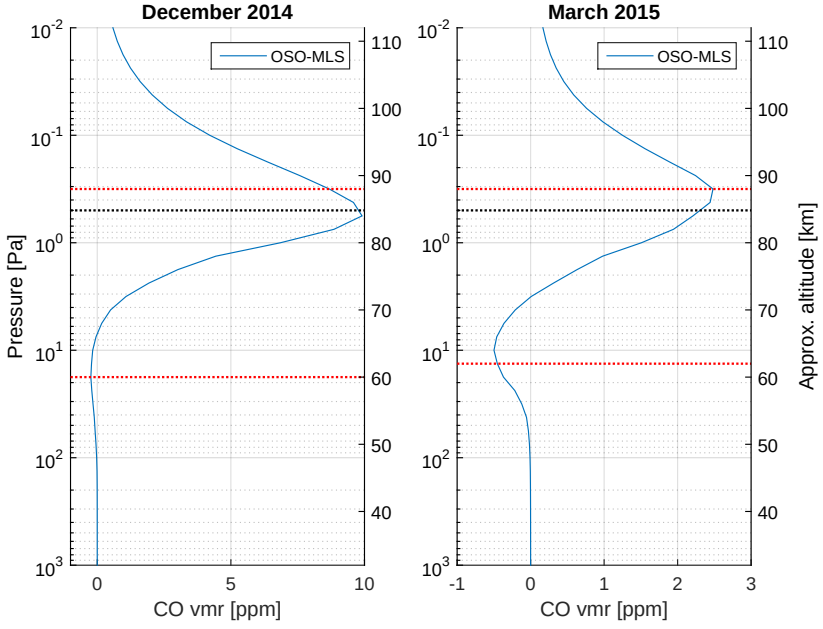

Figure 15: Difference between OSO and MLS (OSO-MLS) for December and March vertical profiles of CO. The a priori affects the OSO result < 20 % between the red dotted horizontal lines. The black dotted horizontal line mark the upper altitude for the MLS data.

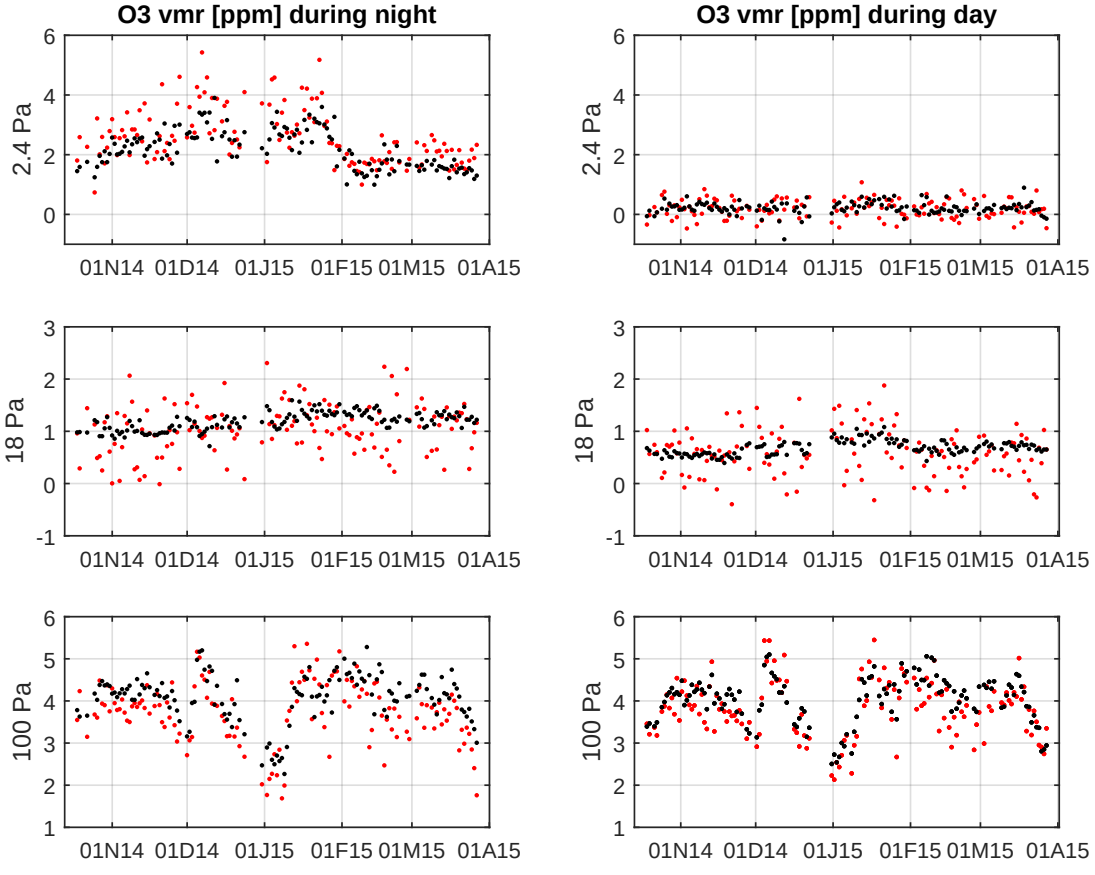

Figure 16: O_3 at 3 different altitudes, October–April (ddmyy), OSO (red), MLS (black).

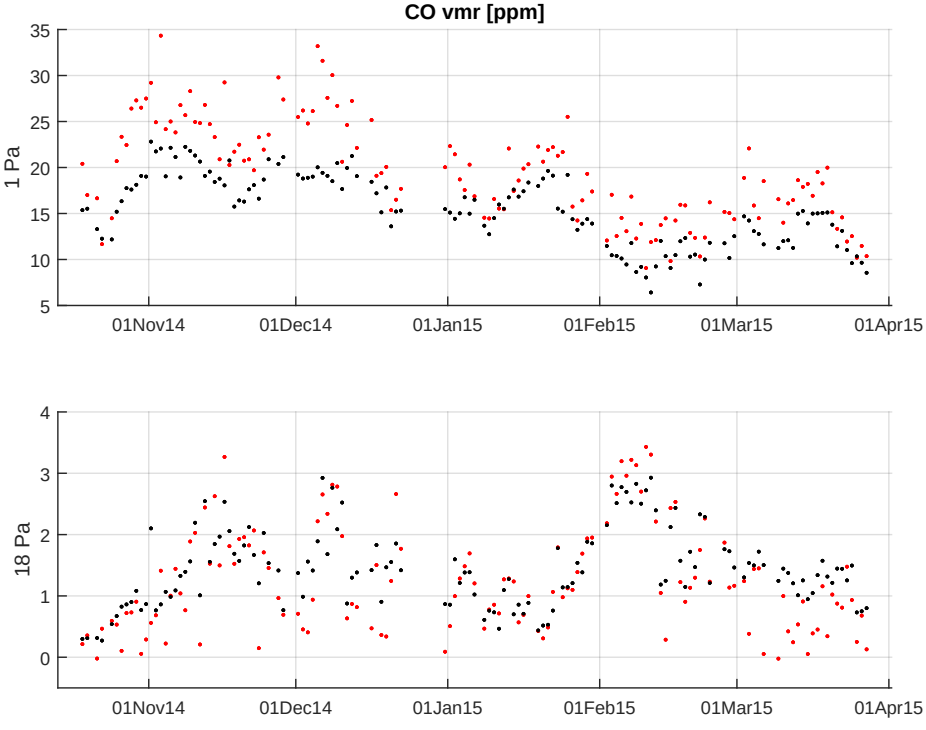

Figure 17: CO at ~~3~~ 2 different altitudes, October–April (ddmmmyy), OSO (red), MLS (black).